Springer Proceedings in Physics 244

Alexander D. Pogrebnjak
Maksym Pogorielov
Roman Viter *Editors*

Nanomaterials in Biomedical Application and Biosensors (NAP-2019)

Springer

Preface

This book covers novel and innovative technologies used for development, modeling, chemical and physical investigation and biomedical (in-vitro and in-vivo) trials of nanomaterials and nanocomposites for medical applications and sensors. Novel method for nanoparticle development and manufacturing highlighted as well as their safety and promising application are under consideration. This book opens a new frontier in metal, metal oxide nanoparticle, hierarchical nanostructures and organic coatings as a sensor for gases, inorganic and organic materials, including biosensors for bacteria and cancer detection. Organic nanoparticle composites for medical application (tissue engineering, tissue replacement, regeneration, etc.) including hydroxyapatite-NPs are under the special focus, including in-vitro and preclinical investigation. Nanoparticle and nanocomposites for antibacterial application are discussed in the present book with a detailed focus on NPs–bacteria interaction and cell toxicity study. Orthopedic and dental implant coatings discussed and detailed described their biological effect and safety.

Sumy, Ukraine — Alexander D. Pogrebnjak
Sumy, Ukraine — Maksym Pogorielov
Riga, Latvia — Roman Viter

Chapter 11
Composite Ultrafiltration Membrane Incorporated with Dispersed Oxide Nanoparticles

L. M. Rozhdestvenska, O. I. V'yunov, L. N. Ponomarova, A. V. Bilduykevich, T. V. Plisko, Y. G. Zmievskii and V. D. Ivchenko

Abstract Organic-inorganic membranes containing the nanoparticles of hydrated zirconium dioxide and $BaFe_{12}O_{19}$ magnetic nanoparticles were obtained. The nanoparticles were inserted into polymer matrices, they form aggregates, a size of which is up to 20 nm (active layer) and up to 2 μm (macroporous fibrous support). Larger aggregates are formed in absence of the magnetic constituent (up to 5 μm). The membranes were tested for filtration of sugar beet juice. Due to smaller particle size, the membrane containing also $BaFe_{12}O_{19}$ shows the liquid flux of 4.3×10^{-7} to 5.7×10^{-7} m^3 m^{-2} s^{-1} at 2 bar and rejection towards vegetable protein of 55–87%. Regarding the membranes including no magnetic nanoparticles, these values are 3.8×10^{-7} to 5.5×10^{-7} m^3 m^{-2} s^{-1} and 38–77%.

11.1 Introduction

Ultrafiltration technology is widely used for removal of colloidal particles from ground and brackish water, wastewater, sea water [1]. This stage of water treatment is before reverse osmosis to prevent membrane fouling. Ultrafiltration is also applied

L. M. Rozhdestvenska · O. I. V'yunov
Vernadsky Institute of General and Inorganic Chemistry, Ukrainian National Academy of Sciences, Kiev, Ukraine

L. N. Ponomarova (✉)
Sumy State University, Sumy, Ukraine
e-mail: l.ponomarova@chem.sumdu.edu.ua

A. V. Bilduykevich · T. V. Plisko
Institute of Physical Organic Chemistry, National Academy of Science of Belarus, Minsk, Belarus

Y. G. Zmievskii
Ministry of Education and Science of Ukraine, National University of Food Technologies, Kiev, Ukraine

V. D. Ivchenko
Sumy National Agrarian University, Sumy, Ukraine

A. D. Pogrebnjak et al. (eds.), *Nanomaterials in Biomedical Application and Biosensors (NAP-2019)*, Springer Proceedings in Physics 244,
https://doi.org/10.1007/978-981-15-3996-1_11

to beverage industry, for instance, for milk skimming and effluents treatment etc. The main problem of filtration is a decrease of membrane permeability due to fouling with organics. This is especially important, when liquids of biological origin are processed.

In general, species of organic substances, microorganisms, iron oxide and silicon dioxide significantly decrease the time of filtration. The membranes need chemical regeneration that involves aggressive reagents. Frequent regeneration reduces a lifetime of the membranes. One of the ways to overcome these disadvantages is to enhance hydrophilicity of polymer membranes. As a rule, nanoparticles of inorganic ion-exchangers are used for modification of polymers. A number of inorganic compounds are applied to modifying [20]: zirconium hydrophosphate [15] (the attempt to use these materials as a filler for electromembrane processes is known [4], moreover, they are used for modifying of ion exchange resins [6]), silica [18], hydrated zirconium [15, 16] or iron oxide [17]. This approach allows one to enhance liquid permeability and anti-fouling ability without sufficient changes of membrane structure.

Magnetic particles are another type of modifier that improves functional properties of polymer membranes. The membrane containing magnetic Fe_3O_4 nanoparticles and graphene oxide particles shows high flow of pure water and high degree of rejection (up to 83.0%) [11]. Membranes containing iron nanoparticles can be used to remove copper and lead ions from wastewater [9, 11]. Adsorption capacity increases due to improved hydrophilicity on the one hand and nucleophilic functional groups on the surface of nanoparticles on the other hand. Nanocomposite membrane exhibits minimal interaction with whey protein due to its higher hydrophilicity, which leads to a polar-non-polar interaction between membrane surface and protein. This depresses membrane fouling [19].

The membranes modified with magnetic nanoparticles shows an increase in water flow due to changes in the average pore radius, porosity and hydrophilicity of the membranes. The membrane surface roughness and hydrophilicity are considered to be main factors, which minimize membrane fouling.

The aim of the work was to obtain organic-inorganic membranes containing inorganic modifier, particularly magnetic one, and to establish the effect of the filler on separation ability of the composite membranes and their stability against fouling.

11.2 Experiment Details

11.2.1 Membrane Modifying

Ultrafiltration membranes (produced by the Institute of Physico-Organic Chemistry of the National Academy of Science of the Republic of Belarus) were used for investigations as a polymer substrate. These materials consist of macroporous substrate

(non-woven polyester) and ultrathin active layer (polysulfone (PS) or polyacrylonitrile (PAN)). Further the membranes were marked according to the polymer forming the active layer. PS and PAN rejects globular proteins, molecular mass of which is 100 and 50 kDa, respectively.

Magnetic nanoparticles (MNP) $BaFe_{12}O_{19}$ were synthesized according to [2]. In order to provide their fixation in membrane pores, hydrated zirconium dioxide (HZD) was used. First of all, sol of insoluble zirconium hydroxocomplexes was obtained from a 0.25 M $ZrOCl_2$ solution similarly to [8]. MNP were dispersed in zirconium sol and treated with ultrasound at 30 kHz. The membranes were degassed in deionized water under vacuum conditions at 343 K, and impregnated with suspension of MNP in sol. Then HZD and MNP were coprecipitated directly in the polymer with a 0.1 M NH_4OH solution. The membrane was dried at 50 °C and cleaned with ultrasound to remove the precipitate from its outer surface. This approach, which involves impregnation of a membrane with the suspension of insoluble compounds followed by precipitation, was applied earlier to modification of ceramics [7]. For comparison, the membranes containing only HZD were obtained. In this case, the polymer matrix was impregnated with zirconium-containing sol.

Morphology of the membranes was investigated using scanning electron microscopy (SEM). Fractal dimension of aggregates in macroporous support was determined with methods of cube counting, triangulation, and power spectrum analysis similarly to [3].

Before the application of transmission electron microscopy (TEM), the active layer was separated from the macroporous substrate, and milled in the medium of liquid nitrogen.

11.2.2 Membrane Testing

The experimental set-up for filtration consisted of typical elements for baromembrane separation (magnetic pump, manometer, rotameter). A divided two-compartment flow-type cell was used. An effective area of the membrane was 2.82×10^{-3} m^2. Before the measurements, the membrane was pressed by means of pumping deionization water at 4 bar. The effluent volume was measured after predetermined time. Filtration was stopped, when the constant flow rate through the membrane was achieved.

Tap water containing 1 and 0.2 mol dm^{-3} Ca^{2+} and Mg^{2+} respectively was used for testing. The content of ions in permeate was determined by means of atomic absorption technique. Filtration was carried out at 2 bar. Sugar beet juice (PC "Salyvonkivskyy sugar factory") was also applied to investigations. Before testing, juice was diluted in 10 times. The content of vegetable proteins was determined in permeate using such dye as Coomassie brilliant blue G-250 [12]. Selectivity of membranes (φ), i.e. rejection of species was estimated via [1]:

$$\varphi = \left(1 - \frac{C_p}{C_f}\right) \times 100\%. \quad (1)$$

where C_p and C_f are the concentration of feeding solution and permeate, respectively.

11.3 Results and Discussion

11.3.1 Morphology of Membranes

As an example, typical SEM images of the pristine PAN membrane are given in Fig. 11.1a, b. It is seen that the microporous support consists of sprung fibers, a size of which is 10–20 μm. Active layer is attached to the support forming the membrane that is able to reject colloidal particles. During HZD precipitation, the particles, a size of which is up to 5 μm, are formed in the support, when MNP are absent (Fig. 11.1c).

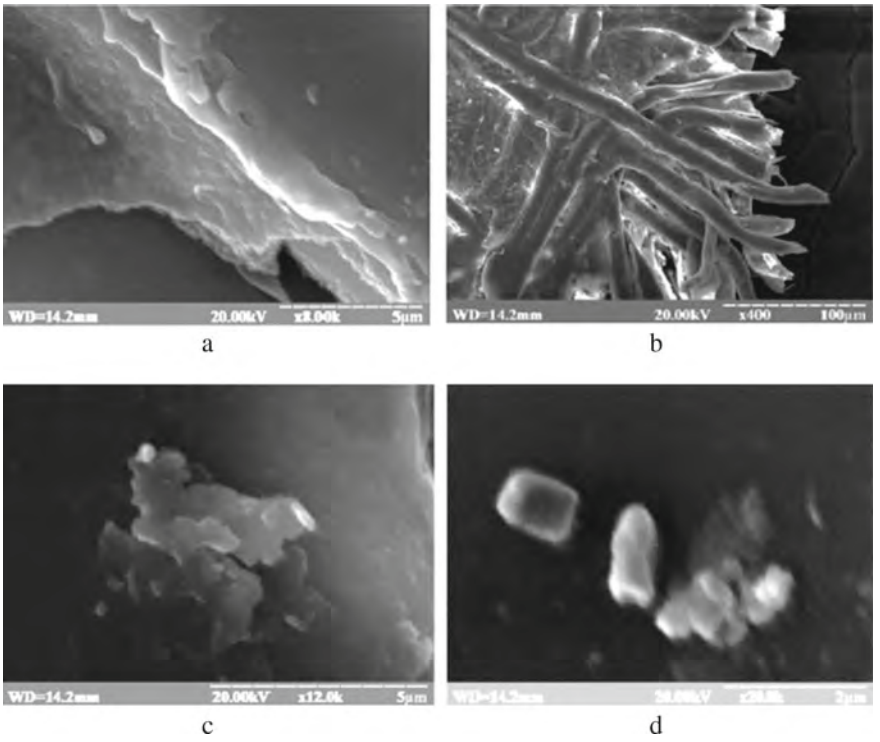

Fig. 11.1 SEM image of pristine (**a**, **b**) and modified (**c**, **d**) PAN membrane: active layer (**a**) and macroporous support (**b**–**d**). One-component HZD (**c**) and HZD containing MNP (**c**, **d**) were used as a modifier

In the case of MNP in sol, the size of aggregate is up to 2 μm (Fig. 11.1d). Analysis of fractal dimension gives 2.4–2.7 indicating diffusion as a limiting stage during aggregate formation. The mechanism involves sticking of particles to a small cluster (DLA model) [14]. In our case, MNP particles are evidently additional precipitation centers.

Indeed, the flux of particles (J) during precipitation is determined by Fick's law:

$$J = DgradC, \tag{2}$$

where D and C are the diffusion coefficient and the concentration of particles being formed. Formation of smaller particles causes increase of their concentration gradient, which moves from the outer sides of a membrane to its middle together with a precipitator. When deposition occurs, higher concentration gradient is realized for smaller particles. On the other hand, magnetic nanoparticles provide local magnetic fields inside membrane. As found for solutions of NaCl, KCl, $CaCl_2$ and Na_3PO_4, their conductivity increases under the influence of magnetic field [10]. The reason is suggested to be structuring water in hydrate shells of ions, this results in increase of their diffusion coefficient. It is possible to assume that bonded water around the particles is also structured promoting faster diffusion. Enhancement of particle movement affected by magnetic field leads to formation of smaller aggregates comparing with the case of MNP absence.

TEM image of the active layer (Fig. 11.2a) shows very small aggregates of nanoparticles (up to 20 nm). Dark contrast spots evidently correspond to MNP, grey traces are related to HZD.

For comparison, the image for MNP is also given. The shape of nanoparticles is seen to be close to globular. A size of the primary particles is about 10 nm. The size of aggregates embedded to the active layer corresponds to pore size of the polymer according to its rejection ability towards proteins, molecular mass of which is 50 kDa.

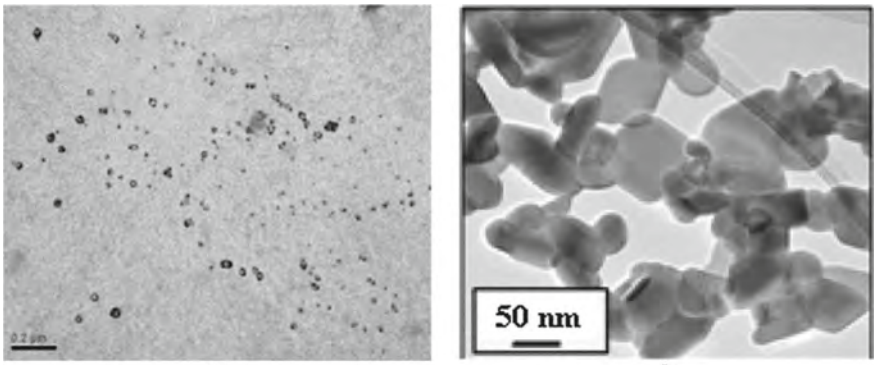

Fig. 11.2 TEM image of active layer of PAN membrane containing HZD and MNP (**a**). The image of MNP that are outside the membrane is also given (**b**)

11.3.2 Water Filtration. Secondary Active Layer

Figure 11.3 illustrates a volume of permeate (V) as a function of time of water filtration (τ).

As seen, the dependencies are linear. This allows us to estimate water flux (J) as:

$$J = \frac{dV}{d\tau}\frac{1}{A}, \tag{3}$$

where A is the membrane area. The calculation were made from the slopes of the lines to the abscissa axis, the results are given in Table 11.1.

As seen, the PAN membrane containing HZD and MNP shows lower permeate flux than the pristine membrane. due to filling of the polymer pores. At the same time, rejection of hardness ions becomes higher due to decrease of pore size in the active layer and charge effect. The φ values are similar for the membranes containing MNP and free from them. At the same time, the PS membranes show higher values

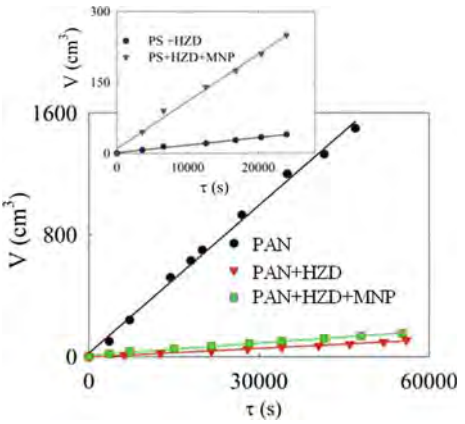

Fig. 11.3 Permeate volume as a function of time of water filtration through the pristine PAN membrane (PAN), PAN membrane containing HZD (PAN + HZD), PAN membrane containing HZD and MNP (PAN + HZD + MNP)

Table 11.1 Filtration of liquids at 2 bar

Membrane	Water		Sugar beet juice	
	J (m^3 m^{-2} s^{-1})	φ (%), Ca^{2+}, Mg^{2+}	J (m^3 m^{-2} s^{-1})	φ (%), VP
PAN	1.1×10^{-5}	6–7	1.1×10^{-6}	16–26
PAN + HZD	5.9×10^{-7}	8–19	3.8×10^{-7}	58–77
PAN + HZD + MNP	9.5×10^{-7}	7–20	4.3×10^{-7}	78–87
PS	2.3×10^{-5}	2–3	2.4×10^{-6}	6–13
PS + HZD	5.7×10^{-7}	5–7	5.5×10^{-7}	38–49
PS + HZD + MNP	3.6×10^{-6}	5–6	5.7×10^{-7}	55–60

of fluxes and lower rejection of Ca^{2+} and Mg^{2+}. It means that the PAN polymer membrane, which is characterized by smaller holes in active layer, is more attractive for modifying.

The inorganic particles form "secondary active layer" inside the polymer pores: this layer determines water flux and rejection ability of the membrane. Its thickness (l) was calculated from Kozeny–Carman equation [13]:

$$\frac{\Delta P}{l} = \frac{180\mu(1-\varepsilon^2)}{\Phi^2 d^2 \varepsilon^3} \text{ J.} \tag{4}$$

where ΔP is the pressure drop, ε is the porosity (0.33 for compact bed of globules), Φ is the particle sphericity (it is assumed that $\Phi = 1$), d is the particle diameter ($\approx$10 nm), μ is the dynamic viscosity (9×10^{-3} Pa s at 298 K). The calculations give $l \approx 0.58$ μm both for the PS and PAN membranes containing HZD. This value is comparable with a thickness of active layer of the membrane. Regarding the membranes containing also MNP, $l = 95$ nm (PAN) and 0.87 μm (PS). Thus, thinner "secondary active layer" is formed in the polymer matrix containing smaller pores. In the case of PS, the nanosized inorganic particles are dispersed through the polymer active layer.

11.3.3 Filtration of Sugar Beet Juice

In all cases, filtration of sugar beet juice caused its clarification. Vegetable proteins partially penetrated into the permeate (see Table 11.1). Modifying was shown to improve ability of the membranes to reject this valuable component. Higher φ values were found for the membranes containing MNT. As seen from Fig. 11.4, the V-τ dependences can be fitted with linear functions (organic-inorganic membranes) or tend to plateau formation (pristine membrane).

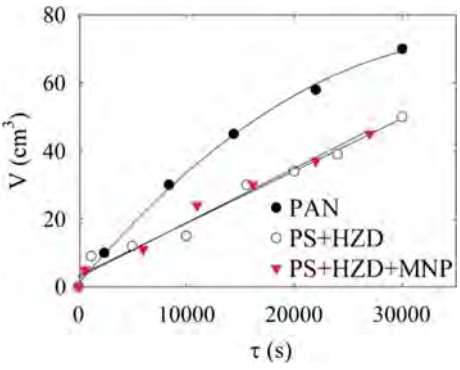

Fig. 11.4 Permeate volume *vs* time of filtration of sugar beet juice

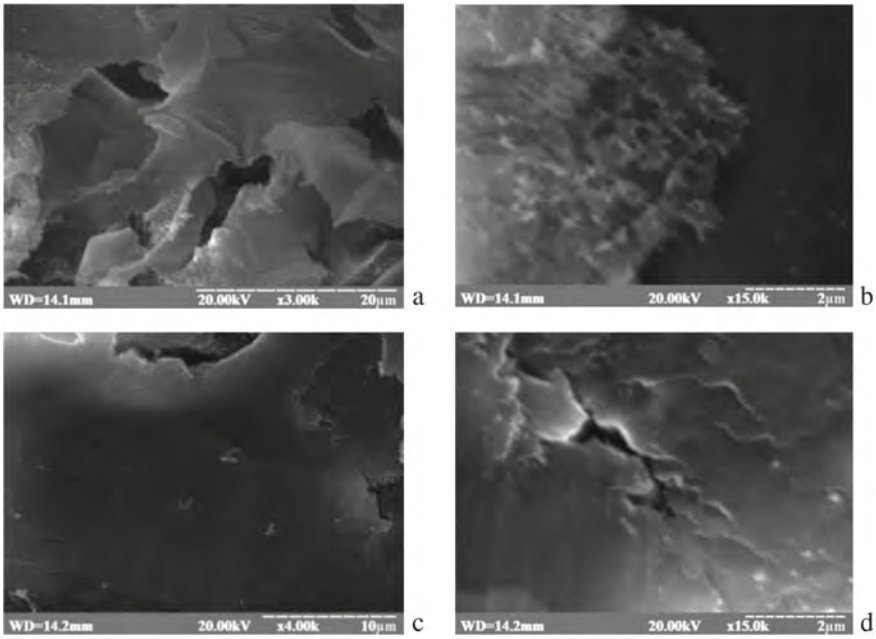

Fig. 11.5 SEM images of the samples after filtration of sugar beet juice: pristine PAN membrane (**a**, **b**), membrane modified with HZD (**c**), HZD and MNT (**d**)

The depression of filtration is due to fouling with organics: the precipitate is seen as a web-like patina (Fig. 11.5). At the same time, the outer surface of the organic-inorganic membrane remains clean.

11.4 Conclusions

When hydrated zirconium dioxide is deposited in ultrafiltration polymer membranes, aggregates of the nanoparticles are formed both in macroporous support and active layer. MNP provides formation of smaller HZD particles. Fractal analysis shows the DLA model of particle formation. The function of MNP is assumed to accelerate diffusion of HZD nanoparticles being precipitated. This depresses enlargement of the aggregates, As a result of modifying, the composite membrane shows slight improvement of rejection of hardness ions and much higher rejection of vegetable proteins comparing with pristine membranes. The modifying effect is most expressed for the PAN polymer membrane, which is characterized by smaller pores through its active layer comparing with the PS membrane. The composites also demonstrate stability against fouling with organics due to additional hydrophilization of polymer support. The membranes can be recommended for water treatment and processing

of feedstock and wastes of food industry. The composites also demonstrate stability against fouling with organics due to additional hydrophilization of the polymer support similarly to [5, 15].

Acknowledgements This work was performed within the framework of the project entitled "Baro- and electromembrane processes in technologies for purification of liquid media produced by food technologies" (grant number 0117U001247 supported by the Ministry of Education and Science of Ukraine). The work was also supported by the joint Ukrainian-Belorussian project that is called "Development of composite ultra- and nanofiltration membranes with predetermined functional properties for complex processing of wastes of food industry" (supported by the National Academy of Science of Ukraine and by the National Academy of Science of Belarus). The authors thank Dr. S. Scherbakov (M.G. Kholodnii Institute of Botany of the NAS of Ukraine) for his support of investigation using electron microscopes.

References

1. S. Adham, *Development of a Microfiltration and Ultrafiltration Knowledge Base* (AWWA Research Foundation and American Water Works Association, Denver, CO, 2005)
2. A.G. Belous, O.I. V'yunov, E.V. Pashkova, V.P. Ivanitskii, O.N. Gavrilenko, J. Phys. Chem. B **110** (2006)
3. C. Douketis, Z. Wang, T. Haslett, M. Moskovits, Phys. Rev. B **51** (1995)
4. Y. Dzyaz'ko, L. Rozhdestvenskaya, A. Pal'chik, Russ. J. Appl. Chem. **78** (2005)
5. Y. Dzyazko, L. Rozhdestvenskaya, Y. Zmievskii, A. Vilenskii, V. Myronchuk, L. Kornienko, S. Vasilyuk, N. Tsyba, Nanoscale Res. Lett. **10** (2015)
6. Y. Dzyazko, L. Ponomaryova, Y. Volfkovich, V. Trachevskii, A. Palchik, Microporous Mesoporous Mater. **198** (2014)
7. Y. Dzyazko, A. Rudenko, Y. Yukhin, A. Palchik, V. Belyakov, Desalination **342** (2014)
8. Y. Dzyazko, Y. Volfkovich, V. Sosenkin, N. Nikolskaya, Y. Gomza, Nanoscale Res. Lett. **9** (2014)
9. N. Ghaemi, S. Madaeni, P. Daraei, H. Rajabi, S. Zinadini, A. Alizadeh, R. Heydari, M. Beygzadeh, S. Ghouzivand, Chem. Eng. J. **263** (2015)
10. L. Holysz, A. Szczes, E. Chibowski, J. Colloid Inter. Sci. **316** (2007)
11. Y. Huang, C. Xiao, Q. Huang, H. Liu, J. Hao, L. Song, J. Membrane Sci. **548** (2018)
12. H. Mæhre, L. Dalheim, G. Edvinsen, E. Elvevoll, I.-J. Jensen, Foods **7** (2018)
13. W. MacCabe, P. Harriott, J. Smith, *Unit Operations Of Chemical Engineering* (McGraw-Hill Higher Education, Boston, MA, 2005)
14. P. Meakin, Physica D: Nonlinear Phenomena **86** (1995)
15. V. Myronchuk, Y. Dzyazko, Y. Zmievskii, A. Ukrainets, A. Bildukevich, L. Kornienko, L. Rozhdestvenskaya, A. Palchik, Acta Periodica Technologica (2016)
16. R. Pang, X. Li, J. Li, Z. Lu, X. Sun, L. Wang, Desalination **332** (2014)
17. Z. Rahimi, A.A. Zinatizadeh, S. Zinadini, J. Appl. Res. Water Wastewater **1** (2014)
18. J. Shen, H. Ruan, L. Wu, C. Gao, Chem. Eng. J. **168** (2011)
19. L. Upadhyaya, M. Semsarilar, A. Deratani, D. Quemener, J. Membrane Sci. Res. **3** (2017)
20. M. Zahid, A. Rashid, S. Akram, Z. Rehan, W. Razzaq, J. Membrane Sci. Technol. **8** (2018)

Chapter 15
Effect of Surface Modification of Sputtered Ta_2O_5 Magnetron Ceramic Coatings on the Functional Properties of Antigen-Presenting Cells In Vitro Tests

S. Yakovin, S. Dudin, A. Zykova, V. Safonov, A. Goltcev, T. Dubrava, and I. Rassokha

Abstract The effect of surface treatment of Ta_2O_5 nanostructured coatings by argon ions and electron beam on the functional potential of antigen-presenting cells of the monocyte-phagocytic system has been studied. The adhesive potential, indicators of phagocytic and metabolic activity of the studied cells depending on the surface properties of magnetron sputtered tantalum pentoxide coatings were analyzed. Electron irradiation process led to the stimulation of adhesive potential, phagocytic and metabolic activity of cells on the Ta_2O_5 coated surfaces. On the contrary, the surface treatment by argon ions significantly reduced the functional activity of the studied cells.

15.1 Introduction

The biological response to the artificial material is determined by a complex of factors. The important role is played not only by the physico-chemical characteristics of the biomaterial surface, but also by the total cells response on the cell/biomaterial interface [1, 2]. It is known, that first immune response on the implantation was recorded by cells of monocytic-phagocytic system of organism [3–5]. Macrophages play important role in the immune organism reactions on the implanted materials—catheters, stents, femoral and oral implants. Immune response on the artificial implants leads to the postoperative complications, inflammatory processes and the risk of repeated surgery operations. Inflammatory and anti-inflammatory reactions

S. Yakovin · S. Dudin (✉) · A. Zykova · V. Safonov
V. N. Karazin Kharkiv National University, Kharkiv, Ukraine
e-mail: dudin@karazin.ua

A. Zykova · V. Safonov
National Science Center "Kharkov Institute of Physics and Technology", Kharkiv, Ukraine

A. Goltcev · T. Dubrava · I. Rassokha
Institute for Problems of Cryobiology and Cryomedicine NASU, Kharkiv, Ukraine

A. D. Pogrebnjak et al. (eds.), *Nanomaterials in Biomedical Application and Biosensors (NAP-2019)*, Springer Proceedings in Physics 244,
https://doi.org/10.1007/978-981-15-3996-1_15

can be regulated by biomaterial properties and surface modifications [6, 7]. The aim of present study was to investigate the effect of surface treatment by argon ions and electron beam on the structure and surface properties of tantalum pentoxide (Ta_2O_5) coatings deposited by reactive magnetron sputtering method and further correlation of the surface characteristics with immune cells response.

15.2 Materials and Methods

Magnetron, inductively coupled plasma (ICP) source, and ion source were included in the technological system for synthesis of coatings [8]. The ICP source was designed to create activated flow of reactive gas molecules, as well as flow of low-energy ions and electrons. The ICP source was used to clean the surface of the samples before deposition and, in combination with the magnetron, for reactive deposition of metal oxides and nitrides. The ICP source was located inside the vacuum chamber that allows to choose the optimal ratio between the distances from the magnetron and the plasma source to the samples.

Volt-ampere characteristics of magnetron discharge with tantalum target in argon for different values of reactive gas flow were previously presented [9]. Figure 15.1 shows the dependence of the magnetron discharge voltage and current on the oxygen flow. With the oxygen flow rise, the voltage increases, and the discharge current falls in the case of the tantalum target.

With the oxygen flow increasing, the discharge shifts to the poisoning mode with reduced deposition rate. On the other hand, non-stoichiometric coatings are formed in the case of insufficient oxygen flow. The technological process allows deposition of stoichiometric transparent coatings in the metallic mode of the magnetron target far from the poisoning mode.

The ion source "Radical M" of medium energies (0.5–3 keV) was used to clean and activate the surface of the samples before the coatings deposition, as well as

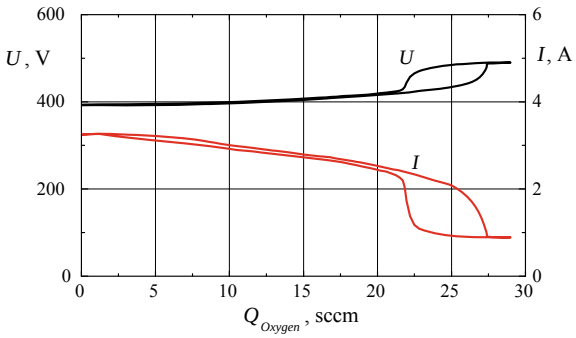

Fig. 15.1 Dependencies of the magnetron discharge voltage and current on the oxygen flow Q_{Oxygen} in the case of the tantalum target

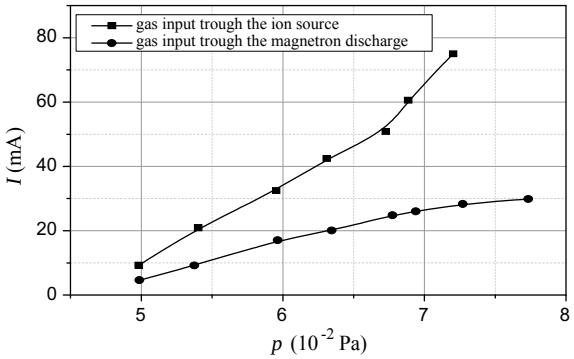

Fig. 15.2 Dependence of the discharge current of the ion source on the gas pressure in the process chamber upon gas input into the magnetron discharge or to the ion source

ion assistance in the process of film synthesis. There is a possibility to change the density, morphology and stoichiometrical composition of the coatings during deposition process by controlling the energy, current density and composition of the ion beam. The influence of gas pressure and flow rate on the current-voltage characteristics was analyzed.

The plots shown in Fig. 15.2 correspond to the technological regime of coatings deposition starting from the minimum gas pressure of 5×10^{-2} Pa for the gas input to the magnetron discharge. As can be seen from the figure, it is possible to control the current density of ions in wide range regulating the amount of gas passing through the ion source or through the magnetron discharge. The allowable range of the current density regulation reaches from 0.1 to 10 mA/cm^2 at a constant average energy of ions.

Ta_2O_5 coatings were deposited on Petri dishes glass substrates in a high vacuum pumping system with a base pressure of about 10^{-4} Pa by ion-assisted magnetron sputtering. Oxygen for the reactive deposition was delivered through the ICP plasma source $Q = 60$ sccm, magnetron voltage was $U = 700$ V, magnetron current was about $I = 5.7$ A.

For other substrates, the deposition process was carried out with simultaneous bombardment of the growing film by argon ions using the ion source. The ion source parameters were as follows: magnetic coil current 1.5 A, ion acceleration voltage 2.5 keV, ion source current 30 mA.

In electron bombardment research the electron beam was created by electron gun of type UL-119. The electrons energy was 20 keV, current density on the sample surface 14 μA/cm^2, the irradiation time 1500 s.

The coating thickness was measured by Calotest. The roughness parameters of the oxide ceramic coatings were evaluated by profilometer Hommel. The surface morphology and topography were observed by scanning electron microscope JSM 5500 LV. The chemical composition of the coatings was analyzed by energy dispersive X-ray (EDX) spectroscopy (Oxford Link ISIS 300). Advancing contact

angles and wettability of the coated surfaces were evaluated by tensiometric measurements (Kruss 12). The total surface free energy, polar and dispersion parts were estimated by Owens-Wendt-Rabel-Kaeble methods.

Adhesive and proliferative activity of immune cells was evaluated by standard protocols. Phagocytes of peritoneal cavity of mice CBA/H line were isolated and cultivated on the coated substrates. The phagocytes cells were cultured with density 1×10^7 cells per dish on the control and oxide coated glass Petri dishes in an CO_2 incubator (5% CO_2) at 37 °C and 95% humidity. Cell adhesive potential was evaluated after 30 min of cultivation on coated/uncoated substrates. After the indicated time, non adhesive cells were removed by washing the tested substrates twice with Hanks solution. Adherent cells were fixed with methanol for 5 min and counted. Visual control of the cell cultures was carried out using a light phase contrast microscope «Primo Star» («Zeiss», Germany) and inverted microscope «Axiovert 40C» («Zeiss», Germany). Statistical analysis of test results was performed using the nonparametric Mann-Whitney U test. The difference was considered statistically significant at $P < 0.05$.

15.3 Results and Discussion

The deposition process carried out with simultaneous bombardment by argon ions was resulted in the structural changes of the growing films.

Also, the changing of surface topography and roughness parameters of the oxide ceramic coatings was evaluated by scanning electron microscopy. The coating thickness and cross-section structure were obtained from the SEM cross-section measurements (Fig. 15.3).

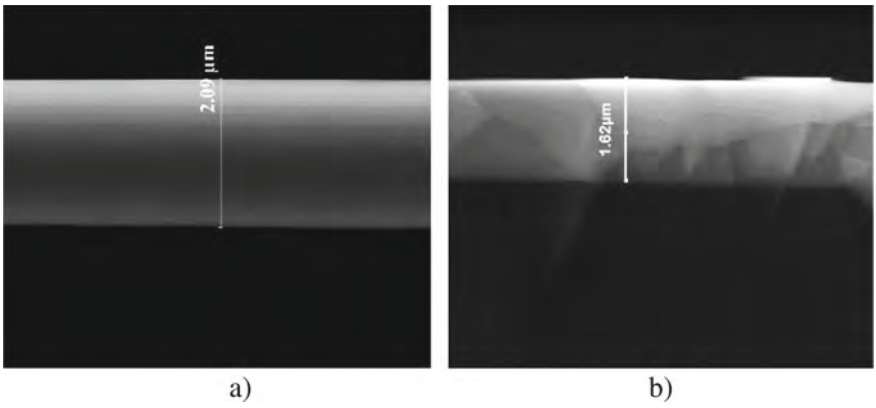

Fig. 15.3 SEM cross-section images of as-deposited oxide ceramic coatings: **a** Ta_2O_5 coatings, **b** Ta_2O_5 coatings deposited with simultaneous bombardment by argon ions

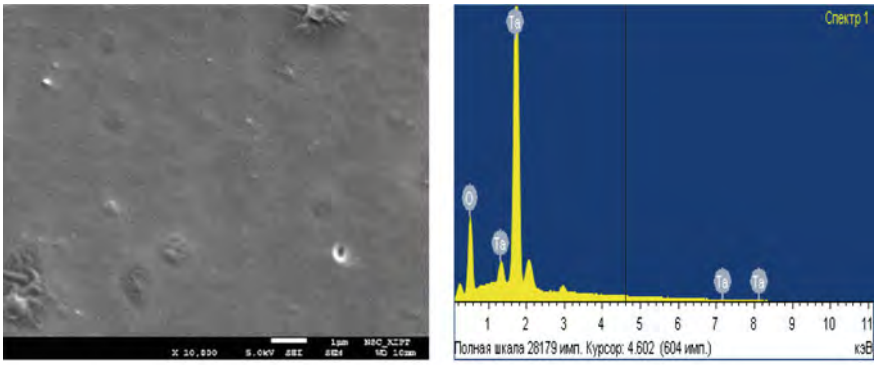

Fig. 15.4 SEM surface images and EDX spectra of Ta_2O_5 coatings: **a** Ta_2O_5 coatings surface, **b** EDX spectra

Scanning electron microscopy images of the magnetron sputtered Ta_2O_5 ceramic coatings have revealed a relatively flat surface with no cracks. EDX spectra demonstrate the stoichiometric composition of magnetron sputtered tantalum pentoxide coatings (Fig. 15.4).

The difference of structure parameters of Ta_2O_5 coatings and Ta_2O_5 coatings deposited with simultaneous bombardment by argon ions was described in [10]. The coatings had a nano-globular structure with characteristic sizes of structural elements of about 15 nm in the case of tantalum pentoxide films without additional treatment and 20 nm with argon ion bombardment of the growing films.

The thickness and roughness parameters of as-deposited coatings, after simultaneous bombardment by argon ions and electron beam post treatment are presented (Table 15.1).

The roughness parameters were principally changed during argon ions bombardment: roughness $Ra = 0.017$ μm, $Rz = 0.240$ μm in the case of Ta_2O_5 coatings, $Ra = 0.035$ μm, $Rz = 0.490$ μm in the case of Ta_2O_5 coatings deposited with simultaneous bombardment by argon ions. In contrast, the post-treatment processing by electron beam created by electron gun was not resulted in the principal changing of surface and structural parameters of oxide ceramic coatings. The structure of electron beam irradiated coatings was similar to as-deposited coatings, roughness parameters

Table 15.1 Thickness and roughness parameters

Substrate/coating	Thickness (μm)	Roughness Ra (μm)	Roughness Rz (μm)
Glass/Ta_2O_5	2.09	0.017	0.240
Glass/Ta_2O_5 (electron beam irradiation)	2.09	0.014	0.210
Glass/Ta_2O_5 (argon ions bombardment)	1.62	0.035	0.490

Table 15.2 The surface free energy SFE and its polar and dispersion parts by Owens-Wendt-Rabel-Kaeble method

Substrate/coating	γ (mN/m)	γ^d (mN/m)	γ^p (mN/m)
Glass	56.28	30.31	25.97
Glass/Ta_2O_5	43.96	31.06	12.90
Glass/Ta_2O_5 (electron beam irradiation)	48.37	32.16	16.21
Glass/Ta_2O_5 (argon ions bombardment)	41.11	30.03	11.08

were $Ra = 0.014$ μm, $Rz = 0.210$ μm close to the case of Ta_2O_5 coatings in good agreement with previous results [9].

Variation of structural parameters may lead to a change of surface characteristics and functional properties of deposited coatings. X-ray diffraction profiles of as-deposited Ta_2O_5coatings demonstrated an amorphous nature for as-deposited magnetron sputtered Ta_2O_5 coatings, no peaks were observed.

XPS survey spectra of the ceramic Ta_2O_5 coatings deposited by magnetron sputtering method were previously analyzed [11]. All spectra consist of well-defined XPS lines of Ta 4f, 4d, 4p and 4s; O 1s; C 1s. Ta 4f doublets are typical for Ta_2O_5 coatings with two main peaks. Ta 4f doublets are typical for Ta_2O_5 coatings and have two peaks: Ta 4f7/2 at ~26.5 eV and Ta 4f5/2 whose binding energy is higher by 1.9 eV. The Ta 4f lines of the deposited films are in a good agreement with the Ta 4f doublet representative of the Ta-O bond in Ta_2O_5. The Ta/O ratio estimated from the spectra was about 0.4 for all investigated coatings. The O 1s peaks are centred at binding energies 530.6 eV for the deposited Ta_2O_5 coatings.

The surface free energy (SFE) plays an important role in the mechanism of cell/biomaterial response [12]. The SFE and its polar and dispersion parts were estimated by Owens-Wendt-Rabel-Kaeble method for liquid system: α-bromonaphthalene–formamide–ethylene glycol–diidomethane–glycerol–water (Table 15.2) at temperature 20 °C.

The data demonstrate that the surface free energy of Ta_2O_5 coatings was in the range 40-50 mN/m and SFE polar parts were in the range 11–16 mN/m. Tantalum pentoxide ceramic coatings deposited with simultaneous bombardment by argon ions possess the minimal values of SFE.

The data demonstrate (Table 15.2) that the properties of oxide ceramic coatings shift in the more hydrophilic region and values of the surface free energy increase for the oxide coated substrates after electron beam irradiation post-treatment.

The topographic and physico-chemical characteristics of the surface act as factors that modulate the adhesive potential of cells [13]. The adhesive potential of phagocytes cells of the peritoneal cavity of CBA/H mice depending on the surface properties of tantalum pentoxide coatings was analysed. Table 15.3 shows the results of studying the adhesive potential of the phagocytes of the peritoneal cavity of CBA/H mice on glass (control) and Ta_2O_5 coatings before and after surface treatment by electrons and argon ions.

Table 15.3 Adhesive potential of the phagocytes cells on glass and Ta_2O_5 coated substrates

Substrate/coatings	Adhesive potential of phagocytes cells, %	Percent of adhesive cells, %
Glass (control)	3.76 ± 0.34	100
Glass/Ta_2O_5	$2.66 \pm 0.20^*$	70.74^*
Glass/Ta_2O_5 (electron beam irradiation)	$4.99 \pm 0.43^*$	132.70^*
Glass/Ta_2O_5 (argon ions bombardment)	$2.61 \pm 0.14^*$	69.41^*

*The difference statistically significant to control, $P < 0.05$

The minimal values of cell adhesive potential in the case of Ta_2O_5 coatings deposited with simultaneous bombardment by argon ions were observed (Table 15.3). Adhesive potential of phagocyte cells on the Ta_2O_5 coated surface after electron irradiation was 30% higher than on the uncoated surface (glass substrates). Thus, the electron irradiation process led to the stimulation of adhesive potential, phagocytic and metabolic activity of cells on the Ta_2O_5 coated surfaces. On the contrary, the surface treatment by argon ions significantly reduced the functional activity of the antigen-presenting cells. The effect of material surface modification on the several inflammatory events in vivo was previously observed [14, 15]. Macrophages preferentially accumulate on rough surface in vitro [16]. A correlation between a decreasing number of interfacial ED1 positive macrophages and increasing surface roughness was found after one week, but not after 6 and 12 weeks. In present study, the surface roughness increasing after argon ions bombardment did not lead to the significant increasing of adhesive potential of phagocyte cells in vitro tests. On the contrary, the changing of surface free energy, polar part parameters, and shift to more hydrophilic region can effect on the increasing of adhesive potential, phagocytic and metabolic activity of cells after electron irradiation process.

15.4 Conclusions

The deposition process carried out with simultaneous bombardment by argon ions and post-treatment by electron irradiation were resulted in structural changes of the growing films. The change of structural parameters leads to changing of coatings surface characteristics.

The roughness parameters were significantly increased in the case of Ta_2O_5 coatings deposited with simultaneous bombardment by argon ions. In contrast, the post-treatment by electron beam was not resulted in the principal change of roughness parameters. The structure of electron beam irradiated coatings was similar to as-deposited Ta_2O_5 coatings.

Tantalum pentoxide ceramic coatings deposited with simultaneous bombardment possess the minimal values of SFE. The Ta_2O_5 coatings demonstrate more hydrophobic properties after surface treatment by argon ions. On the contrary, properties of tantalum pentoxide ceramic coatings shift in the more hydrophilic region and values of the surface free energy increase for the coated substrates after electron beam irradiation post-treatment.

It was shown that the argon ions bombardment during tantalum pentoxide coating deposition process reduces adhesive and proliferative potential of antigen-presenting cells. On the contrary, electron irradiation process led to the stimulation of adhesive potential, being a primary link in providing functional (phagocytic and metabolic) activity of these cells on the Ta_2O_5 coated surfaces. The change of surface free energy, polar part parameters, and shift to more hydrophilic region can lead to the increasing of functional activity of cells of monocytic-phagocytic system after electron irradiation process.

Results demonstrate that surface modification can affect the adhesive potential of immune cells that is important for further clinical applications.

Acknowledgements The research was supported by the international scientific cooperation program between National Academy of Science of Ukraine and National Academy of Science of Belorussia # 17-03-18.

References

1. T.A. Blaine, J. Bone Jt. Surg. **78-A**(8), 1181 (1996)
2. C.M. Takebe, A. Champagne, A. Diener, B. Nebe, F. Luthen, P. Becker, U. Beck, H.G. Neumann, J. Rychly, Biomaterials **26**(4), 383 (2005)
3. M. Bartneck, K.H. Heffels, Y. Pan, M. Bovi, G. Zwadlo-Klarwasser, J. Groll, Biomaterials **33**, 4136 (2012)
4. C.A. Janeway, R. Medzhitov, Annu. Rev. Immunol. **20**(1), 197 (2002)
5. P. Thomsen, C. Gretzer, Curr. Opin. Solid State Mater. Sci. **5**, 163 (2001)
6. C.R. Jenney, J.M. Anderson, J. Biomed. Mater. Res. **49**, 435 (2000)
7. S. MacLauchlan, E.A. Skokos, N. Meznarich, D.H. Zhu, S. Raoof, J.M. Shipley, R.M. Senior, S. Offenbacher, K. Ishibashi, L.F. Cooper, J. Biomed. Mater. Res. **64 A**(2), 207 (2003)
8. S. Yakovin, S. Dudin, A. Zykov, V. Farenik, Problems At. Sci. Technol. Ser. "Plasma Physics" **71**(1), 152 (2011)
9. A. Zykova, V. Safonov, A. Goltsev, T. Dubrava, I. Rossokha, N. Donkov, S. Yakovin, D. Kolesnikov, I. Goncharov, J. Phys: Conf. Ser. **700**, 012027 (2016)
10. A. Zykova, V. Safonov, A. Goltsev, T. Dubrava, I. Rossokha, J. Smolik, R. Rogovska, S. Yakovin, D. Kolesnikov, I. Sudzhanskaya, I. Goncharov, Surf. Coat. Technol. **301**, 114 (2016)
11. N. Donkov, E. Mateev, A. Zykova, V. Safonov, D. Kolesnikov, I. Goncharov, I. Sudzhanskaya, S. Yakovin, J. Phys: Conf. Ser. **558**, 012036 (2014)
12. N.J. Hallab, K.J. Bundy, K. O'Connor, R.L. Moses, J.J. Jacobs, Tissue Eng. **7**(1), 55 (2001)
13. K. Anselme, P. Linez, M. Bigerelle, D. Le Maguer, A. Le Maguer, P. Hardouin, H.F. Hildebrand, I. Alain, J.M. Leroy, Biomaterials **21**, 1567 (2000)

14. A.S. Shanbhag, J.J. Jacobs, J. Black, J.O. Galante, T.T. Glant, J. Biomed. Mater. Res. **28**, 81 (1994)
15. M. Werthen, A. Sellborn, M. Kalltorp, H. Elwing, P. Thomsen, Biomaterials **8**, 827 (2001)
16. A. Rich, A.K. Harris, J. Cell Sci. **50**, 1 (1981)

Chapter 16
Features of Bacterial Cellulose Hydroxyapatite Nanocomposites Obtained by Two Different Techniques

A. Talipova, A. Kistaubayeva, A. Pogrebnjak, A. Turlybekuly, I. Savitskaya, and S. Saidildina

Abstract Nanocomposite material based on bacterial cellulose and hydroxyapatite was obtained using the biomimetic mineralization method (imitation of the formation of the mineral component in natural bone tissue) and the synthesis of hydroxyapatite nanoparticles in the presence of fibrillar fragments of BC. The biocomposite BC/HA-1 obtained by biomineralization showed high physicochemical parameters compared with the composite obtained by synthesis of hydroxyapatite nanoparticles in the presence of fibrillar fragments of BC (BC/HA-2). The ultimate tensile strength of the composite BC/HA-1 was 92.07 + 1.4 MPa, the composite BC/HA-2 was 76.09 + 1.1 MPa. Young's modulus (the coefficient of proportionality between stress and strain) of the BC/HA-1 composite was 59.04 + 0.6 MPa (BC/HA-1), which is 18.6% higher than that of the BC/HA-2 composite (48.03 + 0.8 MPa).

16.1 Introduction

Attention to the creation of artificial composite materials, close to the natural bone tissue, is growing rapidly and an important problem is to obtain a composite that would be as close as possible in its structure and properties to its natural counterpart. The primary role is given to composite materials based on natural polymers (cellulose, collagen, chitosan, chitin etc.) as a substitute for collagen and hydroxyapatite (HA) nanocrystals as the main mineral component of natural bone tissue. As one of the most common biodegradable and biocompatible natural polymers, cellulose has attracted considerable attention for the application of bone scaffolds.

A. Talipova (✉) · A. Kistaubayeva · I. Savitskaya · S. Saidildina
Al-Farabi Kazakh National University, Almaty, Kazakhstan
e-mail: talipova.aizhan@gmail.com

A. Pogrebnjak
Department of Nanoelectronics, Sumy State University, Sumy, Ukraine

A. Turlybekuly
East Kazakhstan State Technical University named after D. Serikbayev, Oskemen, Kazakhstan

A. D. Pogrebnjak et al. (eds.), *Nanomaterials in Biomedical Application and Biosensors (NAP-2019)*, Springer Proceedings in Physics 244,
https://doi.org/10.1007/978-981-15-3996-1_16

Bacterial cellulose (BC) is a unique natural polymer consisting of fibers with a diameter of 20–175 nm, forming a nano-gel film that has a specific inner surface area of at least 500 m^2/g [1]. BC has unique properties that are absent in plant [2]. Unlike plant cellulose, BC is a chemically pure extracellular product, as it does not contain lignin, hemicellulose, pectin and wax. BC has a high degree of crystallinity, its density is 300–900 kg/m^3, has high mechanical strength (up to 20 MPa), absorbs and holds up to 20 g of water per 1 g of dry polymer [3–6].

Along with other natural polymers, bacterial cellulose has unique physico-chemical and sorption characteristics, which makes it a promising material as the basis for a bone implant.

As a precursor of bone tissue, a composite based on BC and hydroxyapatite nanocrystals (HA), which is biocompatible with living organisms, is considered promising. The possibility of directed synthesis of a BC and the inclusion of various additives in it allows us to consider such materials as a universal biomaterial for bone and tissue engineering in general [7–9].

Due to its composition, structure, and unique physico-biological characteristics, materials based on hydroxyapatite are widely used in medicine in the form of ceramics, cements, and composites. They are used in the restoration of bone and dental tissue defects and spinal surgeries, as eye and ear implants, in bone grafting in maxillofacial operations, in the form of coatings for metal implants, etc.

However, prior to clinical trials, it is necessary to conduct detailed studies of the structure of both individual components and composites as a whole, which will help in explaining the behavior of the material in vitro and in vivo studies.

16.2 Materials and Methods

The bacterial strain *Komagataeibacter xylinus* C-3 was obtained from the collection cultures of the Department of Biotechnology of the Al-Farabi Kazakh National University.

16.2.1 Synthesis of Gel Film BC

The synthesis of cellulose strains of acetic acid bacteria was carried out on nutrient media containing aqueous solutions of yeast extract, glucose, peptone, ethanol and beer wort in concentrations established by optimizing the nutrient medium with a pH of 5.9–6.0. A 48-h culture of acetic acid bacteria grown on a medium containing yeast extract and beer wort in a 1: 1 ratio with 2 wt% glucose 1 vol. % ethanol. Cultivation was carried out at 30 °C for 5 days, after which the cellulose was separated and periodically washed with 0.5–1% aqueous NaOH solution while boiling until the cells were removed. Then, the cellulosic film was washed from the NaOH solution with distilled water, 0.5% acetic acid solution and again distilled water until neutral.

The resulting cellulose was stored as a gel film in distilled water at 5 °C [10]. The biomass of the BC films was determined after preliminary drying in a thermostat with a dry heat at 80 °C to a constant mass of the sample.

16.2.2 Development of Composite BC/HA

Nanocomposite material based on bacterial cellulose and hydroxyapatite was obtained using the biomimetic mineralization method (imitation of the formation of the mineral component in natural bone tissue) and the synthesis of hydroxyapatite nanoparticles in the presence of fibrillar fragments of BC.

Biomimetic mineralization method. For this, a polyvinylpyrrolidone (PVP) solution was prepared by adding 0.1 g of PVP to 500 ml of distilled water. Pre-obtained gel films of BC, were treated in PVP solution at 28 °C for 2 days. Then the PVP-treated BC-membrane was washed several times in distilled water. Next, these films were immersed in 0.1 mol/l $CaCl_2$ at 37 °C for 3 days to activate the hydroxyl group. To induce the formation of HA, modified PVP and activated Ca^{2+} BC were soaked in simulated body fluid (SBF) solution at 37 °C for 5 days. The SBF solution was prepared according to the protocol developed by WAN et al. The resulting HA/BC nanocomposites were washed with distilled water and dried [9].

Synthesis of hydroxyapatite nanoparticles in the presence of fibrillary fragments of BC suspension was carried out by co-disintegrating aqueous suspensions of BC and hydroxyapatite nanoparticles. Disintegration was performed in a laboratory blender for 15 min at a rotation speed of 2000 rpm. Then the volume of the reaction mixture was adjusted to 200 ml with distilled water and a portion of calcium oxide was added with vigorous stirring. The resulting mixture was homogenized for 5 min, and then the synthesis of HA nanoparticles was carried out by adding phosphoric acid (at a given rate of ~1 ml/min) to the resulting aqueous suspension of BC and $Ca(OH)_2$. The reaction was considered complete when reaching pH = 6.8–7.0.

16.2.3 Scanning Electron Microscopy (SEM) Studies

The structure of samples of films of bacterial cellulose and composite was examined by field emission scanning electron microscope JSM-7800F (Jeol, Japan). Prior to the SEM observation, the films were sputter coated with a platinum-palladium alloy (Pt/Pd 80/20).

16.2.4 The Study of the Strength of Films of Bacterial Cellulose and Composite BC/HA

Strength was determined on an "Instron" machine with a uniaxial mode in terms of maximum tearing load (kg), breakage stress (MPa), elongation (%). The young's modulus of the films was determined by tensile strength with the standard test ASTM D-882-97.

16.2.5 Statistical Analysis

Statistical comparison was performed using unpaired t-test and one-way analysis of variance (ANOVA) followed by Dunnett's test for multiple comparisons. All statistical analyses were performed using SPSS 16.0 software package (SPSS Inc., USA).

16.3 Results and Discussion

The structural properties, namely, the morphology of the surface of the gel film of the BC and the BC/HA composite, the diameter and location of the microfibrils of the polymer relative to each other were examined by field emission scanning electron microscope JSM-7800F (Jeol, Japan). Figure 16.1 shows electron micrographs of the dehydrated film of BC and composites BC/HA-1, BC/HA-2.

As shown in Fig. 16.1a, the BC has an ultrathin three-dimensional nanoporous network structure consisting of nanoscale fibers, which provides an excellent basis for the formation of HA nanoparticles and facilitates cellular adhesion of bones when used in tissue engineering. After treatment of PVP with a solution and biomineralization, HA crystals formed on the fibers of the BC for 5 days (Fig. 16.1b). Figure 16.1b, c show of HA crystals are embedded as a rod-like shape in a BC fiber network, which facilitates cell adhesion and makes it promising for use as a biomaterial for bone replacement.

In addition, it is obvious the presence of a uniform distribution density of the fibers of the frame, which provides high strength films. Due to the correct location of the fibers, the degree of crystallinity of the films reaches more than 60%, and in order to break them, you need to apply a force of up to several kilograms per square millimeter. Mechanical strength is an important indicator of the quality of polymeric materials. The strength of the films and the composite was determined on a universal tensile testing machine "Instron" in uniaxial mode by tensile strength (MPa), elongation (%) under tension. For this purpose, samples were prepared in the form of strips with a size of 65 × 10 mm. The tests were carried out at a temperature of (25 ± 2) °C and a relative humidity of (55 ± 5) %, with a sample deformation rate

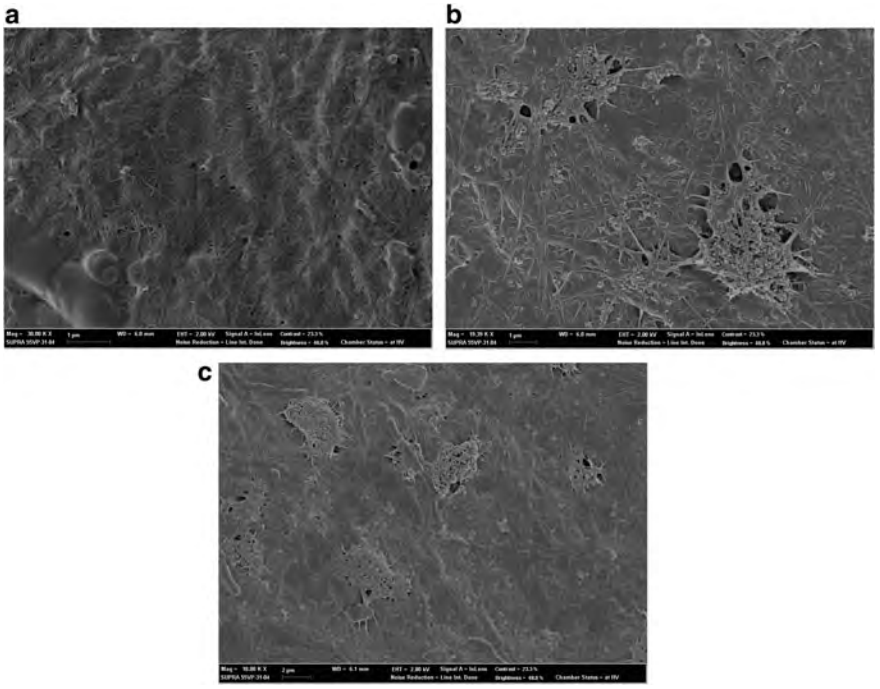

Fig. 16.1 SEM images of BC (**a**) films; BC/HA-1 composite obtained by biomineralization (**b**); BC/HA-2 composite obtained by synthesizing hydroxyapatite nanoparticles in the presence of fibrillar fragments of BC (**c**)

of 100 mm/min. Young's modulus (modulus of longitudinal elasticity) of the samples was determined by tensile strength with standard test ASTM D-882-97, designed to determine the strength of thin plastic films. The results of the study are shown in Table 16.1.

Table 16.1 Physico-chemical properties of BC/HA composite materials

Composite BC/HA	1 method	2 method
Density (g/cm^3)	61 ± 0.5	52 ± 0.3
Porosity (%)	0.55 ± 0.01	0.42 ± 0.02
Porevolume (cm^3/g)	79 ± 1.7	67.5 ± 1.9
Specific surface area (SSA) (m^2/g)	1.48 ± 0.07	2.04 ± 0.8
Ultimate tensile strength (MPa)	92.07 ± 1.4	76.09 ± 1.1
Young's modulus (MPa)	59.04 ± 0.6	48.03 ± 0.8

Thus, based on the research data, the ultimate tensile strength of BC/HA-1 samples is 92.07 ± 1.4 MPa, BC/HA-2 is 76.09 ± 1.1 MPa. This indicator of strength is associated with a high degree of crystallinity of BC, which provides resistance to high pressure (Backdahl 2006: 2141–2149). The Young's modulus of composites is 59.04 + 0.6 MPa and 48.03 ± 0.8 MPa.

The biocomposite BC/HA-1 obtained by biomineralization showed high physicochemical parameters compared with the composite obtained by synthesis.

According to the study, it can be said that the BC/HA-1 composite obtained by biomineralization is promising for use as a biomaterial for bone replacement.

16.4 Conclusion

The obtained biocomposite material based on the gel film of bacterial cellulose and hydroxyapatite. Nanocomposite material based on bacterial cellulose and hydroxyapatite was obtained using the biomimetic mineralization method (imitation of the formation of the mineral component in natural bone tissue) and the synthesis of hydroxyapatite nanoparticles in the presence of fibrillar fragments of BC. The biocomposite BC/HA-1 obtained by biomineralization showed high physicochemical parameters compared with the composite obtained by synthesis. The ultimate tensile strength of the composite BC/HA-1 was 92.07 ± 1.4 MPa, the composite BC/HA-2 was 76.09 ± 1.1 MPa. Young's modulus (the coefficient of proportionality between stress and strain) of the BC/HA-1 composite was 59.04 ± 0.6 MPa (BC/HA-1), which is 18.6% higher than that of the BC/HA-2 composite (48.03 ± 0.8 MPa). These indicators are quite high compared with the values of the Young's modulus of many flat oriented layers of organic polymers.

References

1. L.R. Lynd, P.J. Weimer, W.H.V. Zyl, I.S. Pretoriu, Microbial cellulose utilization: fundamentals and biotechnology. Microbiol. Mol. Biol. Rev. **66**, 506 (2002)
2. N. Shah, M. Ul-Islam, W.A. Khattak, J.K. Park, Overview of bacterial cellulose composites: a multipurpose advanced material. Carbohydr. Polym. **98**, 585–598 (2013)
3. A.S. Guzun, M. Stroescu, S.I. Jinga, G. Voicu, u A.M. Grumezesc, A.M. Holban, Plackett-Burman experimental design for bacterial cellulose-silica composites synthesis. Mater. SciEng. C Mater. Biol. Appl. **49**, 280 (2014)
4. W.C. Lin, C.C. Lien, H.J. Yeh, C.M. Yu, S.H. Hsu, Bacterial cellulose and bacterial cellulose-chitosan membranes for wound dressing applications. Carbohydr. Polym. **94**, 603–611 (2013)
5. R.D. Ruka, P.G. Simon, K. Dean, Altering the growth conditions of *Gluconoacetobacter xylinus* to maximize the yield of bacterial cellulose. CSIRO Mater. Sci. Eng. 1–21 (2015)
6. D.P. Romanov, YuG Baklagina, N.V. Lukasheva, A.K. Khripunov, A.A. Kachenko, V.K. Lavrentyev, Investigation of nanocomposites based on hydrated calcium phosphates and cellulose Acetobacter xylinum. J. Glas. Phys. Chem. **34**, 192–200 (2008)

7. M.J. Kim, M.J. Yeo, M. Kim, G.H. Kim, Biomimetic cellulose/calcium-deficient hydroxyapatite composite scaffolds fabricated using an electric field for bone tissue engineering. RSC Adv. **8**, 20637–20647 (2018)
8. T. Niamsapa, N.T. Lama and P. Sukyaia, Production of hydroxyapatite-bacterial nanocellulose scaffold with assist of cellulose nanocrystals. Carbohydr. Polym., 159–166 (2019)
9. N. Yin, S.Y. Chen, Y. Ouyang, L. Tang, J.X. Yang, H.P. Wang, Biomimetic mineralization synthesis of hydroxyapatite bacterial cellulose nanocomposites. Prog. Nat. Sci.: Mater. Int. **21**, 472–477 (2011)
10. Z. Cai, J. Kim, Bacterial cellulose/poly (ethylene glycol) composite: characterization and first evaluation of biocompatibility. Cellulose **17**, 83–91 (2010)

Chapter 17
Quality Parameters of Cellulose–Chitosan Based Edible Films for Probiotic Entrapment

D. H. Shokatayeva, A. Talipova, I. Savitskaya, A. Pogrebnjak, A. Kistaubayeva, and L. V. Ignatova

Abstract New carboxymethyl cellulose and chitosan edible films have been developed and characterized. Model probiotic bacteria *Lactobacillus rhamnosus* GG and *Lactobacillus acidophilus* AA-1 were incorporated after the film synthesis via bacteria diffusion and adsorption. The film formation and mechanical properties were characterized, as well as the viability of the entrapped bacteria. Inclusion of Ch in CMC film leads to a decrease in swelling ratio but increased rigidity of the films. Presence of Ch in such films inhibits bacteria incorporated in them. Overall, these novel CMC films are regarded as promising inexpensive and friendly matrices for food protection and packaging applications.

17.1 Introduction

Maintaining or improving quality and safety of food is one of the most important roles of its packaging. In the last decade, much attention has been paid to edible films and coatings. Edible films were performed thin layer materials that can be used as a coating to separated food components; food packaging; carrier for the delivery of active compounds or as packaging material for storing and protecting food [1]. In addition to barrier function, i.e. extending the shelf life and reducing the risk of pathogenic microorganisms growth on food products, such films can be considered as carriers of biologically active compounds [2]. It may be antioxidants, nutraceuticals, antimicrobials, flavors [3, 4]. Among them, probiotic bacteria are particularly relevant, since it is believed that these living microorganisms have a beneficial effect on the health of host, replenishing the natural gastrointestinal microbiota [5]. The inclusion of probiotics in polymer films can protect them from premature degradation and improve controlled release [6]. Although in the case of

D. H. Shokatayeva · A. Talipova (✉) · I. Savitskaya · A. Kistaubayeva · L. V. Ignatova
Al-Farabi Kazakh National University, Almaty, Kazakhstan
e-mail: talipova.aizhan@gmail.com

A. Pogrebnjak
Department of Nanoelectronics, Sumy State University, Sumy, Ukraine

A. D. Pogrebnjak et al. (eds.), *Nanomaterials in Biomedical Application and Biosensors (NAP-2019)*, Springer Proceedings in Physics 244,
https://doi.org/10.1007/978-981-15-3996-1_17

edible bioactive films and coatings, this is not even required, since it is assumed that the film/coating itself is consumed with food.

Edible films and coats are classified into three categories based on the components: hydrocolloids (polysaccharides, proteins, alginates); lipids and waxes; and composite films. Polysaccharides used for edible films or coatings are cellulose derivatives, dextrans, inulin, alginate, chitosan, carrageenan, starch derivatives, pectin derivatives [7, 8]. In recent years cellulose-based edible films are used for probiotic entrapment [9–11]. Carboxymethyl cellulose (CMC) is successfully used for these purposes most often [12, 13]. Films and coatings based on cellulose and its derivatives are transparent, flexible, odourless and tasteless. CMC is more resistant to water, however, the water vapor permeability is quite high. It can be reduced by creating a composite film with another biopolymer incorporated into it having high moisture barrier [14].

From this point of view, edible films and coatings obtained on the basis of chitosan (N-deacetylated derivative of chitin) deserve attention. Chitosan (Ch) is a biodegradable biopolymer having excellent film-forming and sorption properties. Therefore, it is often used for the manufacture of film packaging and food coatings [15]. The interesting fact that Ch was successfully used to create microcapsules with probiotics [16–19]. This is on the one hand. However, on the other hand, it has fungicidal and bactericidal properties [20, 21]. Thereby in this study were investigated physicochemical and biological properties of films with probiotic cells immobilized in edible films based on CMC and CMC + Ch. To the best of our knowledge, the potential use of such systems to entrap probiotic bacteria has never been explored before.

17.2 Materials and Methods

Preparation of bacteria *Lactobacillus rhamnosus* GG (LGG) was bought from the Belgian coordinated collection of microorganisms. Strain *Lactobacillus acidophilus* AA-1 (LA) isolated by our group from traditional yogurt was used. The strain was stored in glycerol (50%) at −20 °C. The stored cells were activated twice on MRS agar plates before use. After 48 h of growth, one colony was selected, inoculated into 20 ml MRS broth and incubated for 24 h at 37 °C. After this, the culture was transferred to fresh MRS broth and incubated at 37 °C for 18 h under anaerobic conditions. The cells were collected in the stationary growth phase by centrifugation at 6000 g for 15 min at 4 °C. The supernatant was discarded and cell pellet was washed twice with sterilized distilled water. The precipitate was resuspended in 3 ml of sterilized 0.85% sodium chloride solution. The concentration of cells after this treatment was around 2×10^{10} CFU/ml. Freshly prepared concentrated cell suspension was quantitatively evaluated by plating on MRS agar and used immediately.

Film formation Carboxymethyl cellulose (CMC) molecular weight 250 kDa with a degree of substitution 0.80–0.85 and Chitosan (Ch) of medium molecular

weight (100–300 kDa) and a degree of deacetylation of 75–85% were purchased from Sigma-Aldrich Chemie GmbH.

CMC was dissolved in a full dissolution water. The total polymer concentration was set to 2 wt%. The films were plasticized by incorporating 1 wt% glycerol into the polymer solution. This level of glycerol has been chosen to produce flexible films without excessive surface stickiness. After obtaining a clear solution, 15 g of it were poured into Petri dishes and allowed to cure in an oven at 50 °C for 20 h. The obtained films were removed from the glass plate and conditioned at 20 ± 1 °C and relative humidity 55 ± 1%.

Preparation of CMC/Ch film carried out by the "submerging" ex situ method. Ch powder was dissolved in an aqueous solution of 1% acetic acid to a final concentration of 0.6%. CMC films were placed in Ch solution and incubated for 6 h at room temperature. The excess of Ch solution was removed by placing obtained film between two sheets of filter paper. The whole procedure was performed using autoclaved (121 °C, 15 min) materials and under sterile conditions in a laminar air flow box. The films were stored in sterile vials with lids at 4 °C and used in further experiments.

Model probiotic bacteria (*L*GG and LA) were incorporated in the films after the film synthesis, via bacteria diffusion and adsorption. For this the films were soaked in a bacteria medium for 30 min at room temperature, then the excess of medium was removed to allow a moderate drying at 37 °C for 30 min.

To estimate the viable counts and matrix effect, the included in the film bacteria were released by resuspending 10 mg of film either in a PBS buffer solution (pH 7.4) at 37 °C for 30 min, under stirring. The viability of released cells was determined by plating serial dilutions of resulting suspension on MRS agar. Colony-forming units were counted after 48 h of anaerobic incubation at 37 °C. The total count of viable bacteria was expressed as log colony forming units per gram (log CFU/g, CFU/g = CFU/plate × dilution factor).

Mechanical tests The universal uniaxial tensile tester machine (Instron, USA) was used to access the mechanical properties of the films. Tensile grips with 35 mm were used to hold the specimens which consisted of 40 mm × 40 mm films. Up to four repetitions were made for each film formulation using a grip speed of 1.0 mm/s.

Moisture content The moisture content was assessed according to a gravimetric method. Pre-weighed aluminum pans containing edible films (approximately 0.5 g) were dried at 105 °C in hot air oven until they reached to constant weight. The moisture content was calculated using the following equation: Percentage of residual water content = $(W_i \times W_f)/W_i \times 100$, where w_i and w_f are the initial and final weight of the edible films, respectively.

Scanning electron microscopy (SEM) studies The surface morphology of lyophilized film samples was observed by field emission scanning electron microscope JSM-7800F (Jeol, Japan). Prior to the SEM observation, the films were sputter coated with a platinum-palladium alloy (Pt/Pd 80/20).

Statistical analysis Statistical comparison was performed using unpaired t-test and one-way analysis of variance (ANOVA) followed by Dunnett's test for multiple

comparisons. All statistical analyses were performed using SPSS 16.0 software package (SPSS Inc., USA).

17.3 Results and Discussion

A photograph of the films obtained by the procedure described in experimental section is presented in Fig. 17.1.

The films made from CMC alone or composite CMC/Ch film are reasonably flexible and transparent.

The inclusion of probiotic bacteria in a film is carried out in two ways: the incubation of finished films in bacterial suspension for a certain time or mixing of bacteria inoculum in a mixture of solutions of individual components (in our case CMC/Ch/glycerol before casting and hardening).

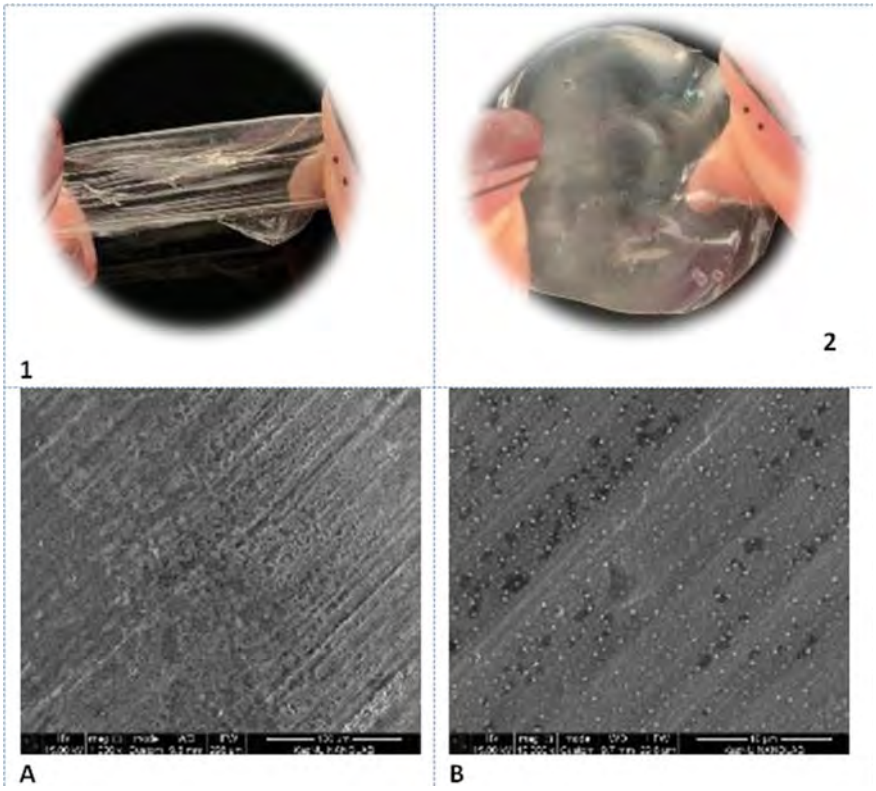

Fig. 17.1 **a** Photograph of CMC (1) and CMC/Ch (2) based films (1—CMC; 2—CMC/Ch) after being casted and dried in Petri dishes. **b** SEM images of different cross-linked films (1—CMC; 2—CMC/Ch)

In the first approach, bacteria should diffuse and adsorb to the film, in the second approach, it is expected that bacteria will be captured in a matrix of cellulosic polymer before casting and hardening [6]. However, since the films are not formed at temperatures below 50 °C, the viability of bacteria included by the second method can be significantly reduced [11]. In this connection, the first method was used in work, i.e. probiotic bacteria were immobilized in already finished films. *Lactobacillus rhamnosus* GG (LGG) and *L. acidophilus* AA-1 (LA) were selected as model bacteria.

The SEM results showed that the structure of control CMC and CMC/Ch films was homogeneous, uniform and compact with no micropores (Fig. 17.1). However, probiotic films showed a higher number of holes than control films. The bacterial cells were embedded in the film matrix (tiny rod-like shapes) that could result in increasing cell-protective effects of films (Fig. 17.2).

Edible films should be adequately resistant to external stresses to use as food packaging materials. Furthermore, films must be flexible and strong during packaging and storage. The obtained films were subjected to tensile tests in order to study their mechanical properties. Tensile strength (TS) and elongation at break (EB) are two key indicators of edible films used for packaging. The TS and EB of the control and probiotic films are shown in Table 17.1.

The CMC/Ch film presents the higher TS (maximum load at break) while the CMC is the weaker one. On the other hand, a significant difference in the TS ($p < 0.05$) is observed in films with probiotics. It is also interesting to note that the

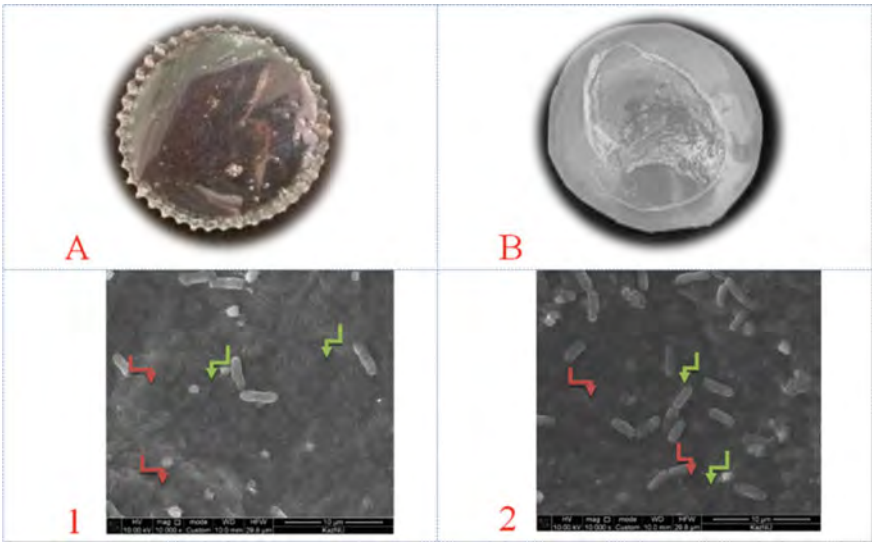

Fig. 17.2 Photograph (**a**) and SEM cross-section image (**b**) of CMC (1) and CMC/Ch (2) films loaded with probiotic *Lactobacillus*. Cells included in (cells included in film structure are shown with red arrows, green arrows show cells attached on surface of material)

Table 17.1 Physicochemical and optical properties of carboxymethyl cellulose films

Type of film	Parameters		
	TS (MPa)	EB (%)	MC (mg/g) of film
CMC	20.3 ± 1.2^a	15.6 ± 0.2^a	340.3 ± 8.2^a
CMC/Ch	28.4 ± 0.8^b	12.3 ± 0.1^b	228.4 ± 7.9^b
CMC/probiotic	15.4 ± 0.2^b	19.4 ± 0.3^b	360.3 ± 10.2^a
CMC/Ch/probiotic	23.7 ± 1.4^b	18.2 ± 0.08^b	237.8 ± 9.4^b

Results are represented as mean ± standard deviation. Values with different superscript letters in each column are significantly different ($p < 0.05$)
a, *b* show statistical difference of values

tensile strength and elongation to break follow an opposite trend. Inclusion of Ch in CMC film improves the TS but decreases the EB. In the present study, addition of probiotic cells into CMC and CMC/Ch films significantly reduced TS as well as EB. This indicates a lower strength and flexibility of the obtained probiotic films. Probably this phenomenon is a consequence of the increase in molecular mobility and free volume in polymer chains in films during immobilization of bacteria in them. Overall, the mechanical properties obtained films are promising.

The moisture content (MC) after drying not only affects the rate of viability decrease during long storage periods but it facilitates melting of edible films in the mouth. Therefore, the quantitative determination of MC in films is important. The MC of the films is shown in Table 17.1.

The CMC film presents the highest swellability. The drawback of such a huge water uptake is that the highly swollen film behaves as a weak gel and thus its handling is rather difficult in contrast to other formulations.

It was observed that the CMC/Ch films present a rather similar trend with a low swelling capacity. In the present study, the addition of probiotics caused no significant effect on the film moisture ($p > 0.05$). Similar results were found in previous studies [13].

Regardless of the technological mechanism for the production of edible films containing probiotics, it is of primary importance that the film has the ability to provide of the viability of probiotic strains in films in order to assess their suitability as probiotic carriers.

One of the most important effective factors on the viability of probiotics is temperature of distribution and storage conditions [5]. The optimal storage temperature, ensuring safety of the population level of probiotics in the composition of functional foods as well as edible films is 4–6 °C. This is explained by the fact that in such a temperature range the level of bacterial metabolism significantly decreases ensuring high cell viability [11–13]. In this regard, the survival of probiotics in the experimental films was determined under such temperature conditions. Figure 17.3 shows the survival of probiotic strains in CMC and CMC/Ch films during storage at 4 °C.

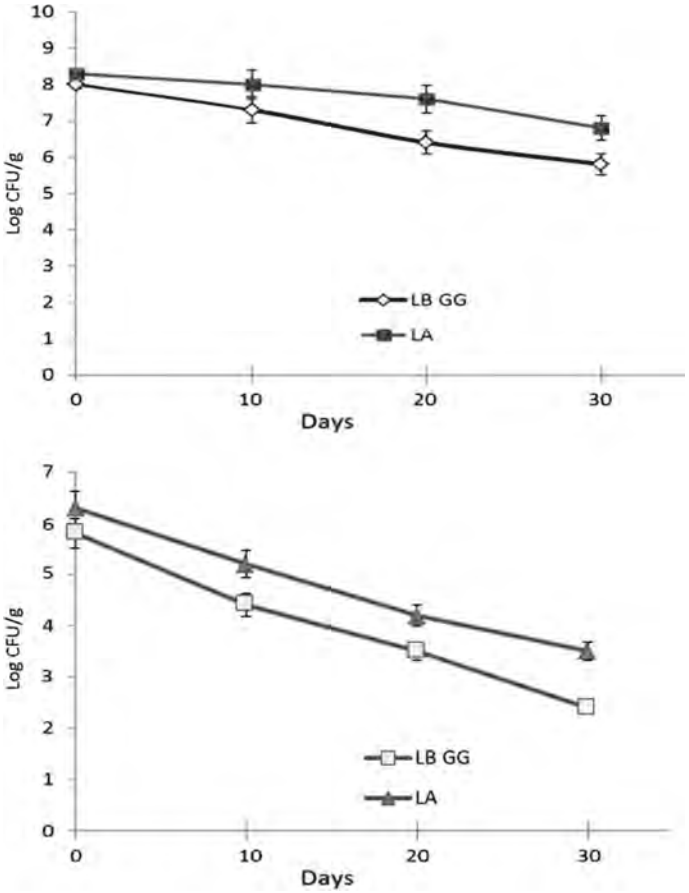

Fig. 17.3 Survivability of *L. rhamnosus* GG and *L. acidophilus* AA-1 during storage at refrigerated (4 °C) temperature. The error bars represent the standard deviation

It has been established that the bacteria trapped in the CMC film have a rather high viability around 8 Log CFU/g. The probiotics showed <2 log CFU decrease in viability at the end of storage. Such indicators are considered as good [11, 13, 22]. In general, viable LGG and LA bacteria can be effectively entrapped in the CMC based films.

In addition, MC in CMC/Ch is reduced compared to CMC films, and decrease in water activity (increase in osmotic stress) in media can affect the viability of probiotics. Furthermore, poor swelling of the film can impede the release of bacteria from it, leading to lower viability counts (thus resulting in a lower viability counting). It should also be noted that viability of LA was significantly higher than that of LGG probiotics at the end of storage. This may occur due to its higher tolerance to detrimental conditions of edible films during storage, what has been observed in other studies [13, 23, 24].

On the other hand, there are quite positive examples of quite tolerant "relationships" of probiotic cells with Ch. But this is only observed when probiotics are found in microcapsules with Ch. And in these capsules, Ch is used as an additional coating (layer-by-layer), but the basis of the microcapsule is either CMC [19] or alginate [16–18]. Therefore, cells of probiotics are in contact only with these polymers.

In general, viable LGG and LA bacteria can be effectively entrapped in the CMC based films and their release is strongly dependent on the film composition, physicochemical and biological properties of films.

17.4 Conclusion

The film properties can be controlled by physical and chemical features of components included in it. Incorporation of Ch в CMC film leads to a decrease in swelling ratio but increased rigidity of the films. Viable LGG and LA could be effectively entrapped in the films after soaking them in a bacteria medium. Presence of Ch in such films inhibits bacteria entrapped in them. However, these films may inspire the formation of related systems, such as micro-beads as carriers for probiotic bacteria and delivery in the gastrointestinal tract.

The systems developed represent promising advances in the search for new applications of edible cellulose based films and coatings as carriers of diverse probiotics and open new possibilities for the development of novel food probiotic products.

References

1. D.Z. Suput, V.L. Lazi´c, S.Z. Popovi´c and N.M. Hromis, Food Feed Res. **42**, 11–22 (2015)
2. J. Wyrwa, A. Barska, Eur. Food Res. Technol. **243**, 1681–1692 (2017)
3. P. Muranyi, J. Food Process Technol. **4**, 1–14 (2013)
4. A.E. Kapetanakou, P.N. Skandamis, Curr. Opin. Food Sci. **12**, 1–12 (2016)
5. P.J.P. Espitia, R.A. Batista, H.M. Azeredo, C.G. Otoni, Food Res. Int. **90**, 42–52 (2016)
6. F. Pavli, C. Tassou, G-J.E. Nychas, N. Chorianopoulos, Int. J. Mol. Sci. **19**, 150 (2018)
7. D.Z. Suput, V.L. Lazic, S.Z. Popovic, N.M. Hromis, Food Feed Res. **42**, 11–22 (2015)
8. A. Dhanapal, P. Sasikala, L. Rajamani, V. Kavitha, G. Yazhini, M. Shakila Banu, Food Sci. Qual. Manag. **3**, 9–17 (2012)
9. L. Sánchez-González, J. Iván Quintero Saavedra, A. Chiralt, Food Control **35**, 200–206 (2014)
10. N. Romano, M. José Tavera-Quiroz, N. Bertola, P. Mobili, A. Pinotti, A. Gómez-Zavaglia, Food Res. Int. **64**, 560–566 (2014)
11. P. Singh, S. Magalhaes, L. Alves, F. Antunes, M. Miguel, B. Lindman et al., Food Hydrocolloid **88**, 68–74 (2019)
12. J. Odila Pereira, J. Soares, S. Sousa, A.R. Madureira, A. Gomez, M. Pintado, LWT-Food Sci. Technol. **73**, 543–550 (2016)
13. B. Ebrahimi, R. Mohammadi, M. Rouhi, A.M. Mortazavian, S. Shojaee-Aliabadi et al., LWT—Food Sci. Technol. **87**, 54–60 (2018)

14. F. Garavand, M. Rouhi, S.H. Razavi, I. Cacciotti, R. Mohammadi, Int. J. Biol. Macromol. **104**, 687–707 (2017)
15. P. Varela, S.M. Fiszman, Food Hydrocolloid **25**, 1801–1812 (2011)
16. I. Trabelsi, W. Bejar, D. Ayadi, H. Chouayekh, R. Kammoun, S. Bejar et al., Int. J. Biol. Macromol. **61**, 36–42 (2013)
17. T.W. Yeung, E.F. Üçok, A.K. Tiani, D.J. McClements, D.A. Sela, Front Microbiol **7**, 494 (2016)
18. M. De Araújo Etchepare, G.C. Raddatz, E.M. de Moraes Flores, L.Q. Zepka, E. Jacob Lopes, J.S. Barin et al., LWT-Food Sci. Technol. **65**, 511–517 (2016)
19. P. Singh, B. Medronho, L. Alves, M. Miguel, B. Lindman, B. Medronho, Carbohyd. Polym. **175**, 87–95 (2017)
20. D. Raafat, H.-G. Sahl, Microb. Biotechnol. **2**, 186–201 (2009)
21. A.P. Martínez-Camacho, M.O. Cortez-Rocha, J.M. Ezquerra-Brauer, A.Z. Graciano-Verdugo, F. Rodríguez-Félix, M.M. Castillo-Ortega et al., Carbohyd. Polym. **82**, 305–315 (2010)
22. C. Soukoulis, L. Yonekura, H.-H. Gan, S. Behboudi-Jobbehdar, C. Parmenter, I. Fisk, Food Hydrocolloid **39**, 231–242 (2014)
23. K. Shukla, K. Mishra, A. Arotiba, B. Mamba, Int. J. Biol. Macromol. **59**, 46–58 (2013)
24. M. Rouhi, R. Mohammadi, A. Mortazavian, Z. Sarlak, Dairy Sci. Technol. **95**(2), 115–133 (2015)

Chapter 18
Synthesis of Silver Nanoparticles and Therapeutic Films for Ophthalmology Based on Them

V. Skobeeva, V. Smyntyna, V. Ulyanov, M. Makarova, V. Tkachenko, N. Malushin, and N. Molchaniuk

Abstract This article presents the results of the silver nanoparticles synthesis by a simple and ecological method of chemical reduction of silver from silver nitrate in an aqueous solution of sodium citrate and their use in the treatment of eye diseases. The technological conditions that lead to formation of silver nanoparticles with spherical shape and size of 30 nm with an intensive band of surface plasmon resonance are established. The effect of the application of therapeutic films with nanoparticles on the ultrastructure of the epithelium and stroma of the cornea of a rabbit after modeling in animals of moderately severe bacterial keratitis has been studied. It has been established that the application of therapeutic films with silver nanoparticles, as compared with antibiotics, leads to more efficient regeneration of the anterior corneal epithelium, contributes to the rapid restoration of the stroma and active formation of the delicate collagen skeleton typical of healthy corneal tissue.

18.1 Introduction

Interest in studies of Ag nanoparticles (Ag NPs) is due to a number of their unique properties that differ from the properties of nanoparticles of other metals, namely, Ag NPs have the greatest intensity of the surface plasmon resonance band (SPR), high absorption coefficient, the phenomenon of giant Raman scattering. The development of nanotechnology and modern research on the potential biological

V. Skobeeva (✉) · V. Tkachenko · N. Malushin
Research Institute of Physics, Odessa I.I. Mechnikov National University Odessa, Odessa, Ukraine
e-mail: v_skobeeva@ukr.net

V. Skobeeva · V. Smyntyna
Odessa I.I. Mechnikov National University, Odessa, Ukraine

V. Ulyanov
Odessa National Medical University, Odessa, Ukraine

M. Makarova · N. Molchaniuk
The Filatov Institute of Eye Diseases and Tissue Therapy, National Academy of Medical Sciences of Ukraine Odessa, Odessa, Ukraine

A. D. Pogrebnjak et al. (eds.), *Nanomaterials in Biomedical Application and Biosensors (NAP-2019)*, Springer Proceedings in Physics 244,
https://doi.org/10.1007/978-981-15-3996-1_18

properties of silver nanoparticles confirm their applicability in medicine. Due to their high antibacterial activity, anti-inflammatory action, low toxicity, silver ions and nanoparticles are used as an alternative to antibiotics. Silver NPs have been used as wound dressings for the treatment of burns, in the form of coatings for medical devices impregnated with silver nanoparticles [1, 2], in the development of restoration materials for dentistry [3]. In a review article [4] R.P. Allaker reports on the use of nanoparticles in combating infections of the oral cavity, on the use of nanoparticles in photodynamic therapy. Studies by the authors [5] showed that Ag NPs show the best antimicrobial activity compared to the standard antibiotic chloramphenicol. This confirms the possibility of using Ag NPs as an antimicrobial agent for suppressing gram-negative and gram-positive bacteria. Ag NPs are non-toxic to humans and do not create side effects compared to antibiotics. Compared with conventional antibiotics, the development of bacterial resistance is less likely when using nanostructured media. Such nanomaterials can attack a wide range of targets in bacteria, for example, membrane proteins, the lipid bilayer, and damage DNA when nanoparticles are absorbed [6]. An analysis of the literature data showed that, despite numerous examples of the use of Ag NPs in medical practice, there is practically no information on the use of Ag NPs in ophthalmology.

In addition, for the practical implementation of the unique properties of Ag NPs, the issue of using nanoparticles with stable and controlled physical and optical characteristics (size, shape, spectrum, and absorption intensity under local plasmon resonance conditions) is topical. This task is closely related to the study of the influence of synthesis conditions on the formation of Ag NPs with the properties that are required for a specific medical application. Note that with the development of modern technologies for producing Ag NPs with the prospect of their further practical application, simple, low-toxic and environmentally friendly synthesis methods are relevant.

In this work, on the basis of these considerations, the method of chemical reduction of silver salt in an aqueous solution of sodium citrate, in which sodium citrate ($Na_3C_6H_5O_7$) performs the functions of both a reducing agent and a particle stabilizer. Sodium citrate is the sodium salt of citric acid, which has a synthetic origin and a very low level of danger. Sodium citrate is often used as a drug. Anionic surfactant, sodium dodecyl sulfate (SDS), which also has a low level of toxicity, was used as additional stabilizers. The above information justifies the use of these substances as media in which silver NPs are formed. However, the fact that sodium citrate performs a dual role in the synthesis (silver reducing agent and NP growth stabilizer) makes the synthesis process dependent on many factors. The problem is that the processes of nucleation and growth of nanoparticles depend on the rate of chemical reaction of silver ion reduction, on the concentration of the reacting components, their ratio, the method of introducing the reagents into the solution.

Thus, the technological part of this work on the synthesis of Ag NP includes the establishment of optimal conditions that ensure the growth and stability of NP of different sizes.

The purpose of the second part of the work is to study the effect of applications of therapeutic films with silver nanoparticles of 30 nm in size, obtained by the citrate

method, on the ultrastructure of the epithelium and stroma of the rabbit cornea after modeling in animals of moderate bacterial keratitis.

18.2 Material and Research Methods

The object of the study of the effect of Ag NPs on ophthalmic diseases was rabbits, in which moderately severe bacterial keratitis was modeled.

Bacterial keratitis in rabbits was modeled according to the patent scheme [7].

After receiving a model of keratitis of moderate severity, all animals were equally divided into 3 groups:

1. control group—rabbits with moderate keratitis
2. group—rabbits with application of a film with silver nanoparticles on the cornea.
3. group—rabbits with antibiotic application (decamethoxin) on the cornea.

Films were obtained by casting onto a polished surface using polyacrylamide, polyvinyl alcohol, polyvinylpyrrolidone, and sodium carboxymethylcellulose as the base. The concentration of Ag NPs in the film was 10 mg/g.

Electron microscopic studies of the ultrastructure of the rabbit cornea were carried out on an electron microscope TEM-100-01. The studied material was processed according to the described generally accepted method [8]. Ultra-thin sections were contrasted by the Reynolds method [9]. Electron microscopic studies of Ag NPs were carried out using scanning electron microscopy (SEM), atomic force microscopy (AFM). To control the synthesis of Ag NPs, we used the method of optical spectrometry in the UV and visible spectral regions.

18.3 Results and Discussion

18.3.1 Synthesis and Optical Properties of Ag NPs

Silver nanoparticles were synthesized by the method of chemical reduction of silver ions from a solution of silver salt ($AgNO_3$) by a reducing agent—sodium citrate ($Na_3C_6H_5O_7$). The reaction used solutions of silver nitrate and sodium citrate with an equimolar concentration of 1×10^{-5} M; 1×10^{-4} M; 1×10^{-3} M; 5×10^{-3} M. The synthesis reaction temperature is 100 °C. The synthesis time varied depending on the conditions of registration of the local surface resonance band (SPR) of Ag NPs (10; 15; 20; 30; 40; 50; 60; 70; 80 min).

The experimental results showed that the process of synthesizing NPs significantly depends on the concentration of the initial reaction products. It was noted that at concentrations of silver salt 10^{-5} M at 100 °C for 120 min, the SPR band in Ag NPs is not registered. It was established that with a further increase in the concentration

of $AgNO_3$, (1×10^{-4} M to 5×10^{-3} M), the formation of silver NPs is determined by the kinetics of the chemical reaction.

The kinetics of the formation of Ag NPs in the reduction reaction was studied using spectrometry in the UV and visible spectral regions at different initial concentrations of $AgNO_3$ and $Na_3C_6H_5O_7$. The basis for the application of the optical method is the fact that the intensity, shape and half width of the SPR band of Ag NPs depend on the number of nanoparticles in the solution and their size dispersion, and the position of the SPR band maximum depends on the size of the NP. The appearance of this band in the absorption spectra is evidence of the formation of silver metal nanoparticles, in which surface plasmons are formed when interacting with electromagnetic irradiation.

In the absorption spectrum of the obtained silver nanoparticles, an intense SPR band is recorded, the maximum of which is localized in the wavelength range of 415 ± 420 nm. This position of the band maximum SPR corresponds to the average NP size of 30 nm. The maximum intensity of the absorption band was achieved at component concentrations in the range of 1×10^{-3} M to 5×10^{-3} M (curves 2 and 3, Fig. 18.1).

It is characteristic that the position of the band maximum does not depend on the concentrations of the components in the range (1×10^{-4} M to 5×10^{-3} M), which indicates the formation of nanoparticles of the same size (30 nm) at the end of the synthesis process. The dependence of the absorption spectra of Ag NPs on the synthesis time for a concentration of 5×10^{-3} M is shown in Fig. 18.2. An increase in the intensity and a decrease in the half-width of the SPR band with increasing synthesis time (1, 20 eV, 1.12 eV, 1.07 eV for curves 2, 3, 4, respectively) is observed. The increase in the absorption intensity and the narrowing of the LPRS

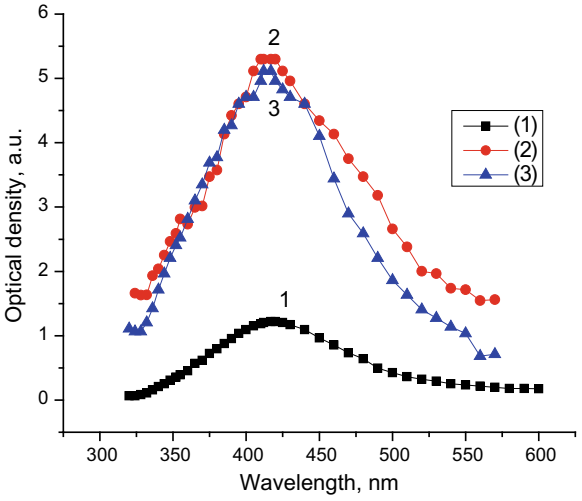

Fig. 18.1 The absorption spectra of Ag NPs obtained at different concentrations of $AgNO_3$ and $Na_3C_6H_5O_7$: 1×10^{-4} M (1), 1×10^{-3} M (2), 5×10^{-3} M (3)

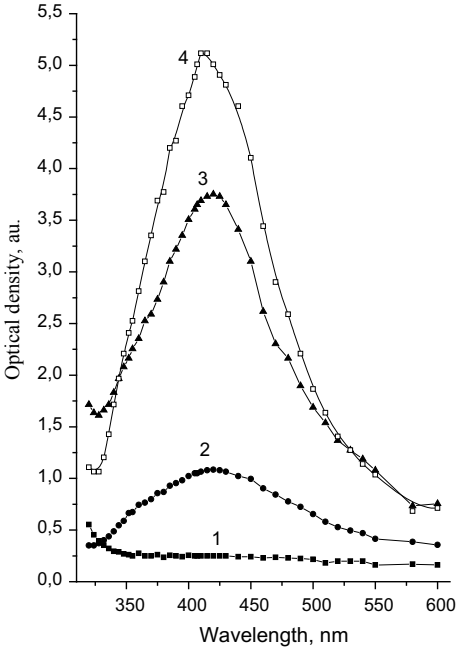

Fig. 18.2 Dependence of the absorption spectra of silver NPs on the synthesis time, min: 10 (1); 13 (2); 15 (3); 20 (4). The concentrations of $AgNO_3$ and $Na_3C_6H_5O_7 = 5 \times 10^{-3}$ M

band may be evidence in favor of the following mechanism for the formation of Ag NPs. At the first stage, particles of different sizes are formed, then smaller particles dissolve according to the mechanism of Ostwald ripening and, at the same time, the particles grow due to the recovery of silver ions on the surface of nanoparticles.

When the concentration of the components is more than 5×10^{-3} M, as a result of coagulation of the nanoparticles, the formation of silver precipitate in solution was observed. Thus, silver NPs used for research in ophthalmology were obtained at a component concentration of 5×10^{-3} M and had a spherical shape with an average size of 30 nm (Fig. 18.3.).

The effect of applications of therapeutic films with silver nanoparticles 30nm in size on the ultrastructure of the cornea of rabbits with moderate keratitis was studied.

The ultrastructure of the cornea of the control group of rabbits with moderate keratitis is shown in Fig. 18.4.

In the central region of the cornea, there is an accumulation of blood cells and histiocytic cells, as well as single collagen fibrils between them. The cells of the anterior epithelium in the subliminal region of the cornea, including the basal ones, have signs of dystrophic changes. They contain few organelles, membrane organelles are vacuolated, the nuclei are small with loosely arranged chunks of chromatin. Some of the cells have signs of cytoplasmic edema. In the intercellular fissures between the basal cells, electron-dense deposits are visible. Moreover, most of the basal cells also

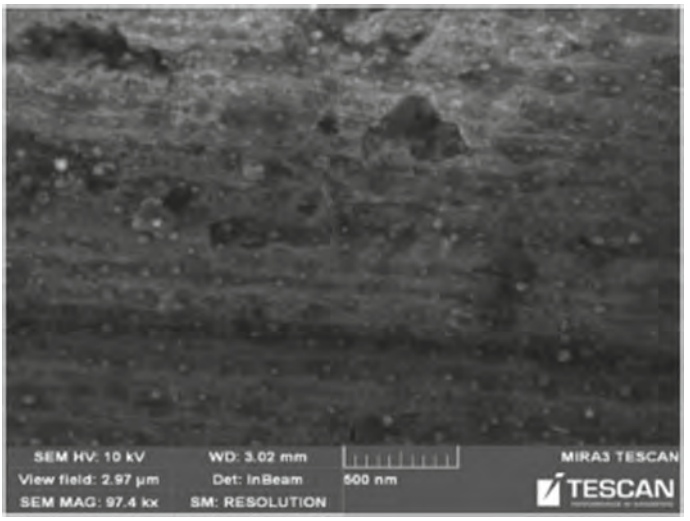

Fig. 18.3 Image of silver NPs obtained in a raster electron microscope

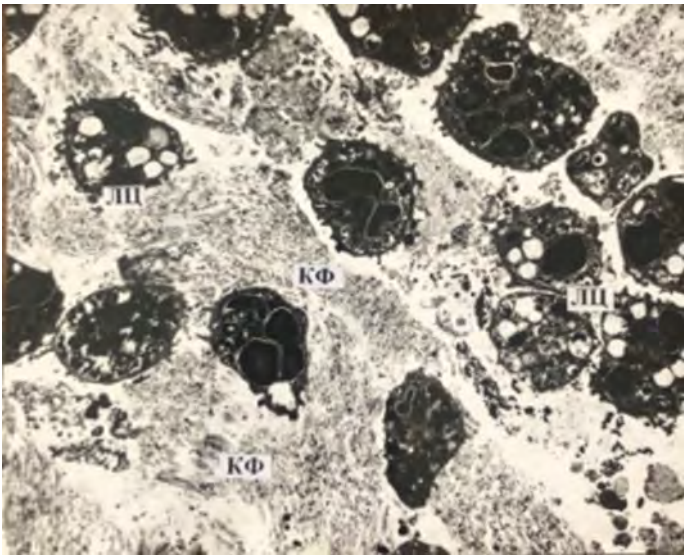

Fig. 18.4 Ultrastructure of a rabbit cornea during modeling of moderate bacterial keratitis. The accumulation of leukocytes and destroyed collagen lamellae in the stroma. Collagen fibrils in a state of destruction. Electron micrograph X 2500. Legend: ЛЦ—leukocytes, КФ—collagen fibrils

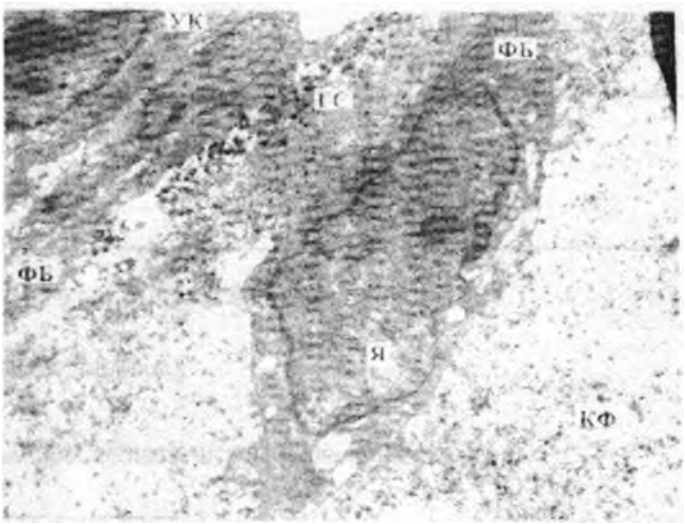

Fig. 18.5 Ultrastructure of the cornea in the area of reparative regeneration of ACE at the border with the performed stromectomy and with the subsequent application of the film with silver nanoparticles. A flattened cell in contact with fibroblast. Large fibroblast and accumulations of silver granules in the connecting skeleton. Electron micrograph X 6000. Legend: УК—a flattened cell, ГС—silver granules, КФ—collagen fibrils, FB—fibroblast, Я—nucleus

contain a homogenized electron dense cytoplasm. The basement membrane does not contain semi-desmosomes.

Ultrastructure of the cornea in the area of reparative regeneration of the anterior corneal epithelium (ACE) at the border with the performed stromectomy and with the subsequent application of films with silver nanoparticles is shown in Fig. 18.5.

In the area of the formation of the epithelial layer in the basal layer, single, slightly differentiated cells are located, located in one row, having short finger-shaped outgrowths with the help of which these cells come into contact with each other, forming interdigitations. They form large intercellular clefts in the form of cavities. Dense intercellular connections are also observed here. In the cytoplasm of these cells, a large nucleus is determined in the karyoplasm of which chromatin is located in a diffuse state, in the center of the karyoplasm there are a large number of free ribosomes and polysomes, and small cisterns of the granular endoplasmic reticulum (ЗЭС). In some places, cells of the same type are in contact with single, large, flattened cells with a fusiform nucleus containing chromatin in a diffuse state, and its margin is also determined. The cytoplasm of these cells contains polysomes, a few mitochondria, with focal destruction of cristae, vacuoles, apparently formed from mitochondria after the destruction of the inner membrane. Under the aforementioned cells are clusters of silver granules and fibroblasts in contact with these cells. Deeper, in the connective tissue skeleton, consisting of thin, short fibrils, silver granules and large fibroblasts with a well-defined ЗЭС are also diffusely located, in the cavity of

the cisterns of which there is a moderate electron density, which indicates protein synthesizing activity.

18.3.2 Ultrastructure of the Cornea in the Area of Reparative Regeneration of ACE at the Border with the Performed Stromectomy and with the Subsequent Application of the Film with Decamethoxin

The anterior corneal epithelium in direct contact with the area where the stromectomy was performed consists of a well-formed layer of surface cells, under which there are large, poorly differentiated basal cells of a round or oval shape, a nucleus containing chromatin in a diffuse state and electron-transparent karyoplasma. Their cytoplasmic backbone consists of short thin fibrils, tonofilaments, rod-shaped or round mitochondria. The number of mitochondria in the cells is not the same, from single organelles in a number of cells to their accumulations in others. A small number of short ЗЭС cisterns containing ribosomes on the profiles of their membranes and slightly free ribosomes are also determined in these cells. The intercellular contacts in the forming layer are dense, sometimes narrow gaps are visible. Interdigitations are determined in places. The basement membrane is not formed. In some areas under the layer of basal cells, elements of the formation of the basement membrane are observed. Under the basal cells in the electron-transparent zone are located short, thin, lying diffusely or in the form of small clusters, collagen fibrils. Near this area, basal cells, both slightly and more differentiated, containing an increased number of organelles, are detected. Subepithelially located tender connective tissue skeleton. In the PER region, a layer of surface cells and a layer of basal cells are observed. The cells of the surface layer, especially those that border the cells of the basal layer, contain an increased number of polysomes, small mitochondria, and bundles of tonofilaments. Basal cells are more differentiated, a large number of typical organelles are revealed in their cytoplasm. Cells are mostly closely adjacent to each other. In places, slightly pronounced, interdigitations and gap junctions are visible. The basement membrane under these cells is more formed, single semi-desmosomes and anchor filaments are visible. Subepithelially visible elements of the coarse connective tissue (Fig. 18.6).

18.4 Conclusions

The kinetics of the formation Ag NPs in the reaction of silver reduction with sodium citrate was studied at various initial concentrations of $AgNO_3$ and $Na_3C_6H_5O_7$. Optimal conditions have been established that ensure the growth and stability of NPs with an average size of 30 nm. To control the synthesis of Ag NPs, the method of optical spectrometry in the UV and visible spectral regions was used.

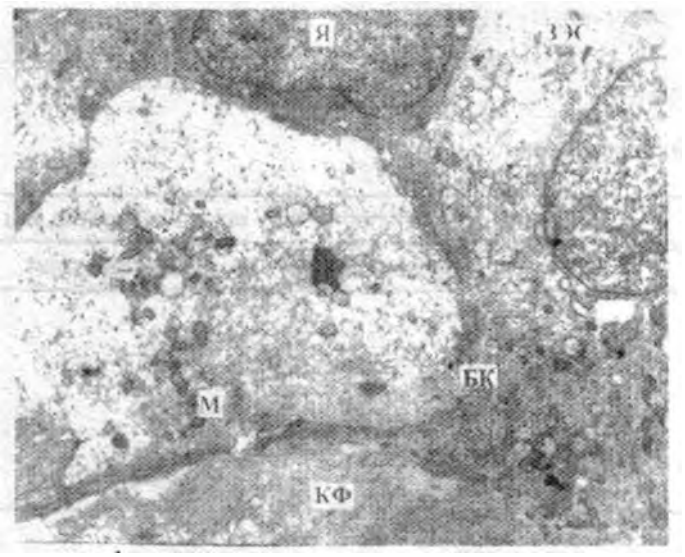

Fig. 18.6 The ultrastructure of the cornea in the area of reparative regeneration of ACE at the border with the performed stromectomy and with the subsequent application of the film with decamethoxin. Under the basal cells, which are in a state of varying degrees of differentiation, are collagen fibrils of coarse connective tissue. Electronic micrograph. X 5000. Legend: БК—basal cells, Я—the nucleus, M—mitochondria, ЭС—granular endoplasmic reticulum, КФ—collagen fibrils

It was shown that films with silver nanoparticles 30 nm in size obtained by the citrate method reduce the exudative phase of the inflammatory process, enhance the proliferative reaction, which leads to the regeneration of the anterior epithelium of the cornea, contribute to the rapid recovery of stroma, due to an increase in the number of fibroblasts, as well as an increase in their protein synthesizing function and the active formation of a delicate collagen skeleton characteristic of healthy corneal tissue.

After exposure to films with decamethoxin, the restoration of the anterior epithelium of the cornea and stroma is slowed down, signs of the exudative phase of the inflammatory process are expressed. In the stroma, the formation of coarse fibrous connective tissue occurs.

References

1. T. Gunasekaran, T. Nigusse, M.D. Dhanaraju, Silver nanoparticles as real topical bullets for wound healing. J. Am. Coll. Clin. Wound Spec. **3**, 82–96 (2012). https://doi.org/10.1016/j.jcws.2012.05.001
2. M. Rai, A. Yadav, A. Gade, Silver nanoparticles as a new generation of antimicrobials. Biotechnol. Adv. **27**(1), 76–83 (2009). https://doi.org/10.1016/j.biotechadv.2008.09.002
3. E. Abou Neel, L. Bozec, R. Perez, H. Kim, J.C. Knowles, Silver nanoparticles as a new generation of antimicrobials. Int. J. Nanomed. **10**, 6371–6394 (2015). https://doi.org/10.2147/IJN.S86033

4. R.P. Allaker, The use of nanoparticles to control oral biofilm formation. J. Dent. Res. **89**, 1175–1186 (2010). https://doi.org/10.1177/0022034510377794
5. A. Shukla, B.A. Makwana, Facile synthesis of silver nanoparticle and their potential application. J. Nanosci. Nanotechnol. **2**, 84–92 (2014). https://doi.org/10.11648/j.nano.20140204.14
6. R. Kummala, K.J. Brobbey, J. Haapanen, J.M. Mäkelä, M. Gunell et al., Antibacterial activity of silver and titania nanoparticles on glass surfaces. Adv. Nat. Sci. Nanosci. Nanotechnol. **10**, 015012–015017 (2019)
7. Patent for model No. UA87119U dated 1/27/2014 Drozhzhina GI, Gaydamaka TB, Vansovich E.V.
8. V.A. Ulyanov, M.B. Makarova, N.I. Movchanyuk, The effect of instillation of a colloidal solution of silver nanoparticles on the ultrastructure of the anterior epithelium and cornea strom. Ophthalmol. J. **3**(476), 63–69 (2017)
9. E.S.S. Reunoldes, The use of lead citrate at higt pH an electronopaque stain in electron microscopy cornea strom. J. Cell Biol. **17**, 208–212 (1963)

Chapter 19
A Hg (II) Fluorescent Sensor Based-on Bodipy Synthesized by Using Knorr Pyrrole

Ersin Guler, Emine Bagci, and Ahmed Nuri Kursunlu

Abstract In this study, firstly Bodipy derivative containing organic groups were prepared. Changes in the emission, absorption and excitation properties of these compounds were then examined in the presence of some metal ions. Thus, in these measurements, it was determined that the final Bodipy derivative intended to be selective of metal ions were found and the compounds obtained were tested with different metal ions. However, only mercury has shown a selectivity for the metal. The prepared compound based-on Bodipy can be used as a fluorescent sensor for the Hg (II) ions.

19.1 Introduction

Due to their fluorescent properties, Bodipy compounds generally have the potential to be used as effective drugs in cell labeling of biomolecules and in photodynamic therapy. Phthalocyanines are target compounds that can be used in photodynamic therapy because of their ability to absorb high wavelength light (about 700 nm), high triplet state quantum yields, triplet state long life, no toxic effect when light is not used, and effectively producing singlet oxygen [1–3].

One of the most important properties of Bodipy dyes is the ability to change their optical properties by changing the molecular backbone. These Bodipy dyes have sharp absorption bands, high fluorescence quantum yields, good solubility, chemical and photochemical resistance in solvent or solid state and ability to transfer energy [4, 5].

They also have very good heat and photochemical stability. Physical conditions are also very stable compounds, they are not much affected by the pH and polarity of the environment. Other advantages of Bodipy dyes are simple synthesis methods, good solubility in organic solvents and a narrow emission band. The photochemical

E. Guler (✉) · E. Bagci · A. N. Kursunlu
Faculty of Science, Department of Chemistry, University of Selcuk, Konya, Turkey
e-mail: eguler66@gmail.com

A. D. Pogrebnjak et al. (eds.), *Nanomaterials in Biomedical Application and Biosensors (NAP-2019)*, Springer Proceedings in Physics 244,
https://doi.org/10.1007/978-981-15-3996-1_19

properties of Bodipys can be readily adjusted by modification, such as emission and excitation wavelengths [6–8].

Bodipy and many derivatives make absorption and emission (500–700 nm) in the visible region. Bodipy, the basic state of singlet (S_0), is thought to result from the fluorescence of S_1 (which is the case for most organic chromophores), and the population of S_1 is assumed to be a simple HOMO → LUMO electron transition [6–8].

The light-induced electron transfer causes the transition from one group to another in the Bodipy compound of the electron excited by photon energy. This transition may be from the Bodipy core to the substituent or from the substituent to the Bodipy core.

Light-induced electron transfer is responsible for fluorescence quenching. This usually occurs in natural phenomena, which is very important in artificial systems and photosynthesis for the conversion of solar energy based on beam-effective charge separation.

The purpose of this study firstly a Bodipy derivative containing Knorr pyyroles were prepared. Changes in the emission, absorption and excitation properties of these compounds were then examined in the presence of some metal ions. Thus, in these measurements, it was determined that the final Bodipy derivative intended to be selective of metal ions were found and the compounds obtained were tested with different metal ions. However, only mercury has shown a selectivity for the metal. The prepared compound based-on Bodipy can be used as a fluorescent sensor for the Hg (II) ions.

19.2 Experiment Details

All chemicals used; isophthaloyl dichloride, 2-propin-1-amine, N1, N3-di (prop-2-yn-1-yl) isophthalamide, 1,4-bis (prop-2-yn-1-yloxy) benzene, benzene-1 2-diamine, sodium azide, lithium bromide, potassium iodide, copper sulfate, sodium ascorbate, potassium carbonate. The metals used are; chromium (Cr (III)), cobalt (Co (II)), copper (Cu (II)), zinc (Zn (II)), mercury (Hg (II)), lead (Pb (II)), cadmium (Cd (II)). Column chromatography, synthesis and characterization applications, dimethylformamide, tetrahydrofuran, dichloromethane, ethanol, ethyl acetate, petroleum ether (40–60%), n-hexane, chloroform, methanol, toluene, acetone, dimethyl sulfoxide, deutero chloroform, deutero dimethylsulfoxide, deutero methanol, acetonitrile, diethylether solvents were used.

Since the pyrrole required for the reaction medium deteriorated very quickly at light and temperature, it was distilled and used fresh each time. However, dry-dichloromethane used in Bodipy syntheses was obtained with the aid of a special apparatus and calcium hydride. Elemental analysis of the C, N and H atoms in the molecule was carried out on the Bruker brand elemental analyzer. ^{1}H-NMR, ^{13}C-NMR, ^{11}B-NMR, ^{19}F-NMR spectra were performed with a Varian 400 MHz spectrometer.

19.2.1 The Synthesis of Bodipy Including Alkly-Chloro (Compound 1)

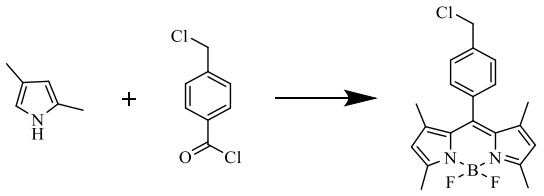

1

4-(chloromethyl) benzoyl chloride (1.5 g, 7.9 mmol) was added dropwise to a solution of 2,4-dimethyl pyrrole (1.65 mL) in dry dichloromethane (150 mL) at room temperature and under N_2. The solution was stirred in the dark for 2 h (at 60 °C). After cooling the solution, triethylamine (TEA) (10 mL) was added to the remaining solid, the mixture was stirred under N_2 for 30 min at room temperature, and then boron trifluoride diethyl etherate (7 eq) was added. The solution was stirred at 60 °C for 2 h and the resulting residue was purified by column chromatography (petroleum ether-EtOAc; 7: 1 ratio). An orange solid.

FT-IR values: 1640 cm^{-1} (C=N), 1600–1450 cm^{-1} (C=C), 3000–2880 cm^{-1} (C–H), (1.75 g, Yield 41%). M.P.:189 °C. ^{1}H NMR [400 MHz, $CDCl_3$]: 7.48 (d, 2H, ArH), 7.25 (d, 2H, ArH), 6.02 (s, 2H, Pyrrole-H) 5.18 (s, 2H, CH_2), 2.53 (s, 6H CH_3) 1.25 (s, 6H, CH_3).

19.2.2 The Synthesis of 8-(azidomethyl)-4,4-difluoro-1,3,5,7-tetramethyl-4-bora-3a, 4a-diaza-s-indacene (Compound 2)

A mixture of compound 1 (2.3 g, 6.2 mmol), NaN_3 (1.2 g, 18.6 mmol) and LiBr (0.54 g, 6.2 mmol) in DMF (30 mL) was stirred at room temperature for 24 h using a magnetic stirrer. H_2O (15 mL) was then added. The aqueous layer was extracted with ethylacetate. The combined organic layers were washed with water, dried with $MgSO_4$, filtered and concentrated. Column chromatography afforded a red solid, i.e., Compound 2.

FT-IR values: 1642 cm^{-1} (C=N), 1600–1450 cm^{-1} (C=C), 3000–2870 cm^{-1} (C–H), 3400 cm^{-1} (NH), M.P.: 140 °C. ^{1}H-NMR [400 MHz, $CDCl_3$]: 7.51 (d, 2H, ArH), 7.32 (d, 2H, ArH), 5.99 (s, 2H, Pyrrole-H), 4.49 (s, 2H, CH_2), 2.52 (s) 6H, CH_3), 1.27 (s, 6H, CH_3).

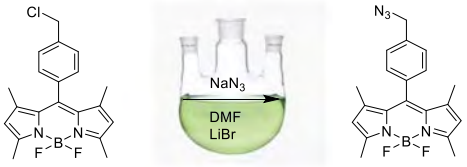

1 2

19.2.3 *Synthesis of N^1, N^3-di (Prop-2-yn-1-yl) Isophthalamide (Compound 3)*

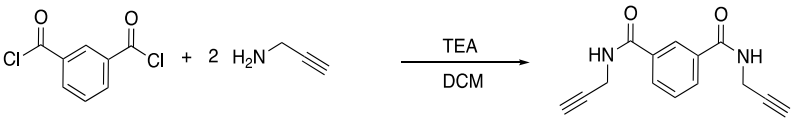

To a solution of isophthaloyl dichloride (167.0 mg, 1 mmol) in dichloromethane was added 0.5 mL of triethylamine at −5 °C (salt-ice). 0.4 mL of propargylamine was then added dropwise to this solution at room temperature and stirred for 48 h. The mixture was extracted in a DCM-water mixture and the crude product was extracted into the organic phase. The organic phase was dried with $MgSO_4$ and the solvent was evaporated in vacuo. The crude product was purified on the column (Petroleum ether 40–60%/EtOAc;1:1). A white solid was obtained.

FT-IR values: 2800–3000 cm^{-1} (CH), 1640 cm^{-1} (C=N), 1596–1448 cm^{-1} (C=C), 1682 cm^{-1} (C=O), 3370–2900 cm^{-1} (NH) Yield: 81%. ^{1}H-NMR [400 MHz, DMSO]: 9.07 (2H, t, J = 5.51 Hz), 8.34 (1H, t, J = 1.61 Hz), 8.02–7.95 (2H, m), 7.56 (1H, t, J). = 7.75 Hz), 4.10–4.08 (4H, m), 3.15 (2H, t, J = 2.49 Hz); ^{13}C-NMR [100 MHz, DMSO]: d (ppm); 165.6, 133.8, 129.9, 128.3, 126.1, 80.9, 72.6, 28.

19.2.4 The Synthesis of Bodipy

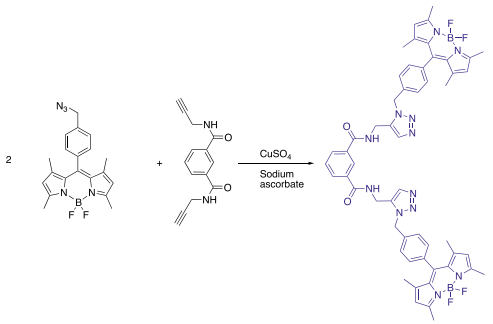

In a mixture of ethanol and water (45:5), compound 2 (0.171 g, 0.45 mmol), N^1, N^3-di (prop-2-yn-1-yl) isophthalamide (0.054 g, 0.22 mmol), $CuSO_4$ (0.034 g) (0.21 mmol) and sodium ascorbate (0.15 g, 0.76 mmol) were stirred for 3 nights with the aid of a magnetic stirrer. Purified by column chromatography (petroleum ether-EtOAc; 7:1 ratio) to give a viscous solid.

0.444 g, Yield: 40%. ^{1}H NMR [400 MHz, $CDCl_3$]: 8.25 (NH, s, 2H), 8.22 (s, 2H, ArH), 8.01 (d, 4H, ArH), 7.55 (d, 4H, ArH), 7.35 (m, 4H, ArH), 5.90 (s, 4H, Pyrrole-H), 5.19 (s, 4H, CH_2), 3.90 (s, 4H, CH_2) 2.35 (s, 12H, CH_3), 1.20 (s, 12H, CH_3). ^{13}C NMR [100 MHz, $CDCl_3$]: δ (ppm); 195.20, 161.02, 151.32, 144.22, 142.44, 141.38, 139.18, 137.22, 136.53, 135.33, 135.11, 132.31, 130.22, 129.41, 128.03, 125.21, 124.47, 123.21, 120.80, 112.44, 110.35, 59.24, 43.22, 13.44, 12.33, 10:43.

19.3 Results and Discussion

In the present study, a Bodipy based ligand was obtained as the final product. In the second stage of this study, The solutions of the Bodipy derivative and metal salts [Hg (II), Pb (II), Cd (II), Co (II), Cr (III), Cu (II), Zn (II),)] were prepared at concentrations. With these solutions, solution mixtures were prepared with a ligand/metal ratio of 1/20 and spectroscopic applications (absorption, emission and excitation, etc.) were initiated. In addition, changes in spectroscopic data, complex stoichiometry (by Job method) and determination of quenching constants due to increase in metal concentration were investigated.

As a result of this data, it was determined which metal ion is more selective for the Bodipy derivative and the degree to which it can be used as a chemosensor due to spectroscopic changes.

In the absorption study for Bodipy, ligand solution at a concentration of 1.10^{-6} M and metal salt solutions at a concentration of 1.10^{-5} M were prepared. These two solutions were mixed in a 1:1 ratio and spectroscopic applications such as absorption

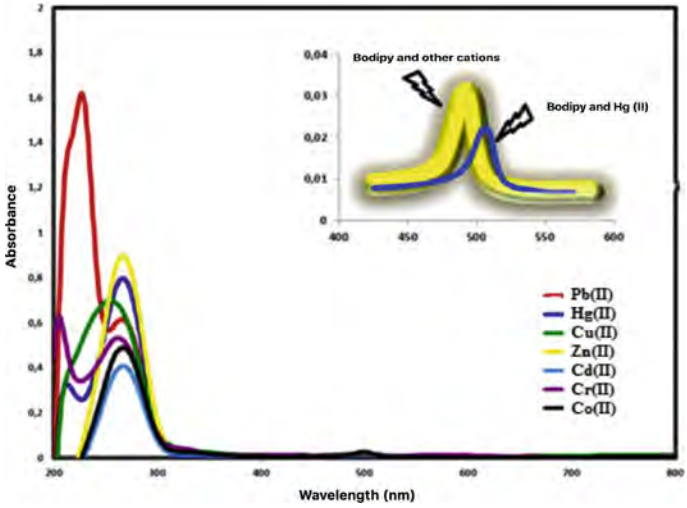

Fig. 19.1 Absorption spectra of Bodipy in presence of Pb (II), Hg (II), Cu (II), Zn (II), Cd (II), Cr (II) and Co (II)

and emission were performed. Metal salts identified as metal ion sources were used here [Cu (II), Zn (II), Hg (II), Cr (III), Co (II), Pb (II), Cd (II)]. After the addition of metal salts, other metal ions except mercury (II) ions did not cause a significant change in the absorption spectrum of Bodipy. However, a charge transfer from the Bodipy nucleus to the mercury was observed and revealed the Hg (II) sensitivity of Bodipy (Fig. 19.1).

Emission measurements were carried out to support absorption measurements. The prepared metal ion-Bodipy solutions were excited at 470 nm excitation to obtain fluorescence spectra. The emission band of Bodipy appeared around 545 nm. The emission spectra of the prepared metal ion-Bodipy solution mixtures were taken. The emission band around 545 nm showed no significant effect while other metal ions showed a significant quenching effect due to Hg (II) ions. Emission band strength decreased from 450 units to 30 units. The damping of the emission of Bodipy with Hg (II) ion sensitivity can be attributed to the paramagnetic character of the mercury complexes and it is possible to talk about a PET type charge transfer event due to the chelate effect with triazole nitrogens (Fig. 19.2).

Complex stoichiometry experiments for Bodipy with proven mercury (II) sensitivity were performed with the Job method. The Hg (II) molar fraction graph corresponding to the emission intensity gave a maximum at 0.5. Thus, the metal: ligand ratio was determined to be 1:1 (Fig. 19.3).

Here, the binding constants were calculated using the Stern-Volmer equation. This equation;

$$I_0/I = 1 + K_{sv}[M]$$

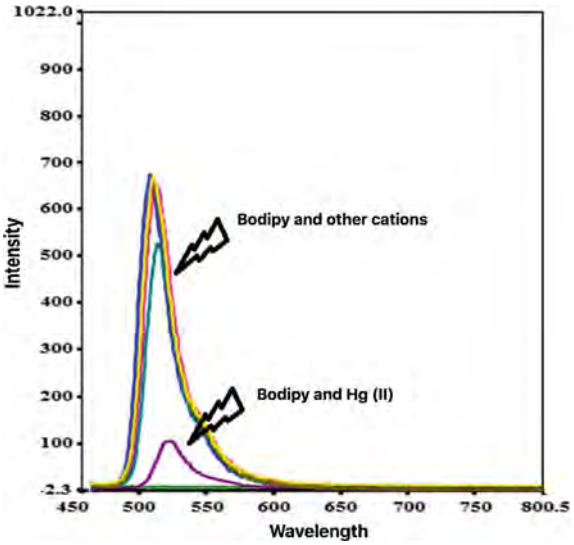

Fig. 19.2 Emission spectra of Bodipy in presence of Pb (II), Hg (II), Cu (II), Zn (II), Cd (II), Cr (II) and Co (II)

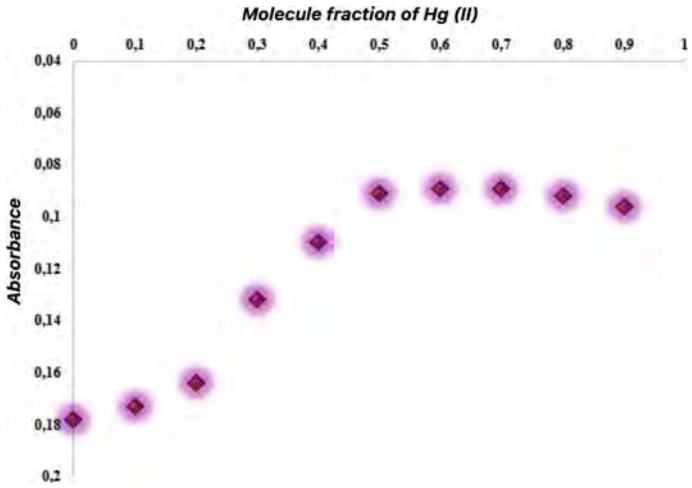

Fig. 19.3 The complex stoichiometry between Bodipy and Hg (II) ion with Job method

and I_0; In the absence of Hg (II) ion, the emission intensity of Bodipy is I; the emission intensity in the presence of Hg (II) ions, Q; Hg (II) ion concentration and K is the binding constant.

In order to understand how fast the interaction of Bodipy with Hg (II) sensitivity with mercury ion takes place, reaction time experiments were performed. For this,

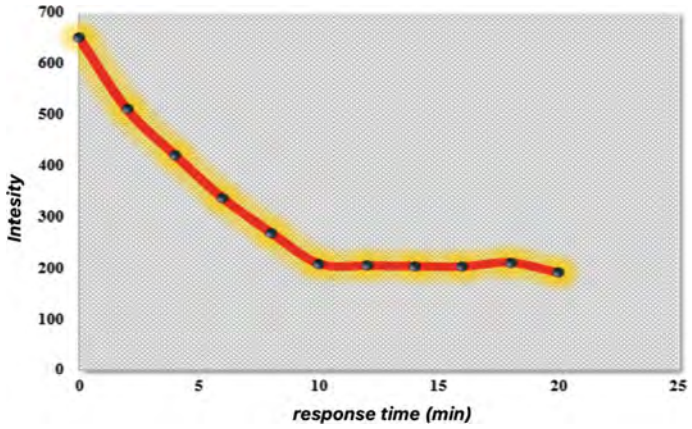

Fig. 19.4 The response time effect of Hg (II) ion on Bodipy

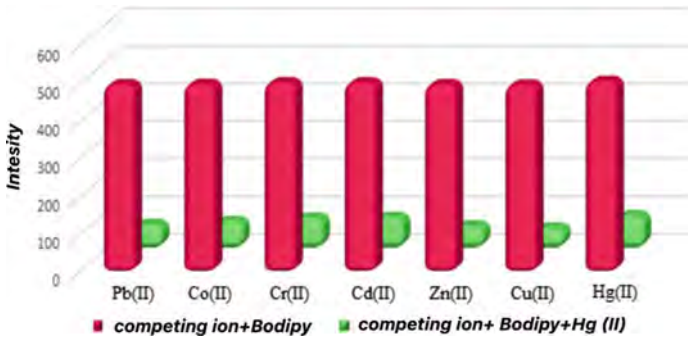

Fig. 19.5 The competing ion effect on selectivity of Bodipy for Hg (II) ion

0, 2, 4, 6, 8, 10, 12, 14, 16, 18 and 20 min were determined. The emission intensity reached a fixed value after 10 min. Thus, the most accurate time for the Hg (II) sensitivity of Bodipy 1 was found to be 10 min (Fig. 19.4).

Competing ion experiments were performed to investigate the selectivity of Bodipy against Hg (II) ions. It only affected mercury ion selectivity. In general, the other metal ions studied did not affect the Hg (II) selectivity of Bodipy. Accordingly, it has clearly demonstrated that Bodipy can be used as an Hg (II) sensor (Fig. 19.5).

19.4 Conclusions

The absorption and emission spectra of Bodipy differed only in the presence of Hg (II) ion when spectroscopic studies of Bodipy were designed to include two-way Bodipy

nucleus. So much so that the absorption bands; the emission band was markedly reduced. These data revealed the Hg (II) sensitivity of the ligand. Competitive ion tests for Hg (II) selectivity were performed for Bodipy whose sensitivity study was completed and other metal ions were studied.

Hg (II) did not affect selectivity. This result was supported by other spectroscopic experiments (complex stoichiometry, binding constant, etc.). It was concluded that Bodipy can be used as a sensitive and selective fluorescence sensor for Hg (II) ion.

Acknowledgements This research was carried out within the framework of the joint scientific project of the Selcuk University BAP (project Number: 19201054), 2019. Authors thanks to Selçuk University BAP, Prof. Dr. Zafer Yazicigil and Dr. Tugce Gover.

References

1. C. Baki N., E.U. Akkaya, J. Org. Chem. **66**, 1512–1513 (2001)
2. R. Bandichhor, C. Thivierge, N.S.P. Bhuvanesh, K. Burgess, Acta Cryst. Sect. E Struct. Reports Online **62**(10), 4310–4311 (2006)
3. M. Baruah, W. Qin, C. Flors, J. Hofkens, R.A. Valle, D. Van Beljonne et al., J. Phys Chem. A **110**(18), 5998–6009 (2006)
4. O.A. Bozdemir, F. Sozmen, O. Buyukcakir, R. Guliyev, Y. Cakmak, E.U. Akkaya, Organic. Lett. **12**(7), 1400–1403 (2010)
5. O.A. Bozdemir, O. Buyukcakir, E.U. Akkaya, Chem. A Eur. J. **15**(15), 3830–3838 (2009)
6. T. Brixner, J. Stenger, H.M. Vaswani, M. Cho, R.E. Blankenship, G.R. Fleming, Nature **434**, 625–628 (2005)
7. H. Burghart, M.B. Kim, L. Welch, H. Thoresen, J. Reibenspies et al., J. Org. Chem. **64**, 7813–7819 (1999)
8. H. Chang, O. El-Kabbani, D. Tiede, J.R. Norris, M. Schiffer, Biochemistry **30**, 5352–5360 (1991)

Chapter 20
Resistance of Hall Sensors Based on Graphene to Neutron Radiation

I. A. Bolshakova, Ya. Ya. Kost, M. I. Radishevskyi, F. M. Shurygin, O. V. Vasyliev, Z. Wang, D. Neumaier, M. Otto, M. V. Bulavin, and S. A. Kulikov

Abstract An in-situ study of Hall sensors based on single-layer graphene in neutron fluxes of a nuclear reactor up to the fluence of 1.5×20 n·m^{-2} was conducted. The sensitivity of the sensors to the magnetic field remained stable throughout the experiment, while the resistance changes correlated with the increase in sample temperature due to radiation heating. The experiment confirmed the theoretical expectations regarding the high resistance of graphene sensors to neutron irradiation. Necessary further improvement of sensor technology to optimize their characteristics, as well as irradiation testing to determine the maximum permissible neutron fluence.

20.1 Introduction

Single-layer graphene has unique electrophysical properties that allow it to be used to create high-performance electronic devices [9]. Thus, Hall sensors based on exfoliated graphene have a record high current-related magnetic field sensitivity (~5700 V·A^{-1}·T^{-1}), which is much larger than that of sensors based on traditional semiconductor materials such as Si (~100 V·A^{-1}·T^{-1}), GaAs (~1100 V·A^{-1}·T^{-1}) thin films, InAlSb/InAsSb/InAlSb nanosized heterostructures with two-dimensional electron gas (~2750 V·A^{-1}·T^{-1}) [7]. This high sensitivity is due to the small thickness of the active element of the sensor, which is the smallest possible with the use of graphene (only one layer of atoms), as well as high mobility and low density of charge carriers in graphene [18].

The great advantage of graphene compared with "bulk" materials is high resistance to the impact of corpuscular radiation, observed in experiments with charged-particle

I. A. Bolshakova (✉) · Ya. Ya. Kost · M. I. Radishevskyi · F. M. Shurygin · O. V. Vasyliev
Magnetic Sensor Laboratory, Lviv Polytechnic National University, Lviv, Ukraine
e-mail: inessa.bolshakova@gmail.com

Z. Wang · D. Neumaier · M. Otto
Advanced Microelectronic Center Aachen, AMO GmbH, Aachen, Germany

M. V. Bulavin · S. A. Kulikov
Frank Laboratory of Neutron Physics, Joint Institute for Nuclear Research, Dubna, Russia

A. D. Pogrebnjak et al. (eds.), *Nanomaterials in Biomedical Application and Biosensors (NAP-2019)*, Springer Proceedings in Physics 244,
https://doi.org/10.1007/978-981-15-3996-1_20

beams [20, 13, 14]. This feature is primarily attributed to the lack of a bulk crystal structure in graphene: this reduces the probability of collision of a bombarding particle with the sample, and in the event of such a collision makes it impossible to develop a large-scale cascade of atomic displacements, which minimizes the size of the material's damage [21]. Moreover, it has been proved that graphene is almost "transparent" to beams of light charged particles in certain ranges of their energy [16, 4], which even allows to develop on the basis of graphene the beam windows for the extraction of high-energy proton beams in powerful accelerators [22]. The second reason for the high resistance of graphene to irradiation is the effects of "self-healing" of radiation defects that are absent in "bulk" materials [20]. In graphene, they are realized, first of all, through thermally activated processes—a reordering of displaced atoms, as well as a trapping of adatoms by vacancies and nanoholes [3, 24].

Indicated features make graphene promising for the development of a new generation of irradiation-resistant Hall sensors, which, in particular, will enable to create effective systems for the plasma's magnetic diagnostics in the steady-state thermonuclear fusion reactors [19]. These facilities, in particular, include ITER, a research tokamak, which is being built in Cadarache (France), as well as DEMO, a prototype of the fusion power plant, which should give the first electric power in the middle of the 21st century. In DEMO, Hall sensors will be placed behind the blanket where the high fluxes of fast neutrons are present. It is expected that the total fluence of neutrons that sensors accumulate during the reactor lifetime will reach $F \approx 2\times10^{26}$ n·m^{-2} [1]. No device based on traditional semiconductors can operate at such high irradiation loads.

Unfortunately, today very little is known about the impact of neutron irradiation on single-layer graphene. Theoretical estimates predict the high stability of its crystal structure in the neutron fluxes, because due to the neutron's small size and absence of electric charge, the probability of its collision with the graphene atoms is only ~10^{-5} [6]. These expectations are partly confirmed by experimental studies, which, however, use an indirect analysis of the structure and consist in comparing the Raman spectra of graphene before and after irradiation. This approach has shown that irradiation with the fluence of $F \approx 1.6\times10^{21}$ n·m^{-2} forms a very small number of structural defects in graphene, which was manufactured by the Chemical Vapor Deposition (CVD) method and transferred onto the Si/SiO_2 substrates [12]. On the other hand, the authors of this work have shown in their previous studies that CVD-graphene on sapphire substrates maintains a high quality of its structure, at least up to the fluence $F \approx 4.5\times10^{19}$ n·m^{-2} [2].

The purpose of this work was an in-situ study of the functional characteristics of Hall sensors based on single-layer graphene during their irradiation with neutron fluxes in a research nuclear reactor.

20.2 Experiment Details

20.2.1 Hall Sensors Samples

Single-layer graphene, grown by the CVD method on copper foil (Graphenea, Spain), was used for manufacturing sensors. As a substrate, sapphire (Al_2O_3) with the thickness of 400 μm was used. Graphene was transferred to the substrate according to the procedure described in [15].

The sensors' active elements were made using photolithography and had a symmetrical four-lead cross-like topology (insert in Fig. 20.1), with intersection area dimensions (100 × 100) μm^2. In order to ctreate the electrical top-contacts to graphene, the layers of Ni (20 nm) and Au (400 nm) were successive deposed onto the ends of active elements arms. The active elements were protected with a layer of Al_2O_3 (80 nm) deposited by the Atomic Layer Deposition (ALD) method.

After completion of the technological procedures, the sapphire plate was diced into chips with sizes of ~(1 × 1) mm^2, each with single sensor. The chips were glued to special ceramic holders with contact pads that were connected to the sensor pads by Au-wires (Ø 30 μm) with the help of ultrasonic bonding. The holder with two samples is shown in Fig. 20.1.

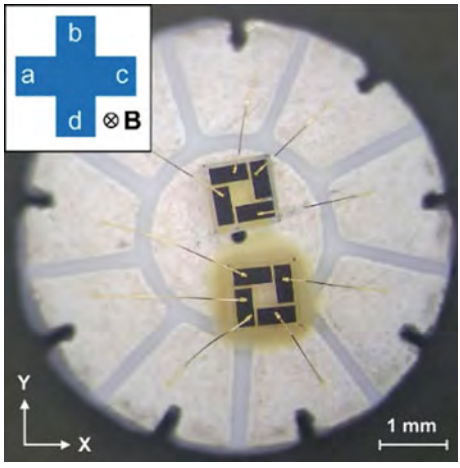

Fig. 20.1 Samples of sensors placed on a ceramic holder. Insert: schematic representation of active element

20.2.2 Sensor Characteristics Measurement Methods

The main investigated parameters in this work were sensors' current-related sensitivity S and graphene's surface resistance R_S. These characteristics were investigated during the selection of samples on laboratory equipment, as well as during the irradiation testing with the help of special control electronics.

When the Hall sensor is biased by a direct current I through one pair of opposite leads, the output signal on another pair S is defined as [17]:

$$S = \left| \frac{V_H(I, B)}{I \cdot B} \right|, \tag{20.1}$$

where I is biasing current; B is normal to the surface component of magnetic induction; $V_H(I, B)$ is Hall voltage.

The problem for S calculating is the presence at the sensor output of the residual voltage (offset) V_0, which is generated, primarily, because of inhomogeneities in the material of the active element, as well as asymmetry in its geometry and location of the leads [17]. The value V_0 does not depend on B, but depends on I and changes the sign when the current is inverted. Due to the offset existence, the output voltage of the sensor V is the sum:

$$V^{bd}(I^{ac}, B) = V_H^{bd}(I^{ac}, B) + V_0^{bd}(I^{ac}), \tag{20.2}$$

where the upper indices near I and V_H denote the leads (see Fig. 20.1) that were attached during the measurement to the positive (first index) and negative (second index) terminals of the current source and voltmeter correspondingly.

For a symmetrical sensor at $\mathbf{B} = const$ and $I = const$ a change in the connection of the arms to the current source and voltmeter in one direction ($I_{ac} \to I_{bd}$ and $V_{bd} \to V_{ca}$) does not change the offset value, but changes its sign ($V_0^{bd} = -V_0^{ca}$), while Hall's voltage preserves both its value and sign ($V_H^{bd} = V_H^{ca}$). When changing connections in different directions ($I_{ac} \to I_{bd}$ and $V_{bd} \to V_{ac}$) the situation is reversed. This is the basis of the spinning-current method, which allows to separate V_H and V_0 [17]. The method consists in sequential measurement of several values of the output voltage V, obtained for different connection's configurations, and their subsequent averaging. In this work, for the effective removal of the offset under the reactor environment, the results of four measurements were averaged:

$$V_H(I, B) = \frac{V^{bd}(I^{ac}, B) + V^{ca}\left(I^{bd}, B\right) + V^{db}(I^{ca}, B) + V^{ac}\left(I^{db}, B\right)}{4}. \tag{20.3}$$

Offset was determined by inversion of the current at $B = 0$:

$$V_0(I) = \frac{V^{bd}(I^{ac}, B = 0) - V^{bd}(I^{ca}, B = 0)}{2}. \tag{20.4}$$

For the implementation of the spinning-current method, special signal switches were used as part of the measuring equipment. It also allowed to determine the surface resistance of graphene R_S by the van der Pauw method, which involves measuring the voltage on a pair of neighboring leads while current supply is through another pair of terminals with subsequent re-switching [17]. For the selected geometry of the active element:

$$Rs = \frac{\pi}{2 \cdot \ln 2} \cdot \left[\frac{V^{bc}\left(I^{ad}, B = 0\right)}{I^{ad}} + \frac{V^{dc}\left(I^{ab}, B = 0\right)}{I^{ab}} \right]. \tag{20.5}$$

20.2.3 Temperature Testing for Samples Selection

At neutron irradiation the radiation heating of materials is taken place. In particular, preliminary estimates have shown that sensors will heat up to ~50 °C during the in-situ experiment in a nuclear reactor.

Therefore, the preliminary temperature testing of sensors in the laboratory was carried out on a special bench, built on the basis of Keithley and Tektronix high-precision measuring instruments. The bench implements spinning-current and van der Pauw methods, and also allows maintaining a constant temperature of sample T in the range up to 250 °C with accuracy ±0.5 °C.

For each sample, the test was carried out as follows: (i) characterization at $T_1 =$ 30 °C; (ii) heating at a fixed rate up to $T_2 = 54$ °C; (iii) time-exposure to achieve thermal equilibrium; (iv) re-characterization. Figure 20.2 shows the distribution of samples on the levels of relative change in their parameters after heating. The area of histogram columns is proportional to the number of samples in them.

As can be seen from Fig. 20.2, increasing of T significantly affects S, V_0 and R_S. At the same time, the changes of these values for each sample are not correlated with each other: for example, a decrease in resistance is not necessarily accompanied by an increase in sensitivity and/or a decrease in the offset. This may indicate that the temperature affects simultaneously several factors that determine the electrophysical properties.

The strongest changes are demonstrated by sensitivity, Fig. 20.2a. Among the studied sensors, there are such ones for that S reduced by almost 90% after heating, but for individual samples, on the contrary, S increased by ~5000% (on Fig. 20.2a this range is not shown for illustrative purposes). Such transformations may be due to changes in the electrostatic interaction of graphene with a substrate and a protective layer, or due to certain uncontrolled aspects of manufacturing technology (resist residuals, nonuniform adhesion, etc.). Asymmetry of histograms on Fig. 20.2b and 2c reflects the fact that after heating the values V_0 and R_S decreased for most samples. For offset, this may be due to the relaxation of mechanical stresses in graphene (although for individual samples the value of V_0 has increased by ~500%). At the

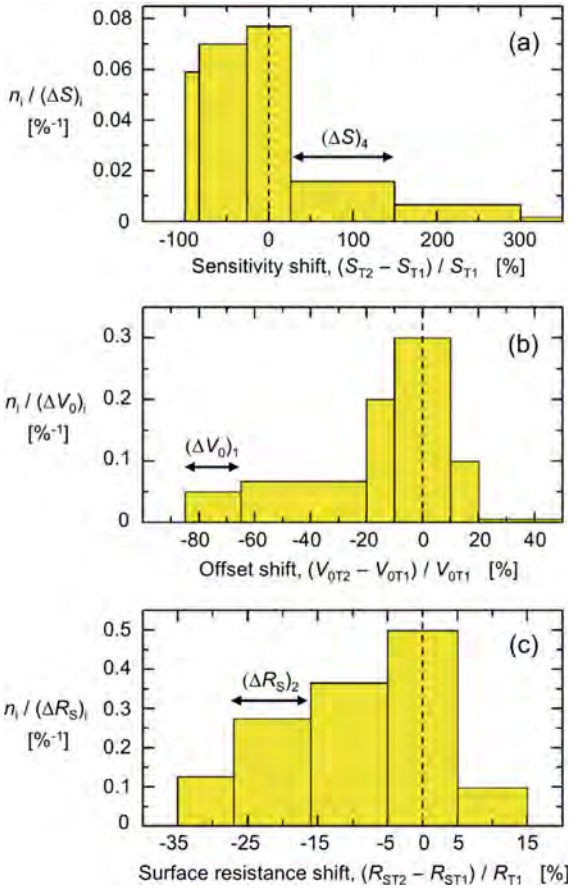

Fig. 20.2 Distribution of samples on the levels of relative change in: **a** the sensitivity S; **b** the offser V_0; **c** the surface resistance R_S during temperature change from $T_1 = 30$ °C to $T_2 = 54$ °C. n_i is the number of samples within the interval $(\Delta\ldots)_i$. Intervals $(\Delta S)_4$, $(\Delta V_0)_1$, $(\Delta R_S)_2$ shown for visualization purposes

same time, the behavior of R_S was not fully understood, as the resistance of graphene should increase from T. The possible reason for the reduction of R_S is some changes in metal/graphene contacts during heating, since the contact resistance may affect the results of measurements by the van der Pauw method [11].

In general, the change in S lies within ±25% for ~29% of the samples; change in V_0 – within ±10% for ~43% of samples; change in R_S – within ±5% for ~36% of samples.

For further investigation in neutron fluxes, it was selected the samples having a high sensitivity S and have demonstrated a satisfactory temperature stability of V_0 and R_S. The average values of their parameters were: $\langle S \rangle \approx 600$ V·A^{-1}·T^{-1}; $\langle V_0 \rangle \approx 150$ mV; $\langle R_S \rangle \approx 3000$ Ω/□.

20.2.4 In-Situ Investigations of Irradiation Stability

In-situ neutron irradiation experiment was conducted in the research nuclear reactor IBR-2 (the Joint Institute for Nuclear Research) in the irradiation channel № 3 [5]. The unique feature of IBR-2 is the pulse modulation of reactivity implemented with the help of movable reflectors, which allows to obtain in the channel № 3 a neutron flux with the high intensity of ~1.5×10^{17} n·m^{-2}·s^{-1} (on the surface of the moderator). Moreover, the IBR-2 is a fast-neutron reactor that provides large content (~38%) of fast particles (energy $E \geq 0.1$ MeV) in the neutron flux. These parameters are close to the operating conditions of Hall sensors in DEMO.

The general scheme of the experiment is shown in Fig. 20.3. For the placement of the investigated samples in the neutron flux, it was developed the special fixture based on the irradiation- and thermal-resistant ceramics Macor (Corning, USA). Each fixture contained a platinum resistance thermometer to monitor the samples temperature, as well as a copper solenoid, insert (a) in Fig. 20.3, to create a magnetic field **B**, normal to the Hall sensors surface. Holders with samples, Fig. 20.1, were fixed inside the fixture, which, in turn, was protected by a duralumin housing. Fixtures were installed on an T-beam of the irradiation facility, Fig. 20.3 insert (b), at a distance of 1.2 m from the moderator surface.

For conducting in-situ measurements, it was developed a control electronics that was located outside the irradiation channel at a distance of ~15 m from the samples. To connect samples with electronics, it was used the home-made irradiation-resistant cables like a twisted pair. To manage the electronics operation, data acquisition and processing, it was used PC with special software. The results of the measurements were stored on the remote server.

When conducting an in-situ experiment, the current supply of the sensors was $I = 100$ μA, and magnetic field was $B = 7$ mT. Neutron flux in the samples location

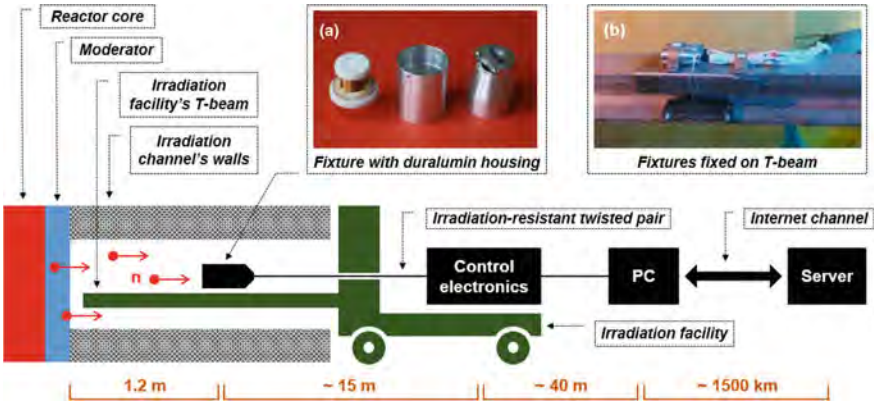

Fig. 20.3 General scheme of the in-situ experiment in the IBR-2 reactor (irradiation channel № 3, side view). Inserts: **a** photo of assembled fixture with protective housing; **b** photo of fixtures with communication lines, placed on a T-beam of the irradiation facility

was ~8.7×10^{14} n·m^{-2}·s^{-1}, which corresponds to the irradiation load level on Hall sensors expected in ITER.

20.3 Results and Discussion

Graphene sensors were irradiated for ~48 h and accumulated fluence $F \approx 1.5\times 10^{20}$ n·m^{-2}. Upon completion of the experiment, 75% of the irradiated samples kept their operability, while the rest stopped conducting the current, and this happened at different values of F. The possible cause of such behavior is the features of metal/graphene top contact. As is known, transferred graphene has weaker adhesion to dielectric layers than to metal ones [23]. At the same time, the thermal contraction of the top contacts, which occurs after the deposition of metals and/or bonding of external leads, may further weaken the adhesion of graphene to sapphire. As a consequence, the probability of graphene detachment from the substrate in the area under the contact pads increases, and, hence, there is a risk of further breaking of the graphene layer continuity under the influence of uncontrolled external factors.

Figure 20.4a, b respectively show measured in-situ dependencies of sensitivity S and surface resistance R_S on fluence F at $F \geq 8.5\times10^{18}$ n·m^{-2} for one of the sensors. For other samples, these dependencies are qualitatively similar. In addition, Fig. 20.4c shows the dependence on the sample temperature $T(F)$, from which it is clear that the sensors during the experiment did not heat up above 55 °C.

The irradiation almost did not change sensors sensitivity: the difference between the initial and final values of S on Fig. 20.4a is ~3%, which is within the measurement error in the noisy environment of the nuclear reactor. However, $S(F)$ has a weakly expressed maximum at $F \approx 7\times10^{19}$ n·m^{-2}. Such a peculiarity cannot be

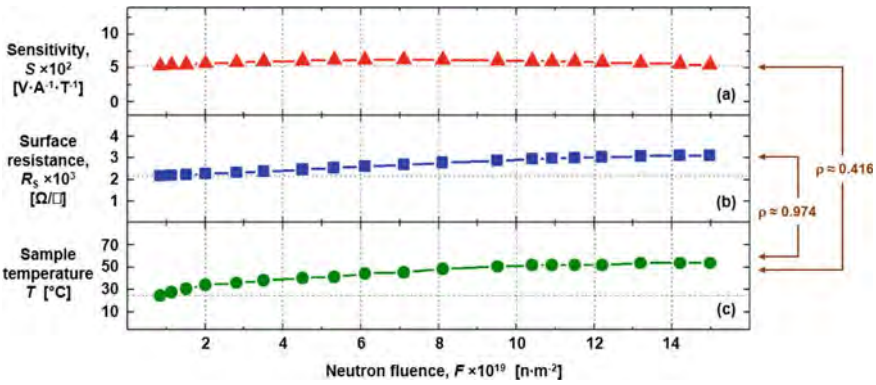

Fig. 20.4 Dependences of the parameters of one of the Hall sensors based on single-layer graphene on the neutron fluence obtained in-situ during the irradiation process: **a** sensitivity $S(F)$; **b** surface resistance $R_S(F)$; **c** temperature $T(F)$. Initial values of sample characteristics ($F = 0$): $S \approx 530$ V·A^{-1}·T^{-1}; $R_S \approx 2150$ Ω/□; $T \approx 25$ °C. ρ—Pearson's correlation coefficient

explained by damage to the crystal structure of graphene by neutrons, since in previous works the authors proved that graphene on a sapphire substrate is defect-free both at lower (4.6×10^{19} n·m^{-2}) and at higher (4.1×10^{20} n·m^{-2}) values of F [2]. On the other hand, $S(F)$ weakly correlates with $T(F)$: Pearson's correlation coefficient $\rho \approx 0.416$. Therefore, the maximum on $S(F)$ also cannot be related exclusively to thermal effects. In addition, during the temperature testing in the laboratory, the dependence $S(T)$ for all samples showed a linear character without extremums in the range 30 °C $\leq T \leq$ 54 °C. The possible cause of the maximum on Fig. 20.4a is that there are specific radiation-stimulated effects in the surrounding materials, resulting in a change in their electrostatic influence on graphene. This should, appropriately, affect the charge carriers density, which is inversely proportional to the sensitivity [17].

In contrast to sensor sensitivity, the graphene surface resistance demonstrated a much greater change after the end of in-situ experiment: the difference between the final and the initial value R_S in Fig. 20.4b is ~44%. Most probably, this result is related to the change in sample temperature T, as evidenced by strong correlation of the $R_S(F)$ and $T(F)$ data, $\rho \approx 0.974$. At the same time, as the literature analysis shows, electrical resistance of graphene is much less dependent on T. For example, the approximation of the results given in [8] for graphene on the SiO_2/Si substrate, shows that when heated from $T = 30$ °C to $T = 55$ °C the resistance of graphene increases only by ~6%. The possible cause of the observed behavior of R_S is the influence of metal/graphene contact resistance on the results of measurements by the van der Pauw method [11]. Neutrons can change the properties of these contacts, in particular, enhance resistance, as it occurs, for example, at the irradiation with low-energy electrons [10].

20.4 Conclusion

For the first time in the world, it was studied in-situ in the neutron fluxes of a research nuclear reactor the characteristics of Hall sensors based on CVD single-layer graphene transferred onto a sapphire substrate. The samples maintained a stable value of sensitivity to the magnetic field throughout the experiment that lasted until the fluence reached 1.5×10^{20} n·m^{-2}. The change in the surface resistance of graphene correlates with a change in temperature, the growth of which is due to radiation heat. The obtained results confirm the predictions regarding the high irradiation resistance of the graphene-based sensors in the neutron fluxes and also indicate their suitability for use in the plasma's magnetic diagnostic systems of fusion reactors. Further tests in the neutron fluxes will allow to determine the limit value of the fluence, at which the graphene sensors still remain operable. However, for conducting such research it is advisable to solve a number of technological problems, in particular, to optimize the selection of surrounding materials to minimize external impact on graphene during the irradiation and heating. This will allow to improve the stability of the samples,

to reduce the spread of their parameters, as well as to improve the metal/graphene electrical contacts.

Acknowledgements The work was supported by the Ministry of Education and Science of Ukraine and the Federal Ministry of Education and Research of Germany (Joint R&D Project M74-2018/RaMaG); the European Commission within the Graphene Flagship project (Contract No. 785219); the Joint Institute for Nuclear Research (Project 04-4-1122-2015/2020). The authors express their gratitude to Horst Windgassen for helping in deposition of gold for contact pads of sensors, and Stefan Scholz for helping in the bonding of gold leads.

References

1. W. Biel, R. Albanese, R. Ambrosino, M. Ariola, M.V. Berkel, I. Bolshakova et al.: Diagnostics for plasma control—from ITER to DEMO. Fusion Eng. Des. **146**(A), 465 (2019)
2. I. Bolshakova, D. Dyuzhkov, Ya. Kost, M. Radishevskiy, F. Shurigin, O. Vasyliev et al., in *Abstract Book of Graphene Week 2018 Conference*, San Sebastian, Spain, 10–14 September 2018, We-39
3. T. Botari, R. Paupitz, P. Alves da Silva Autreto, D.S. Galvao: Graphene healing mechanisms: a theoretical investigation. Carbon **99**, 302 (2016)
4. J. Buchheim, R.M. Wyss, I. Shorubalko, H.G. Park.: Understanding the interaction between energetic ions and freestanding graphene towards practical 2D perforation. Nanoscale **8**(15), 8345 (2016)
5. M. Bulavin, A. Cheplakov, V. Kukhtin, E. Kulagin, S. Kulikov et al.: Irradiation facility at the IBR-2 reactor for investigation of material radiation hardness. Nucl. Instrum. Meth. B **343**, 26 (2015)
6. D. Codorniu-Pujals, A. Bermudez-Martнnez, arXiv (2012). https://arxiv.org/abs/1210.4099
7. J. Dauber, A.A. Sagade, M. Oellers, K. Watanabe, T. Taniguchi, D. Neumaier, C. Stampfer: Ultra-sensitive hall sensors based on graphene encapsulated in hexagonal boron nitride. Appl. Phys. Lett. **106**(19), 193501 (2015)
8. B. Davaji, H.D. Cho, M. Malakoutian, J.-K. Lee, G. Panin et al.: A patterned single layer graphene resistance temperature sensor. Sci. Rep. **7**, 8811 (2017)
9. A.C. Ferrari, F. Bonaccorso, V. Falko, K.S. Novoselov, S. Roche, P. Boggild et al.: Science and technology roadmap for graphene, related two-dimensional crystals, and hybrid systems. Nanoscale **7**(11), 4598 (2015)
10. F. Giubileo, A. Di Bartolomeo, N. Martucciello, F. Romeo, L. Iemmo, P. Romano et al.: Contact resistance and channel conductance of graphene field-effect transistors under low-energy electron irradiation. Nanomater. **6**(11), 206 (2016)
11. G. Gonzalez-Diaz, D. Pastor, E. Garcia-Hemme, D. Montero, R. Garcia-Hernansanz, J. Olea et al.: A robust method to determine the contact resistance using the van der Pauw set up. Measurement **98**, 151 (2017)
12. C.N. Kryworuk, Thesis for the degree of Master of Science, Virginia Polytechnic Institute and State University, 2013
13. S. Kumar, A. Tripathi, S.A. Khan, C. Pannu, D.K. Avasthi: Radiation stability of graphene under extreme conditions. Appl. Phys. Lett. **105**, 133107 (2014)
14. S. Lee, J. Seo, J. Hong, S.H, Park, J.-H. Lee, B.-W. Min et al.: Proton irradiation energy dependence of defect formation in graphene. Appl. Surf. Sci. **344**, 52 (2015)
15. X. Li, Y. Zhu, W. Cai, M. Borysiak, B. Han, D. Chen et al.: Transfer of large-area graphene films for high-performance transparent conductive electrodes. Nano Lett. **9**(12), 4359 (2009)
16. J.B. Park, Y.-J. Kim, S.-M. Kim, J.M. Yoo, Y. Kim, R. Gorbachev et al.: Non-destructive electron microscopy imaging and analysis of biological samples with graphene coating. 2D Mater. **3**(4), 045004 (2016)

17. R.S. Popovic, *Hall Effect Devices*, 2nd edn. (IOP Publishing, Bristol, 2004)
18. G. Song, M. Ranjbar, R.A. Kiehl: Operation of graphene magnetic field sensors near the charge neutrality point. Commun. Phys. **2**, 65 (2019)
19. E.J. Strait, E.D. Fredrickson, J.-M. Moret, M. Takechi: Chapter 2: Magnetic diagnostics. Fusion Sci. Technol. **53**(2), 304 (2008)
20. L. Sun, F. Banhart, J. Warner: Two-dimensional materials under electron irradiation. MRS Bull. **40**(1), 29 (2015)
21. R.C. Walker II, T. Shi, E.C. Silva, I. Jovanovic, J.A. Robinson: Radiation effects on two-dimensional materials. Phys. Status Solidi A **213**(12), 3065 (2016)
22. H. Wang, C. Meng, H. Qu, X. Sun, P. Wang, D. Zhu, in *Proceedings of 9th International Particle Accelerator Conference*, Vancouver, Canada, 29 April–4 May 2018, pp. 47–50
23. T. Yoon, W.C. Shin, T.Y. Kim, J.H. Mun, T.-S. Kim, B.J. Cho: Direct measurement of adhesion energy of monolayer graphene as-grown on copper and its application to renewable transfer process. Nano Lett. **12**(3), 1448 (2012)
24. R. Zan, Q.M. Ramasse, U. Bangert, K.S. Novoselov: Graphene reknits its holes. Nano Lett. **12**(8), 3936 (2012)

Chapter 21
Adhesive and Barrier Sublayers for Metal Nanofilms Active Elements of Hall Sensors

I. A. Bolshakova, Ya. Ya. Kost, M. I. Radishevskyi, F. M. Shurygin, O. V. Vasyliev, I. S. Vasil'evskii, and T. Kuech

Abstract It was investigated the thermal stability of two types of Hall sensors based on gold nanofilms deposited on sapphire: (i) with the titanium adhesive sublayer (Ti/Au) and (ii) with the titanium adhesive sublayer and the platinum barrier sublayer of (Ti/Pt/Au). Vacuum annealing for 3 h at 400 °C significantly changes all investigated electrophysical parameters of samples with the Ti/Au metallization, which is explained by the titanium diffusion into gold. At the same time, the sensitivity and the resistivity of sensors with the Ti/Pt/Au metallization remain unchanged within a few percent, allowing them to be used in the plasma's magnetic diagnostic systems of the ITER and DEMO fusion reactors where operating temperatures will exceed 300 °C.

21.1 Introduction

It is assumed that the plasma's magnetic diagnostic system in the new generation's steady-state fusion reactors ITER and DEMO will include, as the front-end components, the Hall sensors with the high irradiation and thermal resistance, since the high neutron fluences $F \approx (10^{24}–10^{26})$ nm^{-2} and temperatures $T \geq 300$ °C are expected in their locations [1]. Traditional semiconductors, which form the basis of modern sensor technics, rapidly degrade in such environment, so the development of sensors based on other types of functional materials is topical.

Earlier, the authors of this work have shown the promise of the use of polycrystalline gold (Au) nanofilms in the ITER- and DEMO-relevant neutron fluxes [3].

I. A. Bolshakova (✉) · Ya. Ya. Kost · M. I. Radishevskyi · F. M. Shurygin · O. V. Vasyliev
Magnetic Sensor Laboratory, Lviv Polytechnic National University, Lviv, Ukraine
e-mail: inessa.bolshakova@gmail.com

I. S. Vasil'evskii
Institute of Functional Nuclear Electronics, National Research Nuclear University MEPhI, Moscow, Russia

T. Kuech
College of Engineering, University of Wisconsin-Madison, Madison, USA

A. D. Pogrebnjak et al. (eds.), *Nanomaterials in Biomedical Application and Biosensors (NAP-2019)*, Springer Proceedings in Physics 244,
https://doi.org/10.1007/978-981-15-3996-1_21

In-situ measurements in the research fast-neutron fission reactor have shown that the sensitivity of sensors based on Au nanofilms is preserved during their irradiation up to fluence $F \approx 10^{24}$ nm^{-2} without any signs of the material degradation (the given F value is related only to the available time of the reactor operation). At the same time, sensors based on nanoheterostructures of InAs/i-GaAs—the material with highest irradiation resistance among known semiconductors—are stable only up to $F \approx 10^{22}$ nm^{-2} [2]. The additional advantage of gold in comparison with semiconductors is the weak dependence of Hall coefficient on temperature in the DEMO-relevant range of its values [5, 15].

The Hall sensor's general stability is determined not only by its active element, but also by the substrate and the adhesion strength between them. Currently, authors of this work for the investigations of Au-based sensors use the substrates made from sapphire (single-crystal Al_2O_3), which has the high resistance to neutron irradiation and therefore is compatible with the fusion reactors' environment [14]. Modern technologies of the single crystals' growth and polishing allow to make sapphire substrates with a surface, sufficiently smooth (roughness <0.5 nm) to deposit on them the thickness-uniform metal nanofilms, and also with high thermal conductivity (~46 W·mK^{-1}), sufficient to remove heat from the active element when sensor operates in the radiation fluxes.[1]

Films of oxides and metals join with each other through oxygen ions, while the adhesion strength is determined by the activity of metal towards oxygen [7]. Gold is chemically inert and therefore has weak adhesion with Al_2O_3 oxide. The standard approach for its increasing is to deposit between Au and Al_2O_3 the titanium (Ti) nanosized adhesive sublayer which interacts much more strongly with oxygen in sapphire, but also has a high adhesion to gold [12]. The Ti/Au metallization is stable at comparatively low temperatures, but at $T > 175$ °C the Ti and Au mutual diffusion significantly increases [9, 10, 16]. Moreover, at $T \geq 250$ °C the AuTi, Au_4Ti, Au_2Ti and Ti_3Au intermetallic compounds are formed [10]. These processes may change irreversibly the electrophysical parameters of Hall sensors based on Au nanofilms, which authors already observed in previous investigations [4]. To solve the diffusion problem, additional barrier sublayers are used—made from platinum (Pt), palladium (Pd), ruthenium oxide (RuO), etc.—which prevent to the Au and Ti atoms' movement [11, 12]. In particular, it has been shown that on the Al_2O_3 substrates, the Ti/Pt/Au metallization system can preserve value of the gold's surface resistance when heated up to 500 °C [11]. This corresponds to the limit thermal loads for Hall sensors, which are expected in the DEMO reactor [1].

Goal of this work was to study an efficiency of the platinum barrier sublayer's use for the thermal stability improvement of the irradiation-resistant Hall sensors, based on gold nanofilms, deposited on sapphire with titanium adhesive sublayer.

[1] http://www.semiwafer.com/sapphire-wafer.html.

21.2 Experiment Details

21.2.1 Samples

Three batches of sensors with the same symmetric cross-like topology with four contact pads were made, Fig. 21.1a. Two batches had the Ti/Au metallization of active element (without a barrier sublayer) and differed only in the Au layer thickness: $h = 70$ nm and $h = 50$ nm, Fig. 21.1b. The third batch had the Ti/Pt/Au metallization (with barrier sublayer), with thicknesses of the Au layer of $h = 35$ nm and of the Pt-sublayer of $p = 5$ nm, Fig. 21.1c. For all samples, the thickness of the adhesive Ti sublayer thickness was the same $t = 4$ nm. Industrial sapphire plates with the thickness $a = 400$ μm were used as substrates.

Metals were sequentially deposited on sapphire by the Vacuum Thermal Deposition (VTD) method—for Ti/Au(50 nm) and Ti/Pt/Au; as well as by the Electronic Beam Evaporation (EBE) method—for Ti/Au(70 nm). To prevent the Ti oxidation and the water adatoms precipitation from the atmosphere on the interlayer interfaces, all active element's metals were deposited under same conditions without the vacuum deterioration.

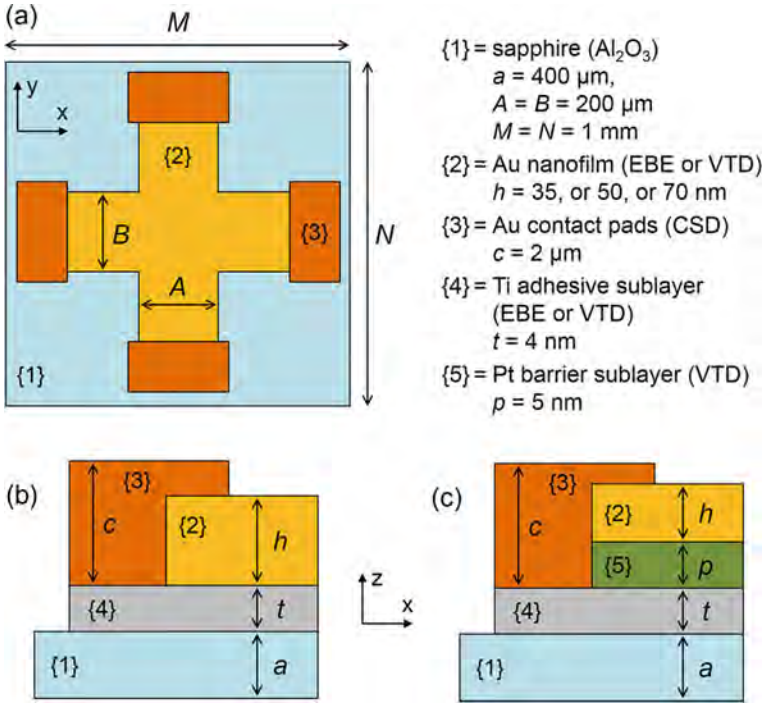

Fig. 21.1 Hall sensors' geometry (not to scale): **a** Chip with active element and contact pads; **b** Structure of layers for samples with the metallization of Ti/Au and **c** of Ti/Pt/Au

The sensor topology was formed by the lithography with lift-off. The active element's cross-hair sizes were $A = B = 200$ μm, Fig. 21.1a. In addition, the Au contact pads with the thickness of $c = 2$ μm, Fig. 21.1, were made at the active elements' ends with the using of lithography with following Chemical Solution Deposition (CSD). After that, the sapphire plates were diced into chips with sizes of $M = N =$ 1 mm. Each chip carried single sensor.

In order to connect sensors with measuring devices, external leads (gold wires with the 30-μm diameter) were bonded to thick Au contact pads with the help of thermo-compression bonding machine.

21.2.2 Measurement Technique

The Hall sensors' thermal resistance was studied by comparing their parameters—current-related sensitivity S_I, residual voltage (offset) V_0, resistivity ρ—before and after vacuum annealing.

As it is known, when applying magnetic field **B** perpendicular to the Hall sensor's surface and transmitting current through one pair of its opposite leads, the output voltage is generated on the other pair [13]:

$$V(I, B) = V_H(I, B) + V_0(I), \tag{21.1}$$

$$V_H(I, B) = \frac{R_H}{h} \cdot I \cdot B \tag{21.2}$$

where, V_H is Hall voltage; V_0— offset; I—supply current; B—magnetic induction; R_H—Hall coefficient for material of the active element; h—its thickness.

Hall voltage V_H is the sensor's useful signal and it determines the current-related sensitivity to magnetic field:

$$S_I = \left| \frac{V_H(I, B)}{I \cdot B} \right| = \left| \frac{R_H}{h} \right|. \tag{21.3}$$

It is seen from (21.3) that S_I depends on the active element's thickness h, which can change due to the diffusion of atoms from the adhesive sublayer. Moreover, diffusion can affect Hall constant R_H, which is sensitive to the material composition. Consequently, the diffusion processes' minimization is a key factor to ensure the sensitivity's stability, especially at elevated temperatures.

Offset V_0 in (21.1) is a spurious signal that limits the sensor's resolution. Offset arises due to the asymmetry of the leads placement or of the active element's topology, its material nonuniformity by structure or by thickness, etc. [13]. Modern magnetic measuring systems use special methods of signal processing to eliminate offset and to extract V_H from the output signal (21.1). However, in cases when offset changes

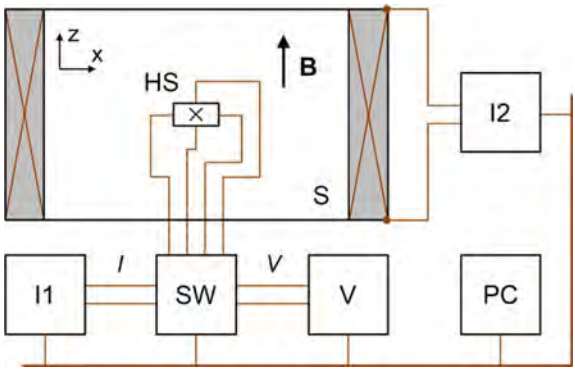

Fig. 21.2 General layout of measuring bench (*see details in text*)

uncontrollably, for example, due to diffusion, the effectiveness of these methods can reduce. It requires to study separately the stability of both sensitivity and offset.

I this work, the spinning-current method was used to determine V_H and V_0 [13]. It lies in the averaging of several output voltage's values V, measured at different configurations of the sensor's opposite leads connection to the current source and voltmeter. Measurements were carried out at the bench which general layout is shown in Fig. 21.2. Leads of Hall sensor (HS) were connected through the 4 × 4 switch (SW) to the Keithley 220 stable current source (I1) and Keithley 2182 nanovoltmeter (V). In order to create a magnetic field **B** it was used a solenoid (S) powered by the Tektronix PWS2323 current source (I2). The computer (PC) with special software carried out the measuring process control, data collecting, processing and storing.

Using the bench, the samples resistivity ρ also was determined by the van der Pauw method [13]. It involves the calculation of the sensor's transverse resistance R_T, based on results of the output voltage measuring the on one pair of its adjacent leads when transmitting a current through another pair and at $B = 0$. Respectively [13]:

$$\rho = \frac{\pi}{\ln 2} \cdot h \cdot \langle R_T \rangle, \tag{21.4}$$

where $<R_T>$ is average value of the transverse resistance's two values, obtained at the current transmitting in mutually perpendicular directions.

21.3 Results and Discussion

Samples was annealed in the vacuum (residual pressure ~10^{-3} Pa) for 3 h at temperature of $T \approx 400$ °C, which corresponds to the average level of thermal loads on Hall sensors expected in DEMO [1].

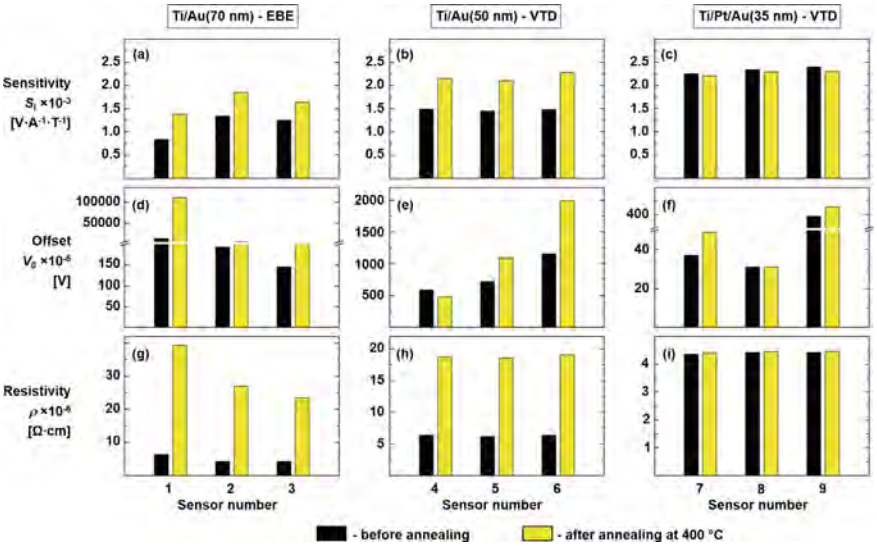

Fig. 21.3 Parameters of Hall sensors with the active element's metallization of Ti/Au(70 nm) (*left*), Ti/Au(50 nm) (*middle*) and Ti/Pt/Au(35 nm) (*right*) before (*black columns*) and after (*yellow columns*) vacuum annealing for 3 h at $T \approx 400$ °C: **a–c** current-related sensitivity S_I; **d–f** residual voltage (offset) V_0; **g–i** resistivity ρ. Sample numbers match the data in Table 21.1

In order to demonstrate the observed effects it was randomly selected three sensors from each samples batch. Figure 21.3 compares for them the sensitivity S_I, offset V_0 and resistivity ρ values measured before (black columns) and after (yellow columns) annealing. Data for S_I are represented on the same vertical axis scale, while for V_0 and ρ the axis scale and breaks are selected for the perception convenience. Relative changes of these parameters (ΔS_I, ΔV_0 and $\Delta\rho$) are given in Table 21.1.

Table 21.1 Relative change in sensors' parameters after annealing (sample numbers coincide with the numbers in Fig. 21.3)

Metallization	No	ΔS_I (%)	ΔV_0 (%)	$\Delta\rho$ (%)
Ti/Au(70 nm) EBE	1	64	702	520
	2	38	3145	533
	3	31	667	447
Ti/Au(50 nm) VTD	4	44	−18	194
	5	45	53	201
	6	54	73	201
Ti/Pt/Au(35 nm) VTD	7	−2	32	1
	8	−2	0	1
	9	−4	9	1

From Fig. 21.3 it is seen, that before annealing, each samples batch had its own average sensitivity value, since it is determined by the gold layer's thickness h, set when manufacturing. Resistivity for all samples was within the range of $\rho \approx (4 - 6) \times 10^{-6}$ Ω cm, which is consistent with the dimensional effects studies in Au nanofilms [8]. Insignificant spread in S_I and ρ within each batch can be explained by divergence of h for different samples, which occurs because a thickness of the film deposited by the EBE or VTD method, as a rule, tends to slightly decrease in the direction from the substrate's center to its periphery. Regarding offset, then the spread of its value V_0 in each batch was much stronger than the spread of S_I and ρ. This fully corresponds to the nature of origin of this spurious signal, which is sensitive to any inhomogeneities in the material. It should be noted that in sensors with the Ti/Pt/Au metallization, the average offset was smaller. The possible reason for this is the Pt sublayer effect on the Au film growth process, resulting in less inhomogeneities.

As it is seen from Fig. 21.3 and Table 21.1, annealing almost did not affect (within measurement error) the sensitivity S_I and resistivity ρ of sensors with the Ti/Pt/Au metallization, but significantly changed these parameters for sensors with Ti/Au. Such changes can be explained by the diffusion of titanium into gold, which occurs without barrier sublayer.

To do this, consider the Ti/Au interface, Fig. 21.4, in which, after annealing, Ti atoms diffused into Au at certain average depth Δh. Obviously, due to diffusion, the resistivity in the gold layer has distributed in the nonhomogeneous manner along its thickness between the two limit values ρ_{Au} (in Au) and ρ_{Ti} (in Ti). For simplicity, resistivity profile ρ(z) in Fig. 21.4 is shown schematically, whereas ρ_{Au} and ρ_{Ti} values are taken for bulk samples of pure metals: $\rho_{Au} \approx 2 \times 10^{-6}$ Ω·cm and $\rho_{Ti} \approx 42 \times 10^{-6}$ Ω·cm [6]. Since $\rho_{Au} << \rho_{Ti}$, then the current supplied to the sensor flows mainly through the near-surface Au layer with thickness of $(h - \Delta h) < h$ with the minimal resistance, as shown schematically by the current density vector's distribution **j**(z)

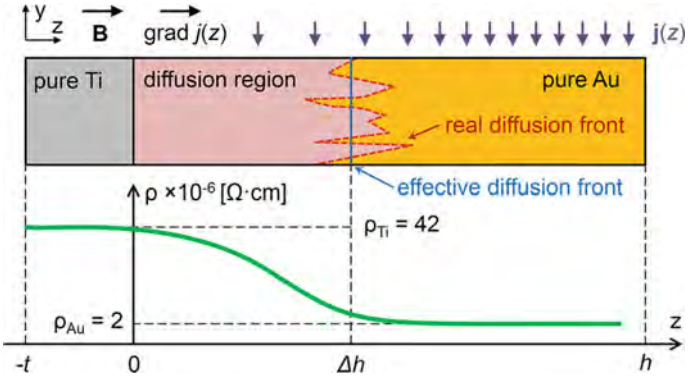

Fig. 21.4 Ti/Au interface with the diffusion region formed after annealing (*top*), and schematic resistivity distribution (*bottom*). **j**(z) is a supply current density. Values ρ_{Au} and ρ_{Ti} are taken for pure bulk samples of Ti and Au from [6]

in Fig. 21.4. According to (21.3), this should increase the sensor sensitivity S_I, as observed in the experiment, Fig. 21.3a, b. In addition, when measuring with the van der Pauw method, the decrease in thickness of the layer through which the current flows should increase the measured value of the sample's transverse resistance $<R_T>$. Accordingly, the application of (21.4) without correction for Δh will result in an increase in calculated value of ρ, as is it seen in Fig. 21.3g, h.

Offset changes after annealing are noticeable for all sensors studied, although, in general, they have less law-governed character than those observed in the case of S_I and ρ: for most samples, the value of V_0 has increased after annealing, but for some ones, on the contrary, decreased, Fig. 21.3 and Table 21.1. The offset change can be connected with the recrystallization effects in the gold active elements, or with the mechanical stresses' initiation due to the thermal expansion coefficients' mismatch for sapphire and gold, etc.

It should be noted that when using the Pt barrier layer, change in V_0 on average was less, Table 21.1. This may also indicate a certain role of diffusion in the offset change. For example, it is known that the diffusion of titanium into polycrystalline gold occurs both in the individual grains volume and in the intergranuale space [9]. This can form the developed relief of diffusion front, Fig. 21.4, which, in turn, leads to the non-uniform distribution of resistivity in the active element's volume, and the distortion of the electric field's equipotential lines in the material when current transmits through it.

21.4 Conclusions

The use of additional platinum barrier sublayer enhances the thermal stability of Hall sensors based on gold nanofilms, deposited on sapphire with titanium adhesive sublayer, during vacuum annealing at 400 °C for 3 h. This fact, together with the previously proven high resistance of such sensors to the intense neutron fluxes' impact, allows them to be used as the front-end components of the plasma's magnetic diagnostic systems in the fusion reactors of ITER and DEMO type, where temperatures above 300 °C are expected.

Acknowledgements This work has been carried out within the framework of the EUROfusion Consortium and has received funding from the Euratom research and training programme 2014–2018 and 2019–2020 under grant agreement No 633053. The views and opinions expressed herein do not necessarily reflect those of the European Commission.

References

1. W. Biel, *Report Presented at the International School of Fusion Reactors Technology*, Erice, Italy, 28 Apr–4 May 2017

2. I. Bolshakova, S. Belyaev, M. Bulavin, V. Brudnyi, V. Chekanov, V. Coccorese et al., Experimental evaluation of stable long term operation of semiconductor magnetic sensors at ITER relevant environment. Nucl. Fusion **55**(8), 083006 (2015)
3. I. Bolshakova, M. Bulavin, N. Kargin, Ya. Kost, T. Kuech, S. Kulikov et al., Metal hall sensors for the new generation fusion reactors of DEMO scale. Nucl. Fusion **57**(11), 116042 (2017)
4. I. Bolshakova, F. Shurygin, A. Moroz, Y. Kost, Y. Mykhashchuk, M. Radishevskiy et al., in *Proceedings of 14th International Conference on Advanced Trends in Radioelectronics, Telecommunications and Computer Engineering* (Lviv-Slavske, Ukraine, 20–24 Feb 2018), p. 381
5. V. Frank, Hall coefficient of technically pure metals from 80°K to 800°K. II. Results for Zr, W, Mo, Ta, Nb and Al. survey of results for the 4d- and 5d-transition group of metals. Appl. Sci. Res. B **7**(1), 41 (1959)
6. I.S. Grigoriev, E.Z. Meilikhov (eds.), *Handbook of Physical Quantities* (CRC Press, Boca Raton, 1997)
7. L.-H. Lee (ed.), *Fundamentals of Adhesion* (Springer Science + Business Media, New York, 1991)
8. W.G. Ma, H.D. Wang, X. Zhang, W. Wang, Experiment study of the size effects on electron-phonon relaxation and electrical resistivity of polycrystalline thin gold films. J. Appl. Phys. **108**(6), 064308 (2010)
9. W.E. Martinez, G. Gregori, T. Mates, Titanium diffusion in gold thin films. Thin Solid Films **518**(10), 2585 (2010)
10. K. Masahiro, S. Noboru, Effects of temperature, thickness and atmosphere on mixing in Au-Ti bilayer thin films. J. Mater. Sci. **28**(18), 5088 (1993)
11. M. Matsui, Thermal stability of Au thin film deposited on Al_2O_3 substrate with RuO_2 adhesion layer. J. Ceram. Soc. Jpn. **109**(6), 574 (2001)
12. D.M. Mattox, *Handbook of Physical Vapor Deposition (PVD) Processing* (Elsevier Inc., Amsterdam, 2010)
13. R.S. Popovic, *Hall Effect Devices*, 2nd edn. (IOP Publishing, Bristol, 2004)
14. T. Shikama, S.J. Zinkle, Long term degradation of electrical insulation of Al_2O_3 under high flux fission reactor irradiation. J. Nucl. Mater. **258–263**, 1861 (1998)
15. C.R. Tellier, Thin metal film senosors. Active Passive Electron. Comp. **12**(1), 9 (1985)
16. M. Todeschini, A.B. da Silva Fanta, F. Jensen, J.B. Wagner, A. Han, Influence of Ti and Cr adhesion layers on ultrathin Au films. ACS Appl. Mater. Interf. **9**(42), 37374 (2017)

Chapter 22
Morphology and Luminescence Properties of Cellulose-CNT-$BiPO_4$:Pr^{3+} Composites

V. P. Chornii, V. V. Boyko, S. G. Nedilko, M. S. Slobodyanyk, V. P. Scherbatskyi, and K. V. Terebilenko

Abstract The peculiarities of preparation and properties of composites which consist of cellulose matrix, multiwall carbon nanotubes and praseodymium-doped bismuth phosphate nanoparticles are reported. The SEM images show that oxide particles are incorporated into cellulose when their sizes below 100 nm and can pierce out of composite surface in case of bigger particles. The carbon nanotubes are clearly observed only at the regions near oxide particles that can be explained by close adhesion between these components of composites. Chemical element analysis shows the composites of lower content of nanotubes possess better homogeneity from viewpoint of elements distribution. The studied composites reveal intensive luminescence under excitation at 405 and 473 nm. The photoluminescence spectra depend on the PL excitation wavelength and related mostly with cellulose host emission centers. The Pr^{3+}-related emission clearly observed only in the case of composites of higher content of nanotubes at direct PL excitation of $^3H_4 \rightarrow {}^3P_1 + {}^1I_6$ absorption transitions in praseodymium ions.

22.1 Introduction

Cellulose is one of the most common natural polymers with possible application in various branches of technology e.g. biofuels, eco-friendly sorbents and "paper electronics" [1–3]. The variety of its possible application is determined by structure of cellulose (porous material with easy incorporation of micro/nanoparticles), its good mechanical properties and relatively low costs of production due to abundance of cellulose sources in nature.

V. P. Chornii (✉) · V. V. Boyko
National University of Life and Environmental Sciences of Ukraine, Kiev, Ukraine
e-mail: vchornii@gmail.com

V. P. Chornii · S. G. Nedilko · M. S. Slobodyanyk · V. P. Scherbatskyi · K. V. Terebilenko
Taras Shevchenko National University of Kyiv, Kiev, Ukraine

A. D. Pogrebnjak et al. (eds.), *Nanomaterials in Biomedical Application and Biosensors (NAP-2019)*, Springer Proceedings in Physics 244,
https://doi.org/10.1007/978-981-15-3996-1_22

Functionalization of cellulose or design of cellulose-based composites can considerably improve certain properties of this natural polymer according to application goals. In particular, adding of metal salts and oxides improves antibacterial and UV-protecting properties of cellulose [4]. Novel photocatalytic materials can be elaborated on base of TiO_2-doped cellulose [4]. Micro/nanoparticles of some oxide compounds when being added to cellulose, significantly affect photoluminescence (PL) properties and dielectric constants of the latter one [5–7]. The essential advantage of oxide luminescent compounds as modifiers is their stability, thus it is difficult to remove them from the cellulosic fiber even using a special treatment. That is why, cellulose fibers with inorganic luminescent particles are perspective for various applications in the textile industry, as well as for the protection of documents [7]. At the same time adding of inorganic filler to cellulose host influences on its mechanical properties [8]. Addition of zirconia to cellulose fibers decreased tenacity and elongation at break values [7]. From other hand mechanical, thermal and electrical properties of various polymers, in particular cellulose can be greatly improved by adding some amount of carbon nanotubes (CNT) [9–14]. CNTs have good light absorption in all visible spectral range, thus it is expected that absorption edge of composites containing of CNTs should move to lower energies.

In this work the data on preparation of the composites consisted of micro/nanocellulose, $BiPO_4:Pr^{3+}$ oxide and carbon nanotubes as well as results of composites' morphology and luminescent properties study are reported.

22.2 Experiment Details

The pure cellulose tablets (produced by ANCYR-B, Ukraine) were grinded and dispersed using high-speed rotation mill. The amount of starting cellulose in all prepared samples of composites was equal to 2.00 g and amount of $BiPO_4$:0.01%Pr^{3+} oxide component was equal to 0.20 g. Carbon nanotubes in weight of 0.01 g and 0.02 g were added to cellulose in composite samples denoted as C1 and C2 respectively. The weighted amount of cellulose, oxide and nanotubes were thoroughly grinded in porcelain crucibles. The used in experiments powders were pressed under pressure 1.8×10^4 kPa/m^2 into discs with average diameter near 10.3 mm.

The Scanning electron microscope (SEM) JAMP-9500F Field Emission Auger Microprobe (JEOL, USA) equipped with X-ray microanalyzer INCA PentaFETx3 (Oxford instruments) was used for SEM measurements. Besides the SEM imaging, microelement analysis of various areas of the samples was also performed using the same microscope.

Photoluminescence (PL) properties of the composites were measured in 400–750 nm spectral range using DFS-12 double diffraction grating monochromator equipped with photomultiplier FEU-79. Diode-pumped lasers (λ_{em} = 405 and 473 nm) were used as excitation light sources. The PL studies were performed at room temperature. All the PL emission spectra were corrected on system responses.

22.3 Results and Discussion

The SEM images for the samples C1 and C2 are shown on Fig. 22.1 at top and bottom of figure, respectively. For both samples the incorporation of oxide nanoparticles (grains sizes below 100 nm) into cellulose host is clearly observed. Larger oxide particles (sizes above 100 nm) pierce out of the composite surface (bottom right part of images). Thus, it is likely to be the nanoparticles of $BiPO_4$ oxide that easily occupy pores in cellulose forming "ceramic-like" samples but incorporation of larger oxide particles leads to local inhomogeneity of samples. This observation reveals that from viewpoint of homogeneity the used method for preparation of composites not as good as that one described in [8]. The CNTs effect on structure is difficultly described from SEM results. Some amount of the carbon nanotubes can be found only at the middle part of SEM image of C2 sample, while no CNTs can be found on SEM image of C1 sample. Interestingly, the CNTs lay only close to oxide particles. This observation can mean that nanotubes have been adsorbed on oxide surfaces.

The chemical elements analysis was performed in three different areas of each of the samples. Spectra 1 and 2 were recorded in the "homogenous" region and spectrum 3—on grains associated with large oxide particles. The results are collected in Table 22.1. It is seen from table, the content of carbon is much higher in the case of sample C2. Such effect can be explained by higher content of CNTs in composite

Fig. 22.1 SEM images of C1 (left) and C2 samples (right)

Table 22.1 Content of some chemical elements in different areas of samples C1 and C2 (in at. %)

Sample	Region	C	O	P	Bi
C1	1	23.09	52.53	11.59	12.79
	2	24.27	50.68	11.62	13.43
	3	21.11	53.46	12.09	13.35
C2	1	85.54	13.97	0.04	0.46
	2	83.46	16.32	0.03	0.19
	3	57.05	34.30	3.87	4.78

C2. Interestingly, the sample C1, from viewpoint of chemical element distribution, is more homogenous than C2. The ratios between the elements are very similar to corresponding ratios for regions without pierced out oxide particles even for areas of C1 close to oxide particles. At the same time, chemical elements analysis showed that content of elements strongly depends on the areas of the sample C2 chosen for experiments. This observation can be ascribed to increased interaction between components of studied composites with increasing content of carbon nanotubes.

It is worth noting that excited beam had diameter near 3 mm and therefore studied luminescence properties can be treated as integrated ones in relatively large area of the samples. We suggest the local inhomogeneity of samples does not affect much on the PL properties. In order to verify this suggestion the PL emission was studied at 3 different areas at each sample and it was found that PL spectra at different area of samples are very similar. The PL emission spectra of composites measured under excitation with $\lambda_{ex} = 473$ nm are shown on Fig. 22.2. It is seen the PL emission for both composites consist of broad band with maxima near 550 nm. This band was earlier ascribed to luminescence centers of various origins in the micro/nanocellulose [8]. Increasing of CNTs content in composites leads to significant decreasing of the cellulose host photoluminescence. At the same time, two additional bands appear in the spectrum of C2 sample. These bands have maxima near 608 and 660 nm that matched well with typical positions of $^3P_0 \rightarrow {}^3H_6$ and $^3P_0 \rightarrow {}^3F_2$ radiation transitions in Pr^{3+} ions [15]. The luminescence of Pr^{3+} ions was expected because the excitation light with $\lambda_{ex} = 473$ nm correspond to $^3H_4 \rightarrow {}^3P_1 + {}^1I_6$ absorption transitions in $BiPO_4$:Pr^{3+} compound [16].

It is looks like the PL excitation processes for luminescence centers in cellulose and oxide components of composites compete each other. Due to small amount of oxide component the Pr^{3+}-related centers, obviously, have much smaller concentration than cellulose-related centers. As result, a luminescence of cellulose is dominant in PL spectra of both composites. At the same time, carbon nanotubes actively

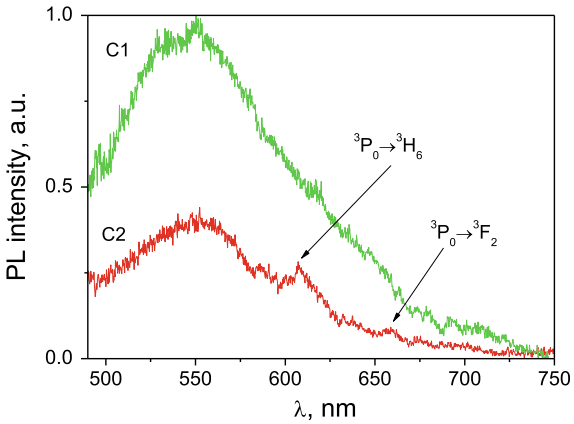

Fig. 22.2 PL spectra of C1 and C2 composites; $\lambda_{ex} = 473$ nm, T = 300 K

participate in luminescence processes, resulting in suppression of cellulose-related luminescence. The effect of CNTs on PL emission of Pr^{3+} ions is unclear and requires further studies.

PL emission was studied also under excitation at $\lambda_{ex} = 405$ nm (this wavelength corresponds to photon energy 3.06 eV). Such photon energy allows excluding direct excitation of Pr^{3+} ions, and also it is much lower than needed for band-to-band absorption of $BiPO_4$ (the band gap of this oxide compound is near 4.8 eV). Thus, only light absorption by cellulose and CNTs take place. As Fig. 22.3 shows, under excitation with $\lambda_{ex} = 405$ nm only broad bands in emission spectra for both C1 and C2 composites are observed. The PL bands have same shape and maxima positions (located near 500 nm). The only difference between spectra on Fig. 22.3 is intensities. Similarly to the case of 473 nm excitation, luminescence intensity of C2 composite is near of 2 times lower than for C1 one.

Decomposition of the photoluminescence spectra on elementary bands allows easily distinguishing spectral changes. Such decompositions were performed for PL spectra using Gaussian curves. The positions of the band maxima ($h\nu_{max}$), full width at half maximum (FWHM), and areas under bands are shown in Table 22.2.

It is seen from table that he main PL emission bands have their maxima at 2.34 eV (530 nm) and 2.24 eV (554 nm) for PL excitation at 405 and 473 nm, respectively. Increasing of CNT content in composites decreases total intensity (area under corresponding band) in almost three times. There are additional weak bands in PL spectra at mentioned PL excitations. In case of $\lambda_{ex} = 405$ nm the additional band have maximum at higher energies and for $\lambda_{ex} = 473$ nm at lower energies in respect to main PL bands. The band at 2.6 eV (477 nm) can be ascribed to cellulose host, because its width is relatively large for the Pr^{3+} emission bands in that region. The band with maximum at 1.94 eV (640 nm) have relatively small FWHM and can be ascribed to unresolved Pr^{3+} emission related with superposition of radiation transitions from

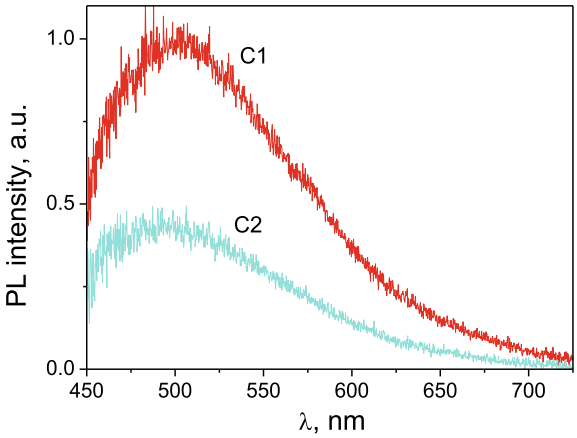

Fig. 22.3 PL spectra of C1 and C2 composites; $\lambda_{ex} = 405$ nm, T = 300 K

Table 22.2 Parameters of PL spectra decompositions

Sample	λ_{ex} (nm)	$h\nu_{max}$ (eV)	FWHM (eV)	Area (a.u.)
C1	405	2.34	0.60	0.097
		2.60	0.35	0.015
	473	1.94	0.15	0.003
		2.24	0.47	0.090
C2	405	2.34	0.60	0.037
		2.63	0.46	0.013
	473	2.24	0.43	0.032

$^3P_0$ on $^3H_6$ and $^3F_2$ levels. The PL emission related with these transitions clearly observed for the case of C2 sample under excitation at 473 nm.

22.4 Conclusions

Two sets of cellulose-CNT-$BiPO_4$:Pr composites have been prepared. Chemical elements analysis and scanning electron microscopy showed that composite samples of lower carbon nanotubes content are more homogeneous. Both composites reveal intensive luminescence under PL excitations at 405 and 473 nm. The most intensive PL bands were ascribed to luminescence centers in a cellulose host. The Pr^{3+}-related emission centers are clearly observed for the case of composites with higher content of carbon nanotubes.

References

1. K. Nelson, T. Retsina, M. Iakovlev, A. van Heiningen, Y. Deng, J.A. Shatkin, A. Mulyadi, in *Materials Research for Manufacturing*, ed. by L.D. Madsen, E.B. Svedberg (Springer, Cham, 2016), p. 267
2. S.G. Nedilko, S.L. Revo, V.P. Chornii, V.P. Scherbatskyi, M.S. Nedielko, J. Sens. Sens. Syst. **4**, 31 (2015)
3. S. Yun, S.D. Jang, G.Y. Yun, J.H. Kim, J. Kim, Appl. Phys. Lett. **95**, 104102 (2009)
4. H.E. Emam, Cellulose **26**, 1431 (2019)
5. S.G. Nedilko, Acta Phys. Pol. A **133**, 829 (2018)
6. L. Zhang, S. Lyu, Z. Chen, S. Wang, Nanomaterials **8**, 352 (2018)
7. P. Kulpinski, A. Erdman, M. Namyslak, J.D. Fidelus, Cellulose **19**, 1259 (2012)
8. M. Nedielko, S. Hamamda, O. Alekseev, V. Chornii, M. Dashevskii, M. Lazarenko et al., Nanoscale Res. Lett. **12**, 98 (2017)
9. S. Zhang, F. Zhang, Y. Pan, L. Jin, B. Liu, Y. Mao et al., RSC Adv. **8**, 5678 (2018)
10. A. Pantano, in *Carbon Nanotube-Reinforced Polymers*, ed. by R. Rafiee (Elsevier, Amsterdam, 2018), p. 201
11. A. Salama, A. Mohamed, N.M. Aboamera, T. Osman, A. Khattab, Adv. Polym. Technol. **37**, 2446 (2018)

12. Z. Pang, X. Sun, X. Wu, Y. Nie, Z. Liu, L. Yue, Vacuum **122**, 135 (2015)
13. M.R. Loos, K. Schulte, in *Carbon Nanotube-Reinforced Polymers*, ed. by M.R. Loos (Elsevier, Amsterdam, 2015), p. 207
14. R. Khare, S. Bose, J. Min. Mater. Character. Eng. **4**, 31 (2005)
15. V.K. Tikhomirov, S.A. Tikhomirova, J. Non-Cryst. Solids **274**, 50 (2000)
16. V.P. Chornii, S.G. Nedilko, K.L. Bychkov, K.V. Terebilenko, M.S. Slobodyanik, V.V. Boyko, Acta Phys. Pol. A **133**, 843 (2018)

Chapter 23
Time Dependence of X-Ray Luminescence from Yttrium Oxide Nanoceramics

S. Kononenko, R. Skiba, I. Mysiura, O. Kalantaryan, V. Zhurenko, V. Chishkala, and M. Azarenkov

Abstract 250–750 nm luminescence of yttrium oxide nanoceramics which are of great interest for several biomedicine applications was measured under the influence of X-ray radiation with up to 60 keV energy. The ceramics was produced from yttrium oxide nanopowder by sintering technique. The time dependence of the luminescent intensity at the 350 nm was investigated. It was shown that the decreasing intensity curve was good approximated by two-exponential function, which indicated the presence of fast and slow processes inducing the luminescence. The cyclic irradiation of the same sample showed that during the absence of irradiation an evident regeneration of the luminescent intensity occurred. The initial value of the intensity registered for each subsequent reirradiation significantly exceeded the final value of the intensity measured for the previous cycle. Wherein, the intensity decreased to a certain saturation value at the end of each cycle.

23.1 Introduction

Yttrium oxide (Y_2O_3) is promising phosphor material in terms of fast response and light yield, in particular, in the field of registration of ionizing radiation [1, 2]. Moreover yttrium oxide is a perspective material for biological imaging applications. It is widely used in medicine, for example, as ceramics for prostheses [3], as an element with upconversion of infrared radiation into visible radiation in cancer cell detection markers [4], and as a functional element of toxic methanol ultrasensitive sensors at room temperature [5]. Considerable practical interest to Y_2O_3 nanoceramics is connected with its possible use as a radiation detector for X-ray quanta with energies of about ten kiloelectronvolts and γ-radiation. Here, knowledge of variability of Y_2O_3 ceramic spectral and kinetic characteristics depending on different irradiation factors is important.

S. Kononenko (✉) · R. Skiba · I. Mysiura · O. Kalantaryan · V. Zhurenko · V. Chishkala · M. Azarenkov
V. N. Karazin Kharkiv National University, Kharkiv, Ukraine
e-mail: sergiy.i.kononenko@gmail.com

A. D. Pogrebnjak et al. (eds.), *Nanomaterials in Biomedical Application and Biosensors (NAP-2019)*, Springer Proceedings in Physics 244,
https://doi.org/10.1007/978-981-15-3996-1_23

Luminescence of Y_2O_3 powder and ceramic samples was studied for different types of irradiation, namely iono- [6], heat stimulated- [7], cathode- [8] and X-ray luminescence [9, 10], as well as upon excitation by a nitrogen laser ($\lambda = 337.2$ nm) [10, 11]. Wide band luminescence with maximum at 350 nm was typical for light spectra of Y_2O_3 exposed to various radiations. The same band we also observed for Y_2O_3 powder and ceramics irradiated by 60 keV X-ray photons earlier [12].

It is well known that Y_2O_3 crystals with 6 eV width of band gap have a cubic syngony with the space group T7h [13]. When wide-gap dielectrics is exposed to ionizing radiation, decay of excitons, especially self-trapped excitons (STE), play an important role both in light generation processes and defect formation processes. A number of authors considered radiation decay of STE to be the main reason for a luminescence light emission at the band with maximum 350 nm (see, e.g., Fukabori [2], Lushchik [14], Guerassimova et al. [15], Novosad et al. [16]). For example, X-ray excitation of Y_2O_3 ceramic material at 85–295 °K temperature induced the intense luminescence, which spectrum was good fitted into the elementary Gaussian shape bands with several maxima [16]. The authors stated that 3.4 eV band of the luminescence was caused by STE of $(YO_6)_9$—complex, when the cation was localized in the field of the trigonal (C3i) and monoclinic (C2) symmetries. However, it is worth noting that exact source of this emission peak is not finally determined yet. So the authors [17] pointed out that in the case of transparent Y_2O_3 ceramics and radio-luminescence induced by 241Am α-ray excitation the origin of 350 nm emission peaks was trapped excitons, i.e. excitons were trapped by point defects, dislocations, grain boundaries (in the case of ceramics), and stacking faults.

Most often, yttrium oxide spectral characteristics study are aimed to identify features associated with the methods of specimen production, doping it with various elements (see, e.g., Novosad et al. [16], Stanton et al. [18], Robindro Singh [19]). Luminescent radiation is the resultant effect of external radiation on defect centres, i.e., it carries information about the structure of a solid, being the dynamics of competing processes of excitation, formation and annealing of defects. At the same time, the spectral characteristics of the samples can undergo significant changes under the influence of intense ionizing radiation. Therefore, it is interesting to study the dynamics of changes of the luminescent radiation intensity as a function of time (or irradiation dose) of X-ray exposure especially for biomedicine applications.

The paper deals with experimental study of changes in the luminescent intensity at wavelength of 350 nm for yttrium oxide nanoceramics, depending on the irradiation time (so-called luminescence kinetics).

23.2 Experiment

The measurements of X-ray luminescence were done at room temperature on the spectrometric complex schematically shown on Fig. 23.1. The irradiation was provided by X-ray unit. The vacuum tube with copper anode and beryllium window was a source of X-ray radiation. Operating voltage of the X-ray tube was up to 60 kV

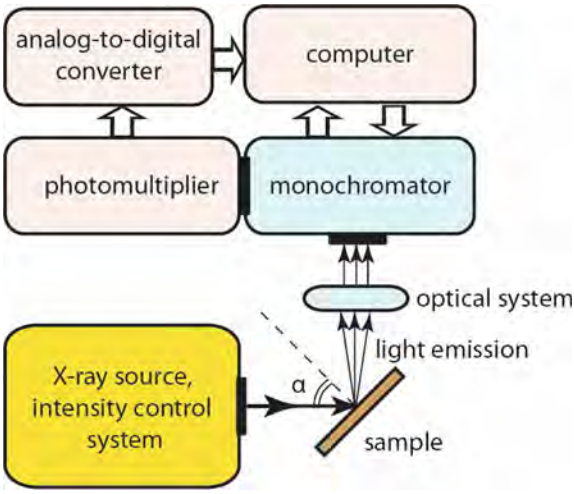

Fig. 23.1 Experimental setup

and current value was 10 mA. The intensity of X-ray radiation was controlled and stabilized by X-ray intensity control system during the experiments. The irradiation duration for each sample under study was 7200 s and the maximum exposure dose was approximately 12.37 C/kg.

The excitation radiation fell on the sample at an angle of 45°. Luminescent light was focused by means of optical system on the entrance slit of grating monochromator (wavelength range 250–750 nm). The resulting signal was detected by photomultiplier connected to the entrance amplifier unit of the analog-digital converter and further transmitted to computer. The spectrometric complex was calibrated by spectrophotometric filament tungsten lamp. The luminescent spectra were corrected to the spectral sensitivity of the apparatus.

The experiments were carried out with samples made from Y_2O_3 powder with purity of 99.99%. The powder consisted of both nano- and micro-sized particles (Fig. 23.2). The ceramics samples were made by sintering technique. At the beginning the compression was performed by the compaction of the powder in a cylindrical tablet 10 mm in diameter and 5 mm thickness (approximately 4×10^3 kg/cm^2). In the second stage the sintering took place in vacuum electric furnace (residual gas pressure 5×10^{-4} Pa) in an alumina crucible at temperature of 1500 °C. The sintering duration was 1 h. At the last stage the samples were cleaned and prepared for installation into the spectrometric complex. The structural state of the samples was examined using X-ray diffractometer DRON-4-07. We used Cu-Kα radiation applying Ni selectively absorbing filter.

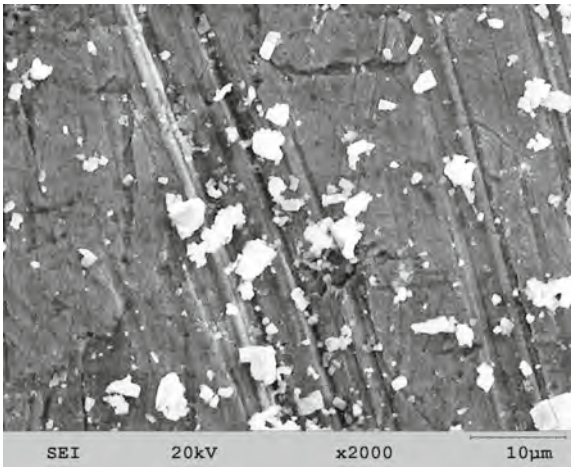

Fig. 23.2 Scanning electron microscope image of Y_2O_3 powder

23.3 Results and Discussions

Figure 23.3 shows the typical XRD pattern for Y_2O_3 sample. The structure is single phase; it contains cubic yttrium oxide peaks (space group #206). The lattice parameters of yttrium oxide are slightly higher than handbook values, but for all samples the measurements are the same within the measurement error. The intensity distribution of the diffraction lines corresponds to the polycrystalline non-textured state; the lines have a small half-width, that is, the sample is in a large-crystalline state.

We measured luminescent spectra for Y_2O_3 ceramics (Fig. 23.4). The spectra were in good agreement with our previous results [12]. For all the samples under

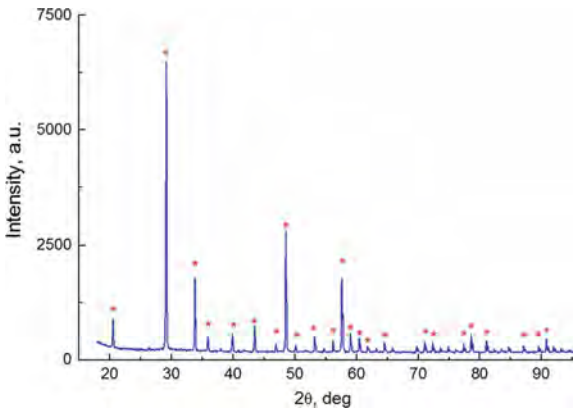

Fig. 23.3 XRD pattern of Y_2O_3 ceramics

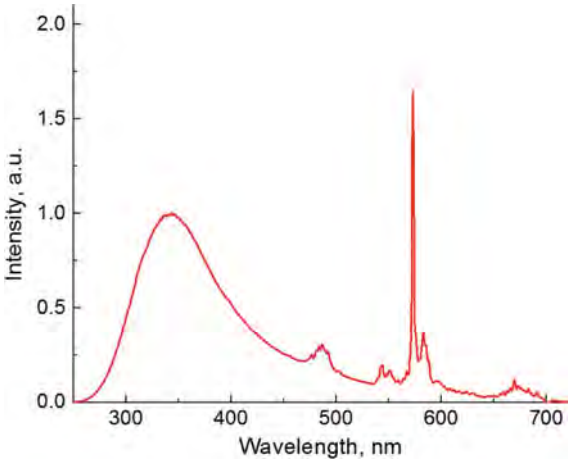

Fig. 23.4 Typical luminescence spectrum of Y_2O_3 ceramics

study the shapes of the spectra were similar. The most pronounced wide band was observed in the UV range with maximum at 350 nm. The maximum amount of light emission is integrally concentrated at this wavelength band. As we mentioned above, intense luminescence at a given wavelength range is often associated with emission of STE decay [2, 14–16].

We found that prolonged X-ray exposure caused a change of 350 nm peak intensity. Figure 23.5 shows the typical time evolution of the peak intensity (dose dependence) for Y_2O_3 ceramics.

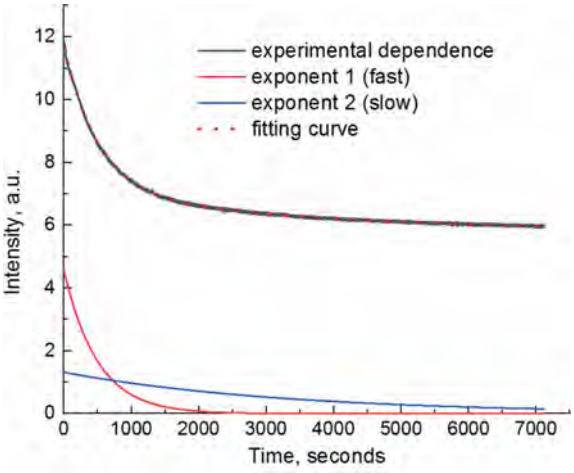

Fig. 23.5 The experimental time evolution of Y_2O_3 luminescent intensity at 350 nm and the result of exponential fitting (we also show the fast and slow exponents of the fitting curve for visualization)

It is well known that the process of relaxation of STE in a substance occurs in three ways. The first one is the excitation of a luminescent center, which is subsequently de-excited by light emission. The second way is de-excitation of the defect, which leads to its annealing. The third one is subthreshold formation of a defect due to the breaking of the bond in the lattice between neighboring atoms and the subsequent displacement of atoms by a distance, which does not allow restoring this bond. It should be noted that STE can migrate along the lattice at many atomic distances, and the probability of its relaxation is significantly higher when the STE encounters the defect [20]. Luminescent light intensity is the result of the instantaneous dynamic equilibrium of the above mentioned processes.

As it can be seen from Fig. 23.5, the decrease of intensity curve means that with increasing exposure time, nonradiative processes prevail over the radiative exciton decay. However, during long-term irradiation a balance between competing nonradiative and radiative processes is set in the substance. Herewith, the radiation intensity becomes almost two times less than its initial value. The fitting of experimental curves was carried out. It turned out that the most accurate result was obtained for experimental curve fitting by the sum of two exponents (fast and slow) in the following form (see Fig. 23.5):

$$I = I_0 + A_1 \mathrm{e}^{-\frac{t}{t_1}} + A_2 \mathrm{e}^{-\frac{t}{t_2}}.$$

The curve had two intervals of the rate of intensity change. The first interval is a high rate of intensity change; the second is a large exposure time and a slow decrease. As can be seen, the time dependence is determined by two processes characterized by significantly different times. The first one is fast process having characteristic time of several hundred seconds, namely $t_1 \approx 500$ s, while the second slow process has a characteristic parameter 5–6 times longer than the first, approximately $t_2 \approx 3300$ s.

As far as time dependence had two components, it is reasonable to assume that a decrease in the X-ray luminescent intensity is determined by two processes that contribute to the total light emission in a given wavelength region. As the X-ray irradiation dose increases, both of these processes, having different dynamic characteristics of luminescence, affect the overall balance of the emission processes in different ways. At the initial moments of irradiation ($t < 500$ s), the fast process prevails, manifesting itself in the rapidly decaying exponential dependence of the light emission. Beginning from the time of 1500 s, the role of the second mechanism in the overall balance of the light emission greatly increases.

The time evolution of luminescent intensity at a wavelength of 350 nm was also studied upon repeated irradiation of the sample with long time interval between exposures (Fig. 23.6). Cyclic irradiation (total irradiation for each sample consisted of 3 cycles, the cycle time was 7200 s and the interval between exposures was 24 h) of the same sample showed that during the absence of irradiation a significant regeneration of the luminescent intensity occurred. It was observed that after pause of 24 h from the previous irradiation, the initial value of the luminescent intensity was significantly higher than the value measured at the end of the previous cycle. At

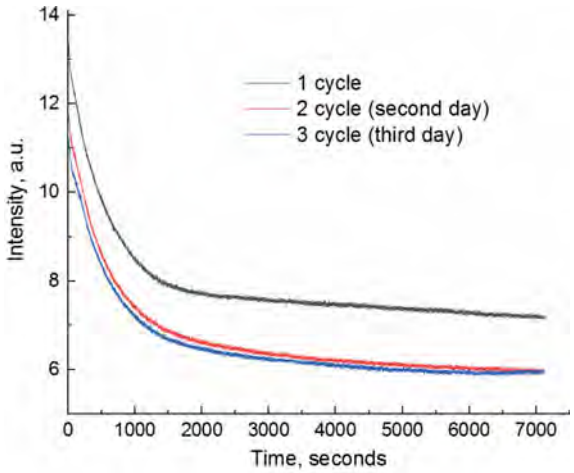

Fig. 23.6 The total time evolution of Y_2O_3 luminescent intensity at 350 nm for cyclic irradiation

the same time, the initial intensity of luminescence for each next irradiation cycle was somewhat less than one for the previous cycle. In addition, the intensity of the luminescence tended to a certain saturated value at the end of each irradiation cycle. As can be seen from Fig. 23.6, for the second and third irradiation cycles the saturated values of intensities at the end of irradiation are very close.

It should be noted that the tendency of two-exponential decrease in the time dependence has always been fulfilled for all irradiation cycles. The time constant of the fast process (first exponent) increased slightly with each subsequent irradiation cycle. The second time constant of the slow process (second exponent) remained unchanged.

An analysis of the time dependence of the luminescent intensity during cyclic irradiation allows us to conclude that there are several types of defects and their balance in the sample. As we mentioned above light generation is associated with STE decay in this wavelength region, so the following scenario of defect balance can be considered. Three types of defects are involved in the dynamics of luminescence.

The first type is a defect that is not annealed during one cycle of exposure to X-ray radiation. Figure 23.6 shows that such defects can be at least half of the total amount of defects that contribute to light emission. But on the other hand it is possible that they can be modified into a defect of other type, which will be annealed during the next irradiation cycle.

The second type is a defect, which is annealed under the influence of X-ray due to a change in the position of the atom and bond reduction with the neighboring atom or a change in the charge state. This bond is maintained during exposure to X-rays. However, after the irradiation termination the influence of thermal vibrations of the lattice leads to breakage of the bonds and finally the defects will be restored (the number of the defects will be the same as before exposure). During subsequent irradiation (next cycle) these defect will again be a source of light radiation for some

time until its annealing is repeated. It is precisely this fact that explains the decrease in the intensity of light emission during prolonged X-ray irradiation.

We attribute the third type of defects with one that is finally annealed after the influence of X-ray radiation. As a result of the annealing process, stable bonds are formed and subsequently these defects do not participate in luminescence processes. The portion of these defects can be defined as the difference between the intensities of light radiation in different irradiation cycles at the initial moments of time or after prolonged exposure, when the intensity of light radiation has stabilized (see the difference between intensities for the first cycle and both the second and the third cycles at the beginning of irradiation $t = 0$ on Fig. 23.6; also see the difference at the end of irradiation $t = 7200$ s).

For a more detailed determination of the nature of various types of defects, as well as their evolution under the influence of X-ray radiation and temperature, additional studies are necessary.

23.4 Conclusions

As a result of long-term X-ray irradiation of Y_2O_3 ceramics sintered from nano-sized powder, the evident decrease (almost double) in the intensity of luminescent radiation at 350 nm occurred. This band is often associated with light emission through STE decay. It was found that the time dependence of the luminescence intensity was good fitted by exponential functions and therefore can be characterized by two processes: fast with a time constant of about 500 s and slow with a time constant of about 3000 s. It was observed that if the sample was exposed to X-ray reirradiation after 24 h pause, then the initial luminescence intensity would considerably exceed the value measured at the end of the previous irradiation. That is, it can be argued that a regeneration of the luminescence centers responsible for light emission at this band occurred during the interval between exposures. As a result of long-time cyclic irradiation, the luminescence intensity approached a saturation value at the end of each cycle, and finally the saturation values for the second and third cycles became practically the same. An analysis of the time evolution of Y_2O_3 luminescence at the wavelength of 350 nm during cyclic irradiation allows us to conclude that several types of defects are involved in the dynamics of light generation.

Acknowledgements We thank to the staff of protecting coating and ceramic laboratory for preparing and sintering the ceramics. We are also grateful S. Bogatyrenko for electron microscope images of the samples.

References

1. A. Fukabori et al., J. Cryst. Gr. **318**, 823 (2011). https://doi.org/10.1016/j.jcrysgro.2010.10.211
2. A. Fukabori et al., J. of Appl. Phys. **107**, 073501 (2010). https://doi.org/10.1063/1.3330407
3. G.V. Lyamina et al., Nanotechnol. Russ. **13**(5–6), 337 (2018). https://doi.org/10.1134/S1995078018030102
4. D.H. Chavez, K. Juarez-Moreno, G.A. Hirata, Nanobiomedicine **3**, 1 (2016). https://doi.org/10.5772/62252
5. J. Shruthia, N. Jayababua, P. Ghosalb, M. V. Ramana Reddy, Ceram. Int. **45**(17) (2019). https://doi.org/10.1016/j.ceramint.2019.07.141
6. N.J. Shivaramu, B.N. Lakshminarasappa, K.R. Nagabhushana, F. Singh, Rad. Meas. **71**, 518 (2014). https://doi.org/10.1016/j.radmeas.2014.03.027
7. O.M. Bordun, I.M. Bordun, J. Appl. Spectr. **64**, 361 (1997). https://doi.org/10.1007/BF02675099
8. V.V. Osipov, A.V. Rasuleva, V.I. Solomonov, Opt. Spectr. **105**, 524 (2008). https://doi.org/10.1134/S0030400X08100068
9. O.M. Bordun, I.M. Bordun, S.S. Novosad, J. Appl. Spectr. **62**, 1060 (1995) https://doi.org/10.1007/BF02606760
10. O.M. Bordun, J. Appl. Spectr. **69**, 430 (2002). https://doi.org/10.1023/A:1019763518857
11. O.M. Bordun, J. Appl. Spectr. **68**, 304 (2001). https://doi.org/10.1023/A:1019228505728
12. S. Kononenko et al., in *Paper presented at the 8th IEEE International Conference on "Nanomaterials: Applications & Properties"*, Odessa, September 2018
13. G. Blasse, L.H. Brixner, Eur. J. Solid State Inorg. Chem. **28**, 767 (1991). https://doi.org/10.1002/chin.199136016
14. A. Lushchik et al., J. Lumin. **232**, 87–89 (2000). https://doi.org/10.1016/S0022-2313(99)00271-9
15. N. V. Guerassimova et al., HASYLAB Annu. Rep. **603** (2005)
16. S.S. Novosad et al., Acta Phys. Polonica A **133**, 806 (2018) https://doi.org/10.12693/APhysPolA.133.806
17. A. Fukabori et al., Ceram. Int. **38**, 2119 (2012). https://doi.org/10.1016/j.ceramint.2011.10.052
18. I.N. Stanton et al., Nanoscale **6**, 5284 (2014). https://doi.org/10.1039/c4nr00497c
19. L. Robindro Singh, Nanotechnology **19**, 1 (2008). https://doi.org/10.1088/0957-4484/19/05/055201
20. L.H. Abu-Hassan, P.D. Townsend, R.P. Webb, Nucl. Instr. Meth. Phys. Res. B **19–20**, 927 (1987). https://doi.org/10.1016/S0168-583X(87)80186-6

Chapter 24
Electrochemical Formation of 'Synthetic Receptors' Based on Conducting Polymers

A. Ramanavicius, A. Tereshchenko, I. Plikusiene, V. Ratautaite, M. A. Deshmukh, V. Smyntyna, Ya. Oztekin, U. Bubniene, and A. Ramanaviciene

Abstract Analysis of pharmaceuticals and biologically active materials recently can be performed by biosensors, which can be based on conducting polymers. Therefore, in this Mini Review some achievements in the synthesis and application of conducting polymer—polypyrrole (Ppy), which is often used in the design of sensors and biosensors, are overviewed. Some perspective methods of conducting polymer synthesis are outlined. Significant attention has been paid to electrochemical, chemical and biochemical synthesis of conducting polymers (CPs) , which were developed by authors. The applicability of polypyrrole based functional layers in the design of electrochemical biosensors is overviewed. The adaptability of enzyme—glucose oxidase (GOx), which can be applied as (i) biological recognition element—in the design of glucose biosensors, (ii) a biocatalyst—in the synthesis of some above mentioned conducting polymers, is discussed. Part of biocompatibility related

A. Ramanavicius (✉) · A. Tereshchenko · I. Plikusiene · V. Ratautaite · M. A. Deshmukh · Ya. Oztekin · U. Bubniene
Department of Physical Chemistry, Faculty of Chemistry and Geosciences, Vilnius University, Vilnius, Lithuania
e-mail: arunas.ramanavicius@chf.vu.lt

A. Ramanavicius · I. Plikusiene · V. Ratautaite · U. Bubniene
Laboratory of Nanotechnology, State Research Institute Center for Physical Sciences and Technology, Vilnius, Lithuania

A. Tereshchenko · M. A. Deshmukh · Ya. Oztekin · A. Ramanaviciene
Faculty of Chemistry and Geosciences, NanoTechnas - Centre of Nanotechnology and Material Science, Vilnius University, Vilnius, Lithuania

A. Tereshchenko · V. Smyntyna
Department of Experimental Physics, Faculty of Mathematics, Physics and Information Technologies, Odesa I.I. Mechnikov National University, Odesa, Ukraine

M. A. Deshmukh
Department of Physics, RUSA - Center for Advanced Sensor Technology, Dr. Babasaheb Ambedkar Marathwada University, Aurangabad, Maharashtra 431 004, India

Ya. Oztekin
Faculty of Science, Department of Chemistry, Selcuk University, Konya, Turkey

A. D. Pogrebnjak et al. (eds.), *Nanomaterials in Biomedical Application and Biosensors (NAP-2019)*, Springer Proceedings in Physics 244,
https://doi.org/10.1007/978-981-15-3996-1_24

aspects of some conducting polymers are also discussed and some insights in the application of polypyrrole-based coatings for implantable sensors are outlined.

24.1 Introduction

Demands for advanced pharmaceutical and biomedical analysis are evolving very rapidly. Therefore, various new and advanced technologies based on sensors and biosensors [1] are finding the application in the solution of challenging problems of pharmaceutical and biomedical analysis [2]. Various polymer-based nanomaterials recently are applied in the design of sensors and biosensors in order to advance their sensitivity and selectivity and in this way to extend their bioanalytical applicability [3, 4]. It should be noted that conducting polymers are among the most promising materials, which can extend analytical characteristics of sensors [5–7], including their sensitivity and selectivity [8]. These achievements are possible due to electrical conductivity, electrochemical activity, mechanical elasticity and environmental stability of conducting polymers [9–11]. In addition, unique capabilities of transferring electric charge from biological objects towards electrodes are also very attractive property for sensorics related application of conducting polymers [12]. Simple doping and dedoping of conducting polymers enables to manipulate the properties of material makes conducting polymer ideal material for sensing applications [13, 14]. Among a variety of conducting polymers polypyrrole (Ppy), polyaniline (PANI) and polythiophene (PTH) are of the greatest interest due to their high technological potential, which has been exploited in the design of super capacitors [15], rechargeable batteries [16], corrosion prevention [17], sensors [18, 19] solar cells [20] and biosensors [21]. Technologically it is advantageous that various conducting polymer based nanocomposites with entrapped enzymes [22], receptor-like proteins [13], antibodies [23] and DNA [24] can be formed by different methods overviewed and discussed in this review. Therefore, such conducting polymer based composite materials can show unique sensing properties, which are determined by entrapped materials and dopants.

The aim of this ‘Mini Review’ is to evaluate the methods of synthesis and bioanalytical application of some conjugated polymers including polypyrrole, polythiophene and polyaniline.

24.2 Synthesis of Conducting Polymers

24.2.1 Synthesis of Conducting Polymers

It was demonstrated that conducting polymers might be produced by chemical [25], electrochemical [13, 26] and even by biotechnological approaches [3].

Therefore, these conducting polymers synthesis methods are taken for consideration in this review.

Chemical synthesis is one of the most popular methods to form conducting polymers. This method is relatively cheap and simple based on usage of strong oxidators such as $FeCl_3$ or H_2O_2 [17, 27]. Spherical particles of polypyrrole can be formed using H_2O_2, which has oxidation potential sufficient to initiate the polymerization of pyrrole and other monomers that are forming conducting polymer [28], this method is very attractive because excess of H_2O_2 can be easily degraded into H_2O and O_2, therefore pure particles of the conducting polymer can be formed, which possesses a good biocompatibility with living stem cells [29, 30] and even when injected in mice peritoneum [31].

The advantage of chemical synthesis is that using this method can be formed large quantities of nanoparticles, based on the conducting polymer, which are suspended in a solution. During the next technological steps these nanoparticles eventually can be modified and applied for biomedical purposes. However, this method is not always well suited for the formation of films, because chemically formed conducting polymer layers mostly are sparse and not stable enough for further technological applications.

Some authors presented in their work where polypyrrole nanostructures such as nanowires and nanotubes were chemically synthesized inside aluminium template [32]. The response surface methodology based on central composite design was used to determine the relationship between the morphology of the nanostructures (nanowires or nanotubes) and synthesis conditions [32]. Other authors showed that polypyrrole nanostructures can be gained chemically synthesizing Ppy within the pores of microporous and nanoporous particle track-etched membranes [33]. Chemical synthesis of polypyrrole nanoparticles is possible using facile one-step chemical oxidative polymerization method at room temperature. Using this method doping of conjugated-polypyrrole nanoparticles into electrically conductive adhesives (ECAs) can be obtained. The purpose of such polymerization procedure is to prepare low-electrical resistivity interconnecting materials [34].

Biochemical synthesis of conducting polymers can be performed in several ways: (i) enzymatic—using redox enzymes, e.g. glucose oxidase or (ii) microbiological—using whole microorganisms [35, 36].

Enzymatic synthesis of conducing polymers. Catalytic reactions of Glucose oxidase (GOx) E.C. 1.1.3.4. from *Penicillium vitale* can be applied for the synthesis of various conducting polymers such as: polypyrrole [3, 13, 28, 29], polyaniline [37] and polytiophene [38], polyphenanthroline [39] and some other conducting polymer based layers and nanoparticles. This is a unique approach, which is based on catalytic action of GOx. Actually polymerization of monomers, which are forming conducting polymer, is initiated by hydrogen peroxide that is formed during the catalytic action of GOx. Immobilized and in water dissolved enzymes have been successfully applied in the enzymatic synthesis of conducting polymer based layers or particles with entrapped enzymes, which are producing hydrogen peroxide. Due to remaining activity of entrapped enzyme, such particles and layers are well suitable for the creation of amperometric glucose biosensors and biofuel cells.

Microbiological synthesis of polypyrrole. Some redox processes, which are part of metabolism occurring in living cells can be adapted for the synthesis of Ppy within cell wall of living cells: yeast cells [22].

Electrochemical synthesis is also very attractive method used for the deposition of conducting polymer based layers. The adjustment of various electrochemistry-related parameters such as polymerization-inducing potential, current, scan rate and polymerization duration enables to create polymeric layers of different characteristics [13, 40, 41]. This method enables to manipulate properties of conducting polymers for particular application by controlling the process parameters [42]. In addition, electrical conductivity and some electrochemical properties of conducting polymers can be tailored and controlled by variation of polymerizable monomer concentrations, pH of polymerization bulk solution and different dopant concentrations [43–45]. Electrochemical formation of conducting polymer based layers is attractive because both morphology and thickness of formed layer can be controlled by the adjustment of (i) potential-profile and the duration of potential pulses or (ii) potential sweep rate [13], pH of the electrolyte [46].

24.2.2 Some Chemical and Physical Properties of Conducting Polymers

In our researches we have determined that conducting polymer—polypyrrole—exhibit unique electrochemical, affinity [32] and/or optical [33] properties. Therefore, changes of one or more of these physicochemical properties (e.g. resistance of CP-based biological recognition layer, variation of electrical capacitance, changes of optical properties etc.) can be determined by particular signal transducer and can be precisely monitored by registration device. It should be noted that among number of CPs—polypyrrole mostly has been used in the design of enzymatic biosensors as enzyme immobilization matrixes [3].

24.3 Conducting Polymers for Biosensor Design

Conducting polymers in the design of amperometric biosensors. Due to relatively low permeability of Ppy layer for substrates and reaction products, apparent Michaelis constant (K_{Mapp}) of immobilized enzymes increases significantly. This effect enables to extend linear range of such enzymatic sensors [14], which can be used for biosensors based on enzymes, which have low K_{Mapp} and therefore are not suitable for the investigation of samples with high substrate concentration, e.g. glucose concentration in blood is significantly higher in comparison with K_{Mapp} of the most popular glucose oxidases [34]. This methodology enables to tune analytical characteristic such as lower and upper limits of detection and linear range of

biosensor [3, 23, 24]. In addition to the above mentioned properties, some conducting polymers are capable to transfer charge directly from redox enzymes towards electrodes [39]. Therefore, electrochemically generated conducting polymers are very promising as advanced immobilization matrixes of amperometric catalytic biosensors [14] biofuel cells and other bioelectronic devices [3, 47–49]. However, most of enzymes have redox centers deeply buried within protein 'shell'. Therefore, charge transfer from these enzymes is complicated even if they are entrapped within conducting polymer. In order to solve this problem in some of our researches we have demonstrated that charge transfer capabilities of electrochemically formed conducting polymers can be improved by grafting to the surface of carbon-based electrodes [39]. Glucose biosensors, which are mostly based on GOx, are important tools, which are used not only for biomedical purposes, but also as a model system in the development of enzymatic sensors. Therefore, very different conducting polymer and GOx based structures have been formed and applied in glucose sensor design [14, 50]. Single-step procedure has been established for the modification of electrode by composite material consisting of polypyrrole, Prussian blue (PB) and glucose oxidase (GOx) [31].

Conducting polymers in the design of affinity biosensors can serve as (i) immobilization matrixes [13, 31], signal transduction systems [13, 39] and even analyte recognizing components [28]. Electrochemically deposited layers of conducting polymers modified with entrapped proteins (antibodies or antigens) have been applied in the design of various types of ***immunosensors*** [13], in such sensors conducting polymer layer is enhancing potentiodynamically generated electrochemical signal [13] or reducing the influence of interfering materials if photoluminescence based analytical signal is registered [51]. The most promising among affinity sensors are ***molecularly imprinted polymers (MIPs) based sensors***, because they do not need very expensive biological recognition materials [52–54]. Overoxidized polypyrrole seems to be one of the most promising among all MIPs because it can be prepared in very simple electrochemical way using single polymerizable monomer. Polypyrrole can be easily imprinted by large [28, 29, 55–57] and low [7, 10, 58, 59] molecular weight molecules (e.g. by Caffeine [10], theophylline [58], L-aspartic acid [59] and histamine [7]) and even by large molecular weight biomolecules (e.g. by DNA and proteins [28, 29, 55–57]).

24.4 Conclusions

Conducting polymers have found application in various sensors and biosensors, which can be used in the analysis of pharmaceuticals and biologically active materials. Electrochemical synthesis of conducting polymers seems promising, because it can be controlled by adjustment of electrical current profile. Characteristics of conducting polymer based sensors are determined by the thickness of polypyrrole layer. Enzymatic and microbial synthesis of polypyrrole demonstrated that in such way formed polypyrrole/bio-composite materials are also suitable for the

development of biosensors and biofuel cells. Also chemical synthesis of polypyrole reveal possibilities to form different nanostructures that can be used as biosensing platforms. The applicability of similar methods for the synthesis of other conducting polymers such as polyaniline, polythiophene, and some others conducting or π-π conjugated polymers is predicted.

Acknowledgements This research was supported by Ukrainian-Lithuanian Research project Lithuanian Research Council project No. P-LU-18-53.

References

1. N.K. Bakirhan, G. Ozcelikay, S.A. Ozkan, J. Pharm. Biomed. Anal. **159**, 406 (2018)
2. A. Sankiewicz, L. Romanowicz, M. Pyc, A. Hermanowicz, E. Gorodkiewicz, J. Pharm. Biomed. Anal. **150**, 1 (2018)
3. N. Aydemir, J. Malmström, J.T. Sejdic, Phys. Chem. Chem. Phys. **18**, 8264–8277 (2016)
4. J.-M. Moon, N. Thapliyal, K.K. Hussain, R.N. Goyal, Y.-B. Shim, Biosens. Biolect. **102**, 540–552 (2018)
5. A. Ramanavicius, A. Kausaite, A. Ramanaviciene, Analyst **133**, 1083 (2008)
6. K.C. Persaud, Mater. Today **8**, 38–44 (2005)
7. V. Ratautaite, M. Nesladek, A. Ramanaviciene, I. Baleviciute, A. Ramanavicius, Electroanalysis **26**, 2458 (2014)
8. I. Baleviciute, V. Ratautaite, A. Ramanaviciene, Z. Balevicius, J. Broeders, D. Croux, M. McDonald, F. Vahidpour, R. Thoelen, W. De Ceuninck, K. Haenen, M. Nesladek, A. Reza, A. Ramanavicius, Synth. Met. **209**, 206–211 (2015)
9. V. Ratautaite, A. Ramanaviciene, Y. Oztekin, J. Voronovic, Z. Balevicius, L. Mikoliunaite, A. Ramanavicius, Colloids Surf. A **418**, 16 (2013)
10. M. Tomczykowa, M.E.P. Brzezinska, Polymers **11**, 350 (2019)
11. H. Yoon, Nanomaterials **3**, 524–549 (2013)
12. Y. Oztekin, A. Ramanaviciene, Z. Yazicigil, A.O. Solak, A. Ramanavicius, Biosens. Bioelectron. **26**, 2541 (2011)
13. Z. Ma, W. Shi, K. Yan, L. Pan, G. Yu, Chem. Science **25**, 6232–6244 (2019)
14. N. Karaoğlan, C. Bindal, Eng. Sci. Technol. Int. J. **21**, 1152–1158 (2018)
15. Y. Wang, Y. Chen, Y. Liu, W. Liu, P. Zhao, Y. Li, Y. Dong, H. Wang, J. Yang, Electrochim. Acta **295**, 989 (2019)
16. Z. Zhao, T. Yu, Y. Miao, X. Zhao, Electrochim. Acta **270**, 30 (2018)
17. J.O. Iroh, W. Su, Electrochim. Acta **46**, 15 (2000)
18. V. Ratautaite, D. Plausinaitis, I. Baleviciute, L. Mikoliunaite, A. Ramanaviciene, A. Ramanavicius, Sens. Actuators B: Chem. **212**, 63 (2015)
19. M. Holguín, O.E.R. Álvarez, C.A. Arizabaleta, W. Torres, Comput. Theor. Chem. **1147**, 29 (2019)
20. N. Sangiorgi, A. Sangiorgi, F. Tarterini, A. Sanson, Electrochim. Acta **305**, 322 (2019)
21. A. Ramanavicius, Y. Oztekin, A. Ramanaviciene, Sens. Actuators B **197**, 237 (2014)
22. N. German, A. Ramanavicius, J. Voronovic, A. Ramanaviciene, Colloids Surf. A **413**, 224 (2012)
23. F.S. Felix, L. Angnes, Biosens. Bioelectron. **102**, 470 (2018)
24. A. Ramanaviciene, A. Ramanavicius, Anal. Bioanal. Chem. **379**, 287 (2004)
25. K. Leonavicius, A. Ramanaviciene, A. Ramanavicius, Polymerization model for hydrogen peroxide initiated synthesis of polypyrrole nanoparticles. Langmuir **17**, 10970 (2011)
26. V. Syritski, J. Reut, A. Öpik, K. Idla, Synth. Metals **102**, 1326 (1999)

27. N.Y. Abu-Thabit, J. Chem. Educ. **939**, 1606–1611 (2016)
28. E. Falletta, C. Della Pina, M. Rossi, J. Adv. Cata. Sci. Technol. **1**, 6–14 (2014)
29. A. Vaitkuviene, V. Kaseta, J. Voronovic, G. Ramanauskaite, G. Biziuleviciene, A. Ramanaviciene, A. Ramanavicius, J. Hazard. Mater. **250–251**, 167 (2013)
30. A. Vaitkuviene, V. Ratautaite, L. Mikoliunaite, V. Kaseta, G. Ramanauskaite, G. Biziuleviciene, A. Ramanaviciene, A. Ramanavicius, Coll. Surf. A **442**, 152 (2014)
31. A. Ramanaviciene, A. Kausaite, S. Tautkus, A. Ramanavicius, J. Pharm. Pharmacol. **59**, 311 (2007)
32. V. Ratautaite, S.N. Topkaya, L. Mikoliunaite, M. Ozsoz, Y. Oztekin, A. Ramanaviciene, A. Ramanavicius, Electroanalysis **25**, 1169 (2013)
33. A. Ramanavicius, N. Ryskevic, A. Kausaite-Minkstimiene, U. Bubniene, I. Baleviciute, Y. Oztekin, A. Ramanaviciene, Sens. Actuators B: Chem. **171–172**, 753 (2012)
34. N. German, A. Kausaite-Minkstimiene, A. Ramanavicius, T. Semashko, R. Mikhailova, A. Ramanaviciene, Electrochim. Acta **169**, 326 (2015)
35. A. Kisieliute, A. Popov, R.M. Apetrei, G. Cârâc, I. Morkvenaite-Vilkonciene, A. Ramanaviciene, A. Ramanavicius, Eng. J. **356**, 1014 (2019)
36. A. Ramanavicius, E. Andriukonis, A. Stirke, L. Mikoliunaite, Z. Balevicius, A. Ramanaviciene, Enzyme Microb. Technol. **83**, 40 (2016)
37. A. German, A. Popov, A. Ramanaviciene, A. Ramanavicius, Polymer **115**, 211 (2017)
38. V. Krikstolaityte, J. Kuliesius, A. Ramanaviciene, L. Mikoliunaite, A. Kausaite-Minkstimiene, Y. Oztekin, A. Ramanavicius, Polymer **55**, 1613 (2014)
39. S.J. Park, C.S. Park, H. Yoon, Polymers **9**, 155 (2017)
40. R. Xiao, S.I. Cho, R. Liu, S.B. Lee, J. Am. Chem. Soc. **129**, 4483–4489 (2007)
41. D.E. Labaye, C. Jérôme, V.M. Geskin, P. Louette, R. Lazzaroni, L. Martinot, R. Jérôme, Langmuir **18**, 5222–5230 (2002)
42. Y. Long, M. Mengli, C. Gu, M. Wan, J.L. Duvail, Z. Liu, Z. Fan, Prog. Polym. Sci. **36**, 1415 (2011)
43. M.A. Rahman, P. Kumar, D. Park, Y. Shim, Sensors **8**, 118 (2008)
44. B. Luc, G. Street, Acc. Chem. Res. **18**, 309 (1985)
45. S. Srilalitha, K. Jayaveera, S. Madhvendhra, Int. J. Innov. Res. Sci. Eng. Technol. **2**, 2694 (2013)
46. T.H. Le, Y. Kim, H. Yoon, Polymers **9**, 150 (2017)
47. S. Ghosh, T. Maiyalagan, R.N. Basu, Nanoscale **8**, 6921–6947 (2016)
48. Beenish, Inamuddin, M.I. Ahamed, A.M. Asiri, K.A. Al Amry, Mater. Sci. Energy Technol. **1**, 63–69 (2018)
49. I. Inamuddin, K.M. Shin, S.I. Kim, I. So, Electrochim. Acta **54**, 3979–3983 (2009)
50. A. Ramanavicius, A.I. Rekertaitė, R. Valiūnas, A. Valiūnienė, Sens. Actuators B: Chem. **240**, 220 (2017)
51. A. Ramanavicius, N. Ryskevic, Y. Oztekin, A. Kausaite-Minkstimiene, S. Jursenas, J. Baniukevic, J. Kirlyte, U. Bubniene, A. Ramanaviciene, Anal. Bioanal. Chem. **398**, 3105 (2010)
52. G. Zhang, Y. Yu, M. Guo, B. Lin, L. Zhang, Sens. Actuators B: Chem. **288**, 564 (2019)
53. A. Tretjakov, V. Syritski, J. Reut, R. Boroznjak, O. Volobujeva, A. Öpik, Microchim. Acta **180**, 1433 (2013)
54. A. Menaker, V. Syritski, J. Reut, A. Öpik, V. Horváth, R.E. Gyurcsányi, Adv. Mater. **21**, 2271 (2009)
55. A. Ramanaviciene, A. Ramanavicius, Biosens. Bioelectron. **20**, 1076 (2004)
56. Z.D. Kojabad, S.A. Shojaosadati, Mater. Des. **96**, 378 (2016)
57. J. Duchet, R. Legras, S. Demoustier-Champagne, Synth. Met. **2**, 113 (1998)
58. V. Ratautaite, S.D. Janssens, K. Haenen, M. Nesládek, A. Ramanaviciene, I. Baleviciute, A. Ramanavicius, Electrochim. Acta **130**, 361 (2014)
59. V. Syritski, J. Reut, A. Menaker, R.E. Gyurcsányi, A. Öpik, Electrochim. Acta **53**, 2729 (2008)

Chapter 25
Optical Immunosensor Based on Photoluminescent TiO_2 Nanostructures for Determination of Bovine Leucosis Proteins. Model of Interaction Mechanism

A. Tereshchenko, V. Smyntyna, U. Bubniene, and A. Ramanavicius

Abstract The main aspects of the interaction mechanism between nanostructured TiO_2 layer and BLV proteins *gp*51 have been evaluated during the formation of photoluminescence-based immunosensor. *Bovine leucosis* protein *gp*51 was adsorbed on the surface of a nanostructured TiO_2 thin film, formed on glass substrates. A photoluminescence (PL) peak shift from 517 to 499 nm was observed after modification of TiO_2 surface by adsorbed *gp*51 (i.e. formation of the biosensitive layer *gp*51/TiO_2). An incubation of *gp*51/TiO_2 in a solution containing anti-*gp*51 antibodies resulted in the formation a of a new structure (anti-*gp*51/*gp*51/TiO_2) and the backward PL peak shift from 499 nm to 516 nm. The PL shifts are attributed to the variations in the self-trapped exciton energy level, which were induced by the changes of electrostatic interaction between positively charged atoms and groups, provided by the adsorbed *gp*51 protein and negatively charged surface of TiO_2. The charge–charge-based interaction in the double charged layers *gp*51/TiO_2 can also be interpreted as a model based on 'imaginary capacitor', formed as a result of the electrostatic interaction between oppositely charged protein *gp*51 layer and the TiO_2 surface.

25.1 Introduction

Bovine leucosis is a lethal cancerous disease caused by *Bovine leukemia* virus (BLV) that belongs to one of the most monitored family of retro-viruses in the world. There is a significant risk that BLV can infect other mammalians like it was in the case

A. Tereshchenko (✉) · V. Smyntyna
Department of Experimental Physics, Faculty of Mathematics, Physics and Information Technologies, Odesa I.I. Mechnikov National University, Odesa, Ukraine
e-mail: alla_teresc@onu.edu.ua

A. Tereshchenko · U. Bubniene · A. Ramanavicius
Department of Physical Chemistry, Faculty of Chemistry and Geosciences, Vilnius University, Vilnius, Lithuania

A. D. Pogrebnjak et al. (eds.), *Nanomaterials in Biomedical Application and Biosensors (NAP-2019)*, Springer Proceedings in Physics 244,
https://doi.org/10.1007/978-981-15-3996-1_25

of Human immunodeficiency virus (HIV). Due to lethal epidemical nature, the outbreaks of *Bovine leucosis* pose a great threat to the environment and eco-systems. As the food quality control is an inseparable part of human safety and wellbeing thus an advanced determination of *Bovine leucosis* can decrease the risks of human diseases caused by this and other dangerous viruses. For this reason, timely diagnosis of virus-induced diseases is an important direction in environmental monitoring. For such monitoring very efficient bio-analytical systems are required but old bio-analytical methods are cumbersome and slow. Therefore, the development of advanced bioanalytical systems based on photoluminescence immunosensors seems to be the most promising direction [1, 2]. However, despite of many reports on photoluminescence-based immunosensors, the mechanism of interaction of biomolecules with semiconducting materials, which are used as analytical signal transducers in the most promising PL-based immunosensors, is still very poorly evaluated [3].

Nanostructured Titanium dioxide (TiO_2) is known as a material of intense photoluminescence at room temperature [4, 5]. The application of TiO_2 photoluminescence properties in optical biosensors and immunosensors have been reported in the range of works [1–3]. TiO_2 is widely studied material as a wide-band gap semiconductor with a great combination of physical and chemical properties [6–8]. A good biocompatibility of TiO_2 nanostructures, their applicability at physiological pHs in the range of 5.5–7.0, non-toxicity and excellent chemical stability have resulted in the extensive application of TiO_2 in various biosensors [1, 2, 9]. Optical biosensors are increasingly studied class of biosensors because optical detection methods have a number of advantages. Optical methods allows to evaluate some inter-molecular interactions contactless, i.e., without contamination and/or deterioration of the aliquot, which contains biological compounds [2, 3] and it allows to avoid application of special tags or markers and enables to determinate the analyte concentration directly without any chemical/physical labels [1–3]. Among the large variety of biosensors, a special attention is paid to the development of immunosensors, based on the specific interaction between antibody and antigen that can be applied for the determination of wide variety of analytes in complex biological samples [1, 2, 9].

The changes in the photoluminescence spectra (shift of photoluminescence maximum and the variation of photoluminescence signal intensity) were exploited as analytical signals for the determination of target analyte [2, 3, 9, 10]. However, the interaction mechanism of proteins with TiO_2 and the origin of the changes in the photoluminescence spectra were not discussed. Although the mechanism of the interaction between semiconductor TiO_2 and proteins is the key in solving many of problems, which are still arising during the development of TiO_2-based immunosensors, such as an improvement of sensitivity and selectivity.

This work is aiming to highlight the origin of the changes in the photoluminescence spectra of TiO_2 resulted after the protein adsorption on its surface during the formation of biosensitive layer, and after the interaction of biosensitive layer with the analyte. The proposed interaction mechanism provides the general understanding of the interaction between TiO_2 and proteins, what is a key in the development of new

PL-immunosensors and solving of many issues related to an improvement of performance of PL-based immunosensors, first of all, related to the sensors' sensitivity and selectivity.

25.2 Experiment Details

Nanostructured TiO_2 layers containing TiO_2 nanoparticles were formed by deposition of colloidal suspension of TiO_2 nanoparticles (Sigma Altrich, 99.7%, particle size of 32 nm) dissolved in ethanol. The concentration TiO_2 nanoparticles was about 0.01 mg/ml. TiO_2 layers were dryed at room temperature and annealed at 350 °C. Structural and surface characterization of the obtained samples showed that TiO_2 layers kept the anatase structure and TiO_2 nanoparticles formed a high surface area porous structure suitable for the formation of biosensitive layer. More detailed information on the deposition and characterization procedures applied for characterization of nanostructured TiO_2 layers is reported in earlier researches [3, 10].

Optical characterization of nanostructured TiO_2 layers was performed by photoluminescence measurements using 355 nm solid state laser as the excitation source. Optical setup is described previous our researches [3, 9]. The spectra were recorded in the range of wavelength from 360 to 800 nm.

The immobilization of biological molecules was carried out by incubation in a solution containing Bovine leukemia virus proteins—*gp*51, similar to the immobilization procedure described in earlier works [3, 9, 10]. In brief: a solution of PBS containing *gp*51 antigens at a high concentration was directly immobilized on the TiO_2 surface. Then the sample was placed into a Petri cup for the incubation in a medium saturated with water vapor at 25 °C. After 10 min of incubation, the surface of the sample was washed with PBS solution in order to remove non-immobilized antigens on the TiO_2 surface. As a result, an adsorption-sensitive layer TiO_2/*gp*51 was formed, selective to the one type of bio-molecules—anti-*gp*51 antibodies against leukemia proteins *gp*51. To prevent a nonspecific interaction (i.e., binding of anti-*gp*51 antibodies directly to unmodified TiO_2 surface), the surface of TiO_2 was further treated with a solution of bovine serum albumin (BSA), which filled possible adsorption sites that remained free after the modification of TiO_2 surface with *gp*51. Thus it is expected that the selectivity of the structure of TiO_2/*gp*51 was improved by this procedure based on treatment with BSA, which is frequently applied during the development of immunosensors devoted for the determination of proteins.

25.3 Results and Discussion

Analysis of the interaction between TiO_2 and *gp*51 proteins was based on the evaluation of photoluminescence of TiO_2 nanoparticles. The protein *gp*51 is specifically binding with antibodies against *gp*51 (anti-*gp*51) that were interpreted as analyte

in this research. The photoluminescence properties of the TiO_2 nanoparticles have been previously investigated by authors in the research papers [3, 9, 10] as well as the influence of *gp*51 protein adsorption on the optical properties of TiO_2 and the development of photoluminescence based immunosensor for the determination of *gp*51 antibodies [3, 9, 10].

The process of immobilization of *gp*51 and formation of TiO_2/*gp*51 structure was similar to that reported in earlier our works [3, 9, 10]. The immobilization of *gp*51 antigens leads to an increase in the intensity of the photoluminescence signal of TiO_2 nanostructures and a UV-shift in the position of the maximum of the photoluminescence spectra (Fig. 25.1). The application of BSA, which were used to block the free adsorption centers on the TiO_2 surface, also leads to a slight increase in the photoluminescence intensity, but the spectrum shift in this case was not observed.

Interaction between TiO_2/*gp*51 and anti-*gp*51 led to the inverse changes in the photoluminescence spectrum (Fig. 25.1), i.e. a decrease in the integral intensity of the photoluminescence and the IR-shift of spectra. Therefore, the response of the immunosensor TiO_2/*gp*51 to anti-*gp*51 can be estimated by two parameters: (i) the photoluminescence intensity and (ii) the position of the PL-maximum. The sensitivity of TiO_2/*gp*51 based immunosensor towards anti-*gp*51 was in the range of 2–8 mkg/ml [9, 10].

TiO_2 (anatase) is known as a semiconductor of n-type conductivity, usually with an 'upward' band bending of the energy levels when closing the surface of TiO_2 (Fig. 25.2) [11], which indicates the accumulation of a negative charge (bound at surface levels) on its surface. The adsorption of the most of molecules is known to

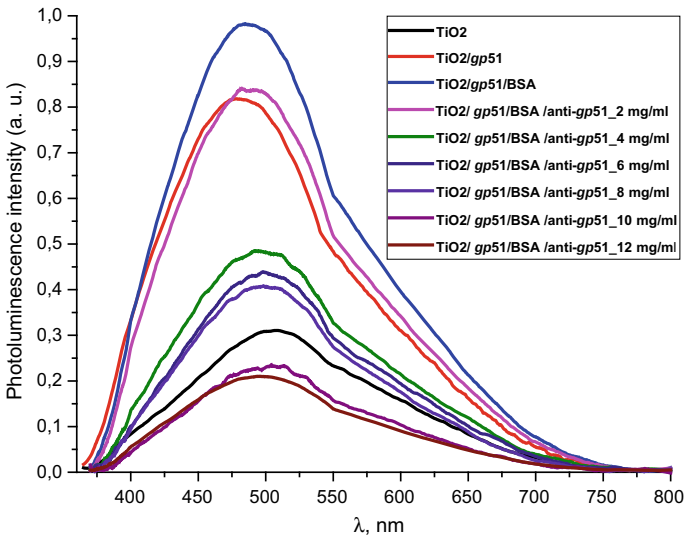

Fig. 25.1 Photoluminescence spectra of TiO_2 nanoparticles before and after the immobilization of *gp*51 antigens on the TiO_2 surface, subsequent BSA deposition and after the interaction of TiO_2/*gp*51 based immunosensor after with analyte (anti-*gp*51 antibodies) of different concentrations

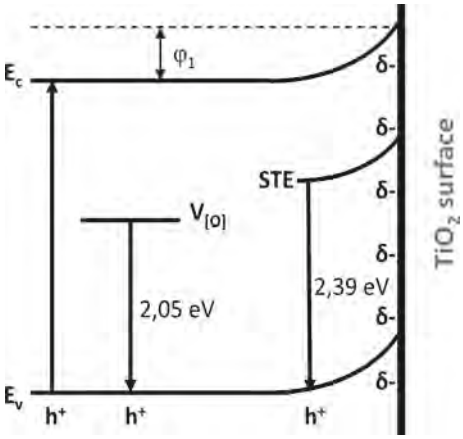

Fig. 25.2 Energetic levels of TiO_2: E_c, E_v—conductive and valence bands respectively, STE—self-trapped exiton level, $V_{[o]}$ —oxygen vacancies level

introduce an additional charge on the solid state surface and it can change the existing surface energy levels or form the additional ones that are involved in the exchange of charges with the volume of a solid material [12].

The proteins consist of amino acids that might contain positively and/or negatively charged radicals that are determining the charge of the different protein domains [13]. A large quantity of negatively charged groups such as aldehyde (–CHO), hydroxyl (–OH), carboxyl (–COOH) and positively charged primary amine ($–NH_2$) and some other groups, which are involved into the structure of amino acids, are responsible for the partial (δ+ and δ−) charges of particular protein domains (Fig. 25.3) [14]. Therefore the proteins are characterized by electrostatic properties, and sometimes even significant electrostatic 'asymmetry of protein molecule' because the atoms

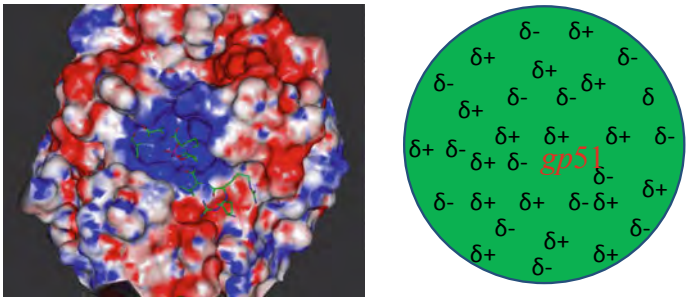

Fig. 25.3 **a** Charge distribution in calciumneurin protein: positive charge—blue color, negative charge—red color, neutral charge—white color [15]; **b** schematic image of charge distribution in *gp*51 antigen protein: δ+ and δ− are partial positive and negative charges respectively

and functional groups forming the protein molecules are charged differently both in their sign and in absolute charge value. Naturally, the charges at least partly are compensating each other, but since the ternary structure of proteins is relatively rigid and the charged groups have only limited degree of freedom to move within the protein globule, therefore in some parts of the protein some uncompensated charge on the surface and inside of the protein still remains [14]. The distribution of charged groups on the surface of the protein depends on the sequence of amino acids, which is pre-determined by the genome that was developed during billions of years lasting evolution and selected genes promoting the synthesis of proteins whose structure the most efficiently matches their function.

It should be taken into account that even if the structure of the most proteins is at some extent 'rigid' there is some degree of flexibility because both secondary and tertiary structures of the protein are supported by a large number of hydrogen bonds but many of them are not very strong [13, 16]. The electrostatic bonds, which are based on Coulomb forces, between the opposite charges, van der Waals forces and disulfide bonds also play an important role in the formation of both secondary and tertiary structures of protein.

25.3.1 Mechanism of Interaction Between TiO_2 and Proteins

A *gp*51 protein molecule has a molecular mass of 51 KDa. The characteristic geometric size of the *gp*51 molecules adsorbed on the TiO_2 surface is about 6 nm in diameter [17]. The authors, which have published a research on the formation of *gp*51 virus based capsid of BLV, have constructed an image of *gp*51 virus structure from the X-ray crystallography data and they have reported that this protein is extra-flexible, which provides very high functionality and the ability to associate and/or dissociate of BLV capsid from the membrane of BLV infected cell [18]. Therefore, it is expected that on the surface of TiO_2 *gp*51 forms well-ordered monolayer. The formation of such layer was confirmed in other our researches by spectroscopic ellipsometry [10, 19, 20].

*Gp*51 protein is not a redox-protein therefore the charge transfer between *gp*51 and TiO_2 is not possible [18, 14]. However the *gp*51 protein like many others, contains a number of partially charged groups and domains, represented as partial charges "δ−" and "δ+" in Fig. 25.3b, which mostly are lower in value than the total electron charge (1.6×10^{-19} coulombs) per charged atom or group. The presence of these partial charges suggests that the electrostatic influence on the surface charge of TiO_2 from the side of partially uncompensated charges in those parts of the *gp*51 protein that located on the surface of TiO_2 is responsible for the adsorption of this protein on the TiO_2 surface. The Coulomb interaction takes place between charged groups in the *gp*51 protein and the negatively charged surface of the TiO_2 because such electrostatic interactions are very strong at a distances ranging from several Angstroms to few nanometers. Therefore, among the others interactions such as hydrogen bonds, disulfide bonds, Van der Waals interaction, etc., which also have

significant role during the adsorption of proteins, the electrostatic interaction plays one of the most important role during the adsorption of proteins to electrically charged surfaces, such as TiO_2. In addition, the local electric fields of charged domains of adsorbed proteins are affecting the photoluminescence centers of TiO_2 and it causes the shift in the photoluminescence spectra of TiO_2 nanoparticles. Therefore, the photoluminescence maximum caused by STE shifts from 517 to 499 nm (i.e., to 18 nm), which corresponds to ~0.086 eV that is less than 0.1 eV, and it is one of the proofs of electrostatic interaction based physical adsorption of *gp*51 [12].

The splitting of the photoluminescence spectra into Gaussian curves at each stage of the experiment shows that after the adsorption of *gp*51 protein molecules on the TiO_2 surface the energy value of excitation levels, which are responsible for the luminescence and are associated with oxygen vacancies $I_{V[O]}$, almost does not change remaining at a value of 605 ± 2 nm. At the same time, the photoluminescence maximum caused by recombination of self-trapped excitons (STE) [14, 21] shifts to short wavelengths, changing its position from 517 ($STE_1 = 2.39$ eV) nm to 499 ($STE_2 = 2.48$ eV) nm. Since the involvement of the STE level in the process of radiative recombination is regulated by the surface, this indicates that STE level is located either on the surface plane or not very deeply within the surface layer of TiO_2. The displacement of the light emitting recombination peak indicates that the energy level of STE is complex and has its 'basic' and 'excited' states [18]. The appearance of luminescence in the region of 499 nm indicates a radiative transition from the excited STE level. This indicates that the charge at the TiO_2/*gp*51 boundary controls the energy level of the STE and shows that the electronic demarcation level practically coincides with the position of the STE level, i.e. is approximately 2.39 eV above the valence band. Therefore, the appearance of proteins on the TiO_2 surface leads to a shift in the energy levels, including the light emitting centers, relatively to the electron demarcation level E_{dn}.

The blue-shift of the photoluminescence maximum by 18 nm as a result of adsorption of the *gp*51 protein, which corresponds to $\Delta E_{STE} = STE_2 - STE_1 = 0.086$ eV, also indicates that the initial value of the potential barrier on the TiO_2 surface has decreased by a value of 0.086 eV. Variation of the potential barrier means that the value of negative charge localized on the TiO_2 surface has also changed, due to the charge-charge-based interaction with adsorbed protein *gp*51. Positively charged atoms and groups, which are provided by the *gp*51 protein, partially compensates the surface charge of TiO_2 and reduces the energy of electrons localized at the surface levels, which are the most responsible for the generation of photoluminescence signal. Taking into account the fact that the total negative charge predominates on the TiO_2 surface, the positively charged parts of the *gp*51 protein electrostatically interact with the negatively charged TiO_2 surface. As a result, a partial decrease of the surface charge reduces the electric field in the TiO_2 surface region. Further interaction of TiO_2/*gp*51 structure with anti-*gp*51, which is also a protein, leads to the inverse changes in the photoluminescence spectra, i.e., to UV-shift the spectrum (Fig. 25.1) and decrease the photoluminescence intensity to the value that corresponds to the pure TiO_2. The latter effect is based on the formation an immune complex between immobilized antigens *gp*51 and anti-*gp*51 antibodies, which were present in aliquot.

Formation of this immune complex besides the van der Waals interaction and other interactions at a very high extent is based on the interaction between oppositely charged domains, functional groups and atoms in *gp*51 and anti-*gp*51 molecules (including the formation of number of hydrogen bounds, which can be estimated as specific kind of electrostatic interaction). It can be assumed that uncompensated charges (δ+ and δ−) of both proteins are involved in electrostatic interactions during the formation of immune complex. As a result, some of the charged groups that were originally involved in the interaction between *gp*51 and TiO_2 are at least partially compensated by the opposite charge of the anti-*gp*51 protein groups, thereby reducing the direct electrostatic effect from immobilized *gp*51 proteins to the charged surface of TiO_2 and to light emitting centers.

The effects described above cause the shift of photoluminescence maximum and decrease in the potential barrier on TiO_2/*gp*51 interface due to the charge-charge interaction between TiO_2 and *gp*51. The potential barrier at the interface between TiO_2 and *gp*51 has greater value in TiO_2/*gp*51 structure in comparison with that in TiO_2/*gp*51/anti-*gp*51 due to partial compensation (decrease in value) and/or delocalization of charges, which were initially involved into interaction between TiO_2 and *gp*51 after formation of TiO_2/*gp*51 structure.

The distribution of charges in TiO_2/*gp*51 structure can also be interpreted as a model based on an 'imaginary flat capacitor' (Fig. 25.4), formed as a result of the electrostatic interaction between oppositely charged protein *gp*51 layer and the TiO_2 surface. The capacitor is formed as a result of protein *gp*51 adsorption on TiO_2 surface, after which the charges are distributed in energetically most favorable way, partially compensating each other. Consequently, the positive 'imaginary capacitor plate' is based on the positive charges, which are predominant in the protein *gp*51 area that after adsorption appears in close proximity to TiO_2/*gp*51 interface and/or due to the negative electrostatic effect of TiO_2 are induced/attracted closer to negatively charged surface.

These charged atoms/groups/domains of *gp*51 that are localized in the close proximity to the TiO_2 surface and they electrostatically affect the TiO_2 emission centers and the energy value of the surface potential barrier. Hence, the position of the

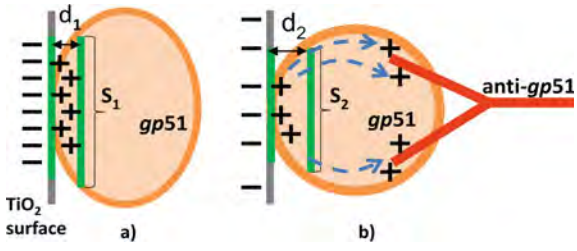

Fig. 25.4 Flat capacitor based model of the charges interaction between TiO_2 surface and *gp*51 proteins: **a** electrostatic interaction of uncompensated charges of immobilized protein *gp*51 with charges located on the surface of TiO_2; **b** model of interaction that takes into account the electrostatic interaction of charges within *gp*51 antigens and anti-*gp*51 antibodies

energy levels of the TiO_2 emission maximum depends on TiO_2 surface modification stage (TiO_2 or TiO_2/*gp*51) shifts from/backwards the initial position of the demarcation level. Figure 25.4a represents an imaginary flat capacitor consisting of a negatively charged plate on the surface of TiO_2 and an 'imaginary positively charged plate' formed in *gp*51 protein in close proximity to TiO_2/*gp*51 interphase. Hence, the interaction of TiO_2/*gp*51 with anti-*gp*51 antibodies and the formation of *gp*51/anti-*gp*51-based immune complex leads to a 'deformation' and the reduction of charge 'stored' on 'the positive imaginary capacitor plate' (Fig. 25.4b). This is mainly due to the redistribution and partial compensation of charges during the formation of the *gp*51/anti-*gp*51 immune complex, which in turn reduces the charge of 'the imaginary capacitor plate' based on *gp*51 ($q_2 < q_1$). Due to this reduced charge it can be interpreted as the reduction of the area of the same plate (S_2) and/or the increase of the distance (d_2) between the two imaginary capacitor plates based on *gp*51 and TiO_2 which leads to the decrease of capacitance according to (25.1).

$$C = \frac{\varepsilon \varepsilon_0 S}{d} \tag{25.1}$$

This effect is observed because some of the *gp*51 protein charges move from the TiO_2/*gp*51 interface towards interacting anti-*gp*51 protein and are partially compensated by charge present in anti-*gp*51, whereby the imaginary positive *gp*51-based capacitor plate of the capacitor is reduced in imaginary surface area and/or correspondingly moving apart from the negative TiO_2 plate. This effect leads to a decrease in the capacitance of this imaginary capacitor and the electric field induced by *gp*51 becomes reduced. Therefore, after the interaction of TiO_2/*gp*51 with anti-*gp*51 antibodies and the formation of *gp*51/anti-*gp*51 complex, which is involved into TiO_2/*gp*51/anti-*gp*51 structure, the electrostatic effect of *gp*51 initially adsorbed on TiO_2 towards the TiO_2 surface significantly decreases.

25.4 Conclusions

The main aspects of the interaction mechanism between nanostructured TiO_2 layer and bovine leukemia virus proteins *gp*51, during the formation of photoluminescence based immunosensor, have been developed. Bovine leukemia virus protein *gp*51, adsorbed on the surface of nanostructured TiO_2 thin film, formed the biosensitive layer (glass/TiO_2/*gp*51) that resulted in the TiO_2 photoluminescence peak shift from 517 to 499 nm. The interaction glass/TiO_2/*gp*51 structure with specific antibodies against *gp*51 (anti-*gp*51) has shifted the photoluminescence peak backwards from 499 nm to 516 nm. These photoluminescence shifts are attributed to the variation of STE energy level, which was induced by changes of electrostatic interaction between adsorbed *gp*51 and negatively charged TiO_2 surface. The displacement of the light emitting recombination peak confirms that the energy of STE level is complex and has its ground and excited states. The blue-shift of the photoluminescence

maximum by 18 nm as a result of adsorption of the *gp*51 protein, which corresponds to $\Delta E_{STE} = I_{STE2} - I_{STE1} = 0.086$ eV, indicates that the initial value of the potential barrier on the TiO_2 surface has decreased by a value of 0.086 eV. Variation of the potential barrier means that the value of negative charge localized on the TiO_2 surface has changed due to the charge-charge-based interaction with adsorbed protein *gp*51. Positively charged atoms and groups, provided by the *gp*51 protein, partially compensate the surface charge of TiO_2 and reduce the energy of electrons localized at the surface levels, which are the most responsible for the generation of photoluminescence signal.

The charge-charge-based interaction in the double charged layers TiO_2/*gp*51 can also be interpreted as a model of 'flat capacitor', formed as a result of the electrostatic interaction between oppositely charged protein *gp*51 layer and the TiO_2 surface. The capacitor is formed as a result of *gp*51 protein adsorption on TiO_2 surface, after which the charges are distributed in energetically most favorable way, partially compensating each other. Consequently, the positive 'imaginary capacitor plate' appears in the close proximity to TiO_2/*gp*51 interface, which is based on the positive charges of protein *gp*51, predominant after its adsorption on the TiO_2 surface. The positive charges are attracted closer to negatively charged surface due to the negative electrostatic effect of TiO_2. The interaction of TiO_2/*gp*51 with anti-*gp*51 antibodies and formation of *gp*51/anti-*gp*51-based immune complex leads to a deformation and reduction of charge in 'the positive imaginary capacitor plate', caused by redistribution and partial compensation of charges during the formation of the *gp*51/anti-*gp*51 immune complex, which in turn reduces the charge of 'the imaginary capacitor plate' based on *gp*51 adsorbed on the TiO_2 surface.

The highlighted origin of the changes in the photoluminescence spectra of TiO_2 as a result of the formation of biosensitive layer and after its interaction with the analyte, bring us closer to an understanding of the interaction mechanism between TiO_2 and proteins, that is the key in the solving of many issues related to an improvement of biosensor performance.

Acknowledgements This research was supported by Joint Ukrainian-Lithuanian research project "Application of hybrid nanostructures which are based on TiO_2 or ZnO and modified by biomolecules, in optoelectronic sensors", supported by Ministry of Education and Science of Ukraine (agreement No. M/20-2019) and Lithuanian Research Council (project No. P-LU-18-53).

References

1. A. Tereshchenko, M. Bechelany, R. Viter, V. Khranovskyy, V. Smyntyna, N. Starodub, R. Yakimova, Sensors Actuat B Chem **229**, 664 (2016)
2. A. Tereshchenko, V. Fedorenko, V. Smyntyna, I. Konup, A. Konup, M. Eriksson, R. Yakimova, A. Ramanavicius, S. Balme, M. Bechelany, Biosen Bioelectron **92**, 763 (2017)
3. R. Viter, A. Tereshchenko, V. Smyntynab, J. Ogorodniichuk, N. Starodub, R. Yakimova, V. Khranovskyy, A. Ramanavicius, Sensors Actuat B Chemical **252**, 95 (2017)
4. R. Plugaru, A Cremades and J Piqueras, J. Phys.: Condens. Matter 16 (2004)

5. J. Preclíková, P. Galář, F. Trojánek, S. Daniš, B. Rezek, I. Gregora, Y. Němcová, P. Malý, J. Appl. Phys. **108**, 113502 (2010)
6. X. Chen, S.S. Mao, Chem. Rev. **107**(7), 2891–2959 (2007)
7. A. Kumar Tripathi, M.K. Singh, M.C. Mathpal, S.K. Mishra, A. Agarwal, J Alloy Compd. **549**, 114 (2013)
8. X. Li, C. Gao, J. Wang, B. Lu, W. Chen, J. Song, S. Zhang, Z. Zhang, X. Pan, E. Xie, J. Power Sources **214**, 244–250 (2012)
9. A. Tereshchenko, V. Smyntyna, A. Ramanavicius, RSC Adv. **8**, 37740–37748 (2018)
10. R. Viter, V. Smyntyna, N. Starodub, A. Tereshchenko, A. Kusevitch, I. Doycho, S. Geveluk, N. Slishik, J. Buk, J. Duchoslav, J. Lubchuk, I. Konup, A. Ubelis, J. Spigulis, Procedia Eng. **47**, 338 (2012)
11. S. M. Gupta, M. Tripathi, Chin. Sci. Bull. **56**, 1639 (2011)
12. V. Smyntyna, *Electron and Molecular Phenomena on the Surface of Semiconductors* (Nova Publishers, New York, 2013)
13. D.L. Nelson, M.M. Cox, A.L. Lehninger, *Principles of Biochemistry* (Worth Publishtrs Inc., New York, 2000)
14. I. Sildos, A. Suisalu, V. Kiisk, M. Schuisky, H. Mändar, T. Uustare, J. Aarik, Proc. SPIE **4086**, 427
15. A. Tempczyk, C Kissinger, E. Villafranca, Catalytic *Mechanism of Calcineurin Serine* (Threonine Protein Phosphatase, Inc. 2010)
16. V. Shewale, P. Joshi, S. Mukhopadhyay, M. Deshpande, R. Pandey, S. Hussain, S. Karna, J. Phys. Chem. **115**, 10426 (2011)
17. G. Obal, F. Trajtenberg, F. Carrión, L. Tomé, N. Larrieux, X. Zhang, O. Pritsch, A. Buschiazzo, Science **5182**, 1–7 (2015)
18. T. Ogawa, *Biochemistry, Genetics and Molecular Biology, Volume 'Protein Engineering—Technology and Application'* (ISBN 978-953-51-1138-2)
19. Z. Balevicius, I. Baleviciute, S. Tumenas, L. Tamosaitis, A. Stirke, A. Makaraviciute, A. Ramanaviciene, A. Ramanavicius, Thin Solid Films **571**, 744 (2014)
20. I. Baleviciute, Z. Balevicius, A. Makaraviciute, A. Ramanaviciene, A. Ramanavicius, Biosen Bioelectron **39**, 170 (2013)
21. K. Wakabayashi, Y. Yamaguchi, T. Sekiya, S. Kurita, J. Lumin. **112**, 50 (2005)
22. Z. Balevicius, A. Makaraviciute, G.J. Babonas, S. Tumenas, V. Bukauskas, A. Ramanaviciene, A. Ramanavicius, Sensors Actuat B Chemical **181**, 119–124 (2013)

Chapter 26
Electrical and Photoelectric Properties of Iron/Chromium Oxide Nanolayers Composite Structures

I. Demchenko, S. Mulenko, A. Smirnov, R. Savkina, M. Walczak, and N. Voloshin

Abstract We report here results of our investigation of oxide nanometric films integrated with silicon substrates for new multifunctional applications. Ultraviolet photons of KrF-laser (248 nm) was used for the synthesis of nanometeric films based on iron and chromium oxides ($Fe_2O_{3-X}(0 \leq x \leq 1)$ and $Cr_{3-x}O_{3-y}(0 \leq x \leq 2; 0 \leq y \leq 2)$) with variable thickness, stoichiometry and electrical properties. X-ray photoelectron spectroscopy was used for nanometric films characterization. The roughness value of the samples investigated shows a good quality of the finishing characteristics of films synthesized by the reactive pulsed laser deposition technique. Investigation of the charge carriers' transport kinetics was carried out by surface photovoltage (SPV) and impedance spectroscopy technique. It was found that effect of the iron and chromium oxide layers' combination results in the photovoltage enhancement of 500 times in the spectral region between 600 and 1150 nm. The effect of the long-term relaxation of the photovoltage was revealed also.

I. Demchenko
Faculty of Chemistry, University of Warsaw, Warsaw, Poland

S. Mulenko
G. Kurdyumov Institute of Metal Physics NAS of Ukraine, Kiev, Ukraine

A. Smirnov · R. Savkina
V. Lashkaryov Institute of Semiconductor Physics NAS of Ukraine, Kiev, Ukraine

M. Walczak
School of Materials, University of Manchester, Manchester, UK

N. Voloshin (✉)
National Technical University of Ukraine "Igor Sikorsky Kyiv Polytechnic Institute", Kiev, Ukraine
e-mail: nick.voloshka@gmail.com

A. D. Pogrebnjak et al. (eds.), *Nanomaterials in Biomedical Application and Biosensors (NAP-2019)*, Springer Proceedings in Physics 244,
https://doi.org/10.1007/978-981-15-3996-1_26

26.1 Introduction

Transition-metal oxides are considered to be very fascinating functional materials [1]. Their unique features involve high dielectric constants, efficient charge separation, enhanced surface reactivity as well as magnetization and polarization properties. Applications of composite structures including two or more transition-metal oxides allow even wider diversity in their electronic properties and chemical behavior. For example, in single-phase multiferroic metal-oxide based materials, the magnetoelectric coupling is very weak and the ordering temperature is too low [2]. In contrast, multiferroic composites incorporated ferroelectric and ferromagnetic phases are characterized with giant magnetoelectric coupling response above room temperature. Besides, it is well-known that a variety of changes in both chemical and physical properties of materials under consideration occur in the nanoscale area. Therefore, transition metal-oxides based nanocomposite structures research is still relevant and important in terms of the practical application of the ones.

Isostructural and isovalent iron and chromium oxides are the subject of active experimental and theoretical investigations as members of the transition metal oxide family [3–8]. The polycrystalline α-Fe_2O_3 and Cr_2O_3 under normal conditions crystallize in the lattice with R3c space group symmetry. Thermodynamically, hematite (α-Fe_2O_3) is the most stable in the family of iron (III) oxides. It is a charge transfer insulator with a band gap of ~2.1 eV [6], absorbs ~40% of the solar spectrum [5], and conducts when doped with Ti [4]. The Cr_2O_3 compound has an eskolaite-like structure. It is one of the most important wide band gap (Eg ≈ 3.3 eV) p-type semiconductor transition metal-oxide material with efficient dielectric properties. Up to now, Cr_2O_3 has been most promising material for realistic applications close to room temperature in magnetoelectric-controlled spintronic elements like MERAM.

Multilayer structures based on these materials exhibit multiferroic behaviors. We have previously demonstrated magnetic hysteresis and magnetoresistive memory effect for hybrid systems of the alternate layers Fe_2O_{3-x}($0 \leq x \leq 1$)/$Cr_{3-X}O_{3-Y}$($0 \leq x \leq 2$; $0 \leq y \leq 2$) [9]. Besides, interest in understanding such materials is being renewed because of their distinctive properties including enhanced surface reactivity and efficient charge separation.

Important properties of iron oxide are its low-toxicity, Earth abundant and suitable redox potential for photocatalytic water dissociation as a source of H_2 fuel [7]. But, one of the major limiting factors affecting the utilization of hematite as a photocatalysts include fast electron–hole recombination. This can be improved by the development of the built-in electric fields and charge carriers' separation by exploitation the band offset properties of Fe_2O_3/Cr_2O_3 heterojunctions. Theoretical justification and experimental studies can be found in the following [3, 8] respectively. The Fe_2O_3/Cr_2O_3 heterostructure is known to have a type-II band alignment, where valence band maximum in Fe_2O_3 is lower than that of Cr_2O_3 [8]. This feature results in an occurrence of the potential gradient over several periods of the multilayer structure that may be useful for enhanced effectiveness in spatially separating electrons and holes.

In the present work we report on the studies of the electrical and photoelectric properties of nanometric films of iron and chromium oxides ($Fe_2O_{3-x}(0 \leq x \leq 1)$, $Cr_{3-X}O_{3-Y}(0 \leq x \leq 2;\ 0 \leq y \leq 2)$) as well as nanocomposite structures of the alternate layers $Fe_2O_{3-x}(0 \leq x \leq 1)/Cr_{3-X}O_{3-Y}(0 \leq x \leq 2;\ 0 \leq y \leq 2)$ synthesized on silicon substrates by reactive pulsed laser deposition (RPLD) method. Here, we use surface photovoltage and impedance spectroscopy technique for investigation of charge carriers' transport in this material.

26.2 Experiment Details

26.2.1 Materials

We have carried out a study of nanometric films based on oxides of the transitional metals with variable thickness, stoichiometry and electrical properties. Chromium $Cr_{3-X}O_{3-Y}$ $(0 \leq x \leq 2;\ 0 \leq y \leq 2)$ and iron $(Fe_2O_{3-X}(0 \leq x \leq 1)$ oxide layers as well as their combination ($Fe_2O_{3-Y}/Cr_{3-X}O_{3-Y}/Fe_2O_{3-Y}/Cr_{3-X}O_{3-Y}$) were grown by RPLD techniques in the vacuum stainless steel reactor on the boron-doped (100)-oriented p-type silicon wafers at the substrate's temperature $T_S = 293$ and 800 K. The development and improvement of RPLD technology for the production of nanometric films of iron and chromium oxides is shown in [10, 11]. The thickness of the films (d) was controlled by "Tensor Instruments" model "Alpha-step 100" profilometer with an accuracy of 5%.

26.2.2 Methods

The samples were studied by X-ray photoelectron spectroscopy (XPS) using Kratos Ultra Axis spectrometer with monochromatic Al Kα radiation ($h\upsilon = 1.4866$ keV) from an X-ray source with a spot of $700 \times 300\ \mu m^2$ (due to the analyzer settings in hybrid mode) while operating at 150 W and 15 kV. The high-resolution (HR) XPS spectra were collected with the hemispherical analyzer at the pass energy of 20 eV and the energy step size of 0.1 eV. The photoelectron take-off angle was 0° with respect to the normal to the sample's surface plane. No charge compensation was applied. Samples were mounted on the grounded holder. Binding energies (BEs) of the photoelectrons were calibrated using the gold $4f_{7/2}$ photoelectron peak at 84 eV. The Casa XPS software (version 2.3.17) [12] was used to evaluate the XPS data. Taking into account that sputtering procedure can easily modify electronic structure of studied samples due to intermixing of atoms (see, e.g., [13]), it was decided to abandon sputtering in this study.

All samples were characterized by measuring their surface photovoltage (SPV) spectra. These measurements were performed at 300 K on a spectrometer SPM-2

with a G-60 prism using a lock-in detection scheme with modulation at 200 Hz at low level of homogeneous excitation by a monochromatic light in a wavelength range of 500 ÷ 1200 nm. The light source was a quartz halogen lamp JCD (950 lm; 50 W). A photovoltage arising was recorded without electrical bias by lock-in nanovoltmeter. Contact metallization was photolithographically patterned on the structure top. Impedance characteristics of the samples were studied using the precision impedance meter Z-3000X within the frequency range 1 Hz…3 × 10^6 Hz with the amplitude of a sinusoidal signal 120 mV.

26.3 Results and Discussion

Our previous X-ray diffraction (XRD) investigation evidenced the polycrystalline structure of the metal oxide films deposited on Si substrate in oxygen atmosphere [14]. Moreover, XRD analysis revealed strong correlation between oxide structural properties and technological parameters. The increase of oxygen pressure in the chamber caused a kinetic energy loss of iron atoms. Correspondingly, the cooling time of films on substrate decreases and the crystallization status is worsening. This accompanied by the decrease of the line intensity in XRD iron oxides spectra. On the other hand, in case of substrates heated at 800 K, the iron oxide lines in XRD spectra are enhanced, the kinetic energy of the ions is increased, resulting in the growth of a new iron oxide phase. Chromium oxide films composition depends strongly on oxygen content in the gas phase and mainly composed of Cr_2O_3 which is the most stable phase in the Cr–O phase diagram [11].

26.3.1 Surface Electronic Structure Characterization

XPS was used to measure of Fe 3p/3s, Cr 3p/3s, and O 2s core levels. Figure 26.1a shows electron spectra partially covering the valence band region up to Fe 3s line at 93.6 ± 0.2 eV for standard and investigated samples. Spin exchange splitting of the Fe 3s and Cr 3s states is clearly seen in the experimental data. The exchange interaction between cores electrons and those in incomplete shells, here 3d electrons, gives rise to multiplet splitting of the s-electrons themselves [15]. The estimated Cr 3s multiplet splitting for examined samples is the same and equals to 4 eV (BE of the main resonance is 75.4 ± 0.2 and of the second one is 79.4 ± 0.2 eV). Obtained values agree well with data shown by Battistoni et al. [16] representing Cr_2O_3 phase. The Cr 3p BE is 43.6 ± 0.2 eV for both examined samples, and according to [17], it is associated with Cr_2O_3 phase as well. It is clearly seen (see "Mult.lay.#2" data in Fig. 26.1a) that the loss feature of Cr 3p (marked by blue asterisk) superimposes with the Fe 3p states. Nevertheless, the Fe 3p/3s lines development (i.e., intensity of signal dependence for multilayer samples) makes it clearthat the thickness of the top layer of chromium oxide is greater for the sample "Mult.lay.#1". Opposite is true for the

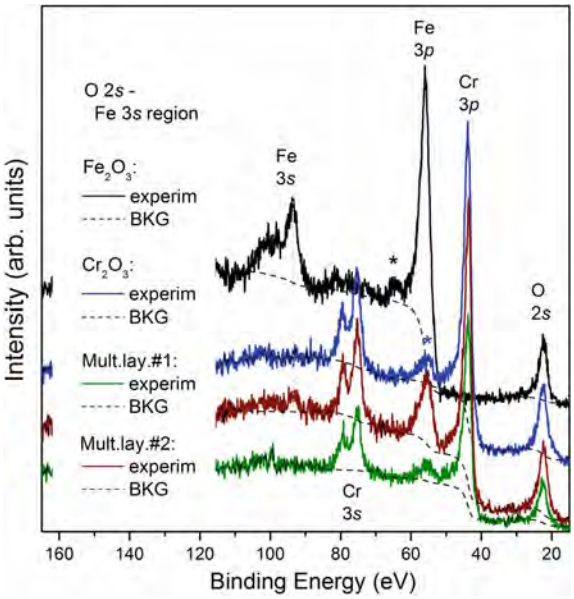

Fig. 26.1 XPS spectra of the Fe3*s*, Cr3*s*, Fe3*p*, Cr3*p*, and O2*s* states measured for Fe_2O_3 (PO_2 = 0.5 Pa, d = 26 HM, N = 5000), Cr_2O_3 (PO_2 = 0.5 Pa, d = 55 HM, N = 5000), and both "Cr_2O_3/Fe_2O_3" multilayer structures: "Mult.lay.#1" (PO_2 = 0.5 Pa, d = 100 HM, N = 2500/2000/2500/2000), "Mult.lay.#2" (PO_2 = 0.5 Pa, d = 10 HM, N = 500/500/500/500). Here and further N is number of the laser impulses. Dashed lines show background signal that was removed before the analysis

sample "Mult.lay.#2", where contribution of Fe 3p/3s lines is difficult to distinguish. Deconvolution of both lines give the flowing BE values: 93.8 ± 0.2 eV for Fe 3s (whereas multiplet splitting is estimated to be 7.3 eV) and 55.6 ± 0.2 eV for Fe 3p. To the same precision, both of them correspond to Fe_2O_3 [17, 18]. Unfortunately, it was found that BEs of the 3d/s lines for Fe_2O_3 are the same or close to Fe_3O_4 phase (there are no differences in BE of the Fe 3s line and only 0.2 eV for the Fe 3p line [19]). Consequently, as a next step, we would like to check the Fe 2p line for the mentioned above compounds noting that the difference of the Fe 2p3/2 resonances in standard (Fe_2O_3 vs. Fe_3O_4) samples is 0.8 eV. The results of this study will be published elsewhere. In any case, the results obtained by XPS at present stage confirm the conclusion of the XRD studies [11, 14] on these samples, namely, existence of Cr_2O_3 and Fe_2O_3 phases.

26.3.2 Kinetics and Spectral Distribution of the Surface Photovoltage

All samples were characterized by measuring their surface photovoltage (SPV) spectra. Surface photovoltage is defined as the difference between the surface potential of a sample in the dark and under illumination. A nonzero SPV indicates redistribution of photogenerated free charges. As a modulated illumination was used in our experiment, the surface photovoltage value can be expressed as [20]:

$$V_{PV}(\omega) = J_{PC}(\omega) \cdot Z_{eff}(\omega),$$

where the photocurrent density—J_{PC} is typically extracted from a current-balance calculation and the effective impedance—Z_{eff} is composed of parallel resistance (R_j) and capacitance (C_j) components, corresponding to the contributions of the various photovoltage influencing agents such as minority and majority carrier transport, depletion and inversion layers, surface states, etc.

Figure 26.2 shows the SPV spectra of Si-based multi-component composite systems investigated. SPV spectrum of Si substrate in the original state (not shown) exhibits a selective peak with the spectral position of the 'red' boundary, which corresponds with the silicon band gap Eg = 1.158 eV (300 K). The SPV spectra of $Cr_{3-X}O_{3-Y}$ ($0 \leq x \leq 2$; $0 \leq y \leq 2$) nanometric film on Si substrate exhibits a selective peak with maximum corresponding to the silicon band gap Eg at 300 K. It is obvious that chromium oxide layer is transparent in this spectral region. The measured value of the SPV_{max} of "iron oxide on silicon" structure at light power density ~1 W cm^{-2} is about ~4 μV (see Fig. 26.2b). At the same time, it was found a surprising improvement in the photoelectric properties of multilayer systems. A broad band of the photosensitivity between 600 and 1150 nm with a high value of the photovoltage ~2×10^3 μV is typical for $Cr_{3-x}O_{3-y}/Fe_2O_{3-y}/Cr_{3-x}O_{3-y}/Fe_2O_{3-y}$ on Si structures (Fig. 26.3c).

It should be noted, that an increase in the photosensitivity in the visible range showed samples grown on a cold substrate. At the same time, samples grown on a hot substrate (800 K) have exhibited photoluminescence phenomenon in the range 500–600 nm.

The photovoltage kinetics was studied by the example of this structure. The typical time dependence of the photovoltage signal for $Cr_{3-x}O_{3-y}/Fe_2O_{3-y}/Cr_{3-x}O_{3-y}/Fe_2O_{3-y}$ on Si structure excited by radiation with quantum energy 2.53 eV is demonstrated in Fig. 26.2d. The effect of the long-time photorelaxation was found. Photovoltage increases and reaches a maximum within 12 min. The total time of the photorelaxation is about 120 min. The photovoltage signal V_{PV} kinetics can be described by the dependence:

$$V_{PV}(t) = A_{1,2}\left(1 - b_{1,3}\exp\left(-t/\tau_{1,3}\right) - b_{2,4}\exp\left(-t/\tau_{2,4}\right)\right)$$

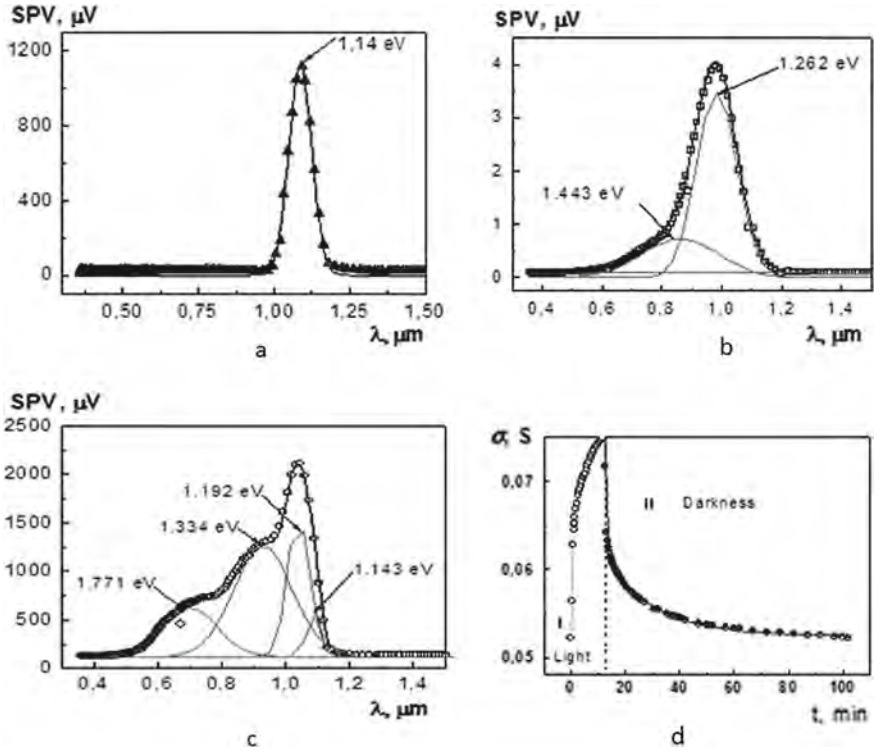

Fig. 26.2 Surface photovoltage spectra of nanometric layers structure deposited on Si substrate corrected on spectral response of setup: **a** $Cr_{3-x}O_{3-y}$/Si, **b** Fe_2O_{3-x}/Si, **c** Mult.lay.#2 $(Cr_{3-x}O_{3-y}/Fe_2O_{3-y}) \times 2$ on Si. All SPV spectra have complicated shape that could be described by a sum of number components. In order to determine positions of spectral components, we have used a deconvolution procedure with fitting to Gauss functions. The peak positions are presented in figures. The dots indicate the experimental data and the solid lines present the results of the fitting procedure. The thin-dash lines show approximation. **d** kinetics of photovoltage of multilayer systems excited by blue LED ($\lambda_D = 475$ nm, the electrical power 1 W) in uninterrupted regime: I—region of the photoexcitation; II—region of the relaxation

where $\tau_1 = 0.51$ min, $\tau_2 = 9.03$ min are the characteristic times of the photoexitation (region I in Fig. 26.2d) and $\tau_3 = 0.92$ min, $\tau_4 = 19.05$ min are the characteristic times of the relaxation (region II in Fig. 26.2d). It should be noted that long-term relaxation is typical for wide-gap oxides such as ZnO or SnO_2 [21] and is associated with stoichiometric oxygen deficiency in these compounds. Another view at the long-term relaxation of the photoexitation in multiferroic materials ($BiFeO_3$) is presented in [22], where a photo-induced depolarization with excited localized states was proposed and first-principles calculations of double-potential well were provided. Anyway, to determine the mechanism of long-term relaxation in our case, additional studies are needed.

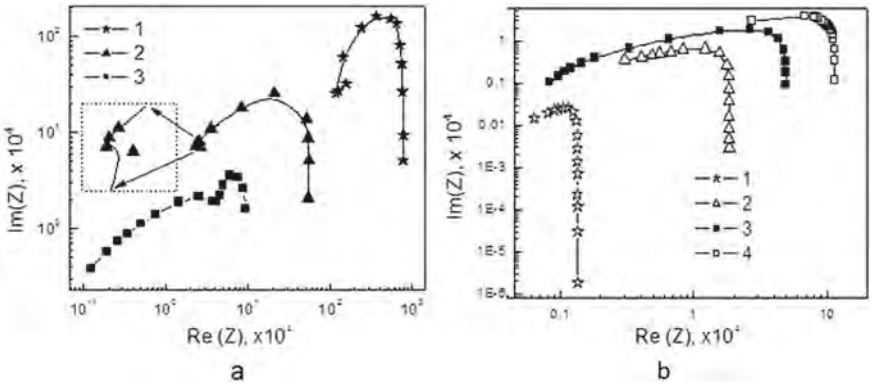

Fig. 26.3 Nyquist plots for **a** $Cr_{3-X}O_{3-Y}$ ($0 \leq x \leq 2$; $0 \leq y \leq 2$)) nanometric films on Si substrate: 1—$PO_2 = 1$ Pa, d = 160 нм, N = 5000; 2—$PO_2 = 0.05$ Pa, d = 40 нм, N = 4000; 3—$PO_2 = 0.5$ Pa, d = 55 нм, N = 5000 and **b** multilayer structures $(Cr_{3-x}O_{3-y}/Fe_2O_{3-y})$/Si and $(Cr_{3-x}O_{3-y}/Fe_2O_{3-y}) \times 2$/Si: 1—$PO_2 = 0.5$ Pa, d = 26 нм, N = 5000; 2—$PO_2 = 0.5$ Pa, d = 100 нм, N = 2500/2000/2500/2000; 3—$PO_2 = 0.5$ Pa, N = 3000/3000, d = 80 нм, $T_{sub} = 293$ K; 4—$PO_2 = 0.5$ Pa, N = 3000/3000, d = 80 нм, $T_{sub} = 800$ K. The impedance measurements were performed at the G-Cp (parallel conductance and capacitance) configuration using Au plates as blocking electrodes. The dots in the figure are experimental data and the solid line is fitting curves obtained by EIS spectrum analyzer

26.3.3 Impedance Spectroscopy

It is known that a semiconductor structure with a potential barrier, in the simplest case, can be considered within the context of an equivalent circuit consisting of the resistance of the depletion region and the barrier capacitance connected in parallel and the resistance connected in series to them. Electrical Impedance Spectroscopy (EIS) is a very sensitive method for research of non-stationary charge transport governed by charge-carrier relaxation in semiconductors structure and development an equivalent circuit. EIS technique has been used for characterization the electron transport kinetics of $Cr_{3-X}O_{3-Y}$($0 \leq x \leq 2$; $0 \leq y \leq 2$), Fe_2O_{3-X}($0 \leq x \leq 1$), $(Cr_{3-x}O_{3-y}/Fe_2O_{3-y})$ and $2 \times (Cr_{3-x}O_{3-}y/Fe_2O_{3-y})$ structures on Si substrate prepared by RPLD.

Figure 26.3 Nyquist plots for (a) $Cr_{3-X}O_{3-Y}$ ($0 \leq x \leq 2$; $0 \leq y \leq 2$) nanometric films and (b) multilayer $Cr_{3-x}O_{3-y}/Fe_2O_{3-y}$ structures on Si substrate. The impedance plane plots for multilayer $Cr_{3-x}O_{3-y}/Fe_2O_{3-y}$ structures on Si substrate (Fig. 26.3b, curve 2, 3, 4) as well as single-layer samples of Fe_2O_{3-y} (Fig. 26.3b, curve 1) and $Cr_{3-x}O_{3-y}$ (Fig. 26.3a, curve 3) are in the shape of one or two semicircles, which can be well interpreted by an equivalent circuit composed of resistors R and constant phase element CPE in parallel. One semicircle corresponds to one chain R-CPE, two semicircles—sequences of two chains R-CPE in series. CPE element accounts for a disorder in the charge diffusion dynamics by material inhomogeneity, which can be typically expected in a polycrystalline material.

At the same time, Nyquist plots for $Cr_{3-X}O_{3-Y}$ ($0 \leq x \leq 2$; $0 \leq y \leq 2$) nanometric films obtained under $PO_2 = 1$ Pa (Fig. 26.3a, curve 1) and $PO_2 = 0.05$ Pa (Fig. 26.3a, curve 2) are characterized by the presence of a loop at the higher frequency side graphics that corresponds to the inductive-type impedance of these material (see Inset in Fig. 26.3a).

26.4 Conclusions

In summary, we have investigated the light-induced phenomena in nanometric films based on iron and chromium oxides (Fe_2O_{3-X}($0 \leq x \leq 1$) and $Cr_{3-X}O_{3-Y}$($0 \leq x \leq 2$; $0 \leq y \leq 2$)) as well as composite structures of the alternate layers Fe_2O_{3-X}($0 \leq x \leq 1$)/$Cr_{3-X}O_{3-Y}$($0 \leq x \leq 2$; $0 \leq y \leq 2$) synthesized on silicon substrates by reactive pulsed laser deposition. It was found that "chromium oxide on silicon" structure is transparent and "iron oxide on silicon" structure exhibits weak photosensitivity in the wavelength range of 500 ÷ 1200 nm. At the same time, it was found a surprising improvement in the photoelectric properties of multilayer systems. Effect of the nanometric oxide (Cr, Fe) layers combination results in the photovoltage enhancement of 500 times. Moreover, the effect of long-term relaxation with a total time of the photorelaxation up to 2 h characterizes such multilayer structure. The equivalent electrical circuit model was obtained by EIS technique for structures investigated.

We think that integration silicon as an industrial key material and oxide-based composite nanostructures characterized by a close coupling of magnetization and polarization properties (such as transitional metal oxides Fe_2O_3, Cr_2O_3) will help in the generation of the new class of sensing devices which multifunctionality can be controlled not only by applied magnetics or electric fields but also by light.

Acknowledgements This work is done within Ukrainian–Polish joint research project "Characterization of the hybrid system of the nanometric layers based on transition metals oxides useful for spintronic" under the agreement on scientific cooperation between the Polish Academy of Sciences and the National Academy of Sciences of Ukraine.

References

1. S. Maekawa, T. Tohyama, S.E. Barnes, S. Ishihara, W. Koshibae, G. Khaliullin, *Physics of transition metal oxides*, vol. 144 (Springer, Verlag Berlin Heidelberg, 2004)
2. N.A. Hill, J. Phys. Chem. B **104**, 6694–6709 (2000)
3. T.C. Kaspar, D.K. Schreiber, S.R. Spurgeon, M.E. Mc Briarty, G.M. Carroll, D.R. Gamelin, et al., Adv. Mater. **28**(8), 1616–1622 (2016)
4. B. Zhao, T.C. Kaspar, T.C. Droubay, J. McCloy, M.E. Bowden, V. Shutthanandan et al., Phys. Rev. B **84**, 245325 (2011)
5. M.N. Huda, A. Walsh, Y. Yan, S.-H. Wei, M.M. Al-Jassim, J. Appl. Phys. **107**(12), 123712 (2010)

6. H. Mashiko, T. Oshima, A. Ohtomo, Appl. Phys. Lett. **99**(24), 241904 (2011)
7. T.W. Hamann, Dalton Trans. **41**(26), 7830–7834 (2012)
8. S.A. Chambers, Y. Liang, Y. Gao, Phys. Rev. B **61**(19), 13223 (2000)
9. A.B. Smirnov, S.B. Kryvyi, S.A. Mulenko, M.L. Sadovnikova et al., Nanoscale Res. Lett. **11**(1), 467 (2016)
10. S.A. Mulenko, YuN Petrov, N.T. Gorbachuk, Appl. Surf. Sci. **258**(23), 9186–9191 (2012)
11. A.P. Caricato, A. Luches, M. Martino, D. Valerini, Y.V. Kudryavtsev et al., J. Optoelecron. Adv. Mater. **12**(3), 427–431 (2010)
12. N. Fairley, *Software Package for the Analysis of XPS Results, Casa XPS Version 2.3.17 dev6.6o* (Casa Software Ltd.). http://www.casaxps.com
13. I.N. Demchenko, W. Lisowski, Y. Syryanyy, Y. Melikhov, I. Zaytseva et al., Appl. Surf. Sci. **399**, 32–40 (2017)
14. N. Serban, C. Ristoscu, G. Socol, N. Stefan et al., Mater. Res. Bull. **50**, 148–154 (2014)
15. G.K. Wertheim, S. Hufner, H.J. Guggenheim, Compounds. Phys. Rev. B **7**(1), 556 (1973)
16. C. Battistoni, J.L. Dormann, D. Fiorani, E. Paparazzo, S. Viticoli, Solid State Commun. **39**(4), 581–585 (1981)
17. G.C. Allen, S.J. Harris, J.A. Jutson, J.M. Dyke, Appl. Surf. Sci. **37**(1), 111–134 (1989)
18. https://srdata.nist.gov/xps/acknowledgment.aspx
19. P. Mills, J.L. Sullivan, J. Phys. D Appl. Phys. **16**(5), 723 (1983)
20. L.W. Martin, Y.H. Chu, R. Ramesh, Mater. Sci. Eng. Rep. **68**(4–6), 89–133 (2010)
21. Tianyou Zhai, Xiaosheng Fang, Meiyong Liao et al., Sensors **9**, 6504–6529 (2009)
22. Gu Jun-xing, Kui-juan Jin, Le Wang et al., J. App. Phys. **118**(20), 204103 (2015)

Subject Index

A. D. Pogrebnjak et al. (eds.), *Nanomaterials in Biomedical Application and Biosensors (NAP-2019)*, Springer Proceedings in Physics 244,
https://doi.org/10.1007/978-981-15-3996-1